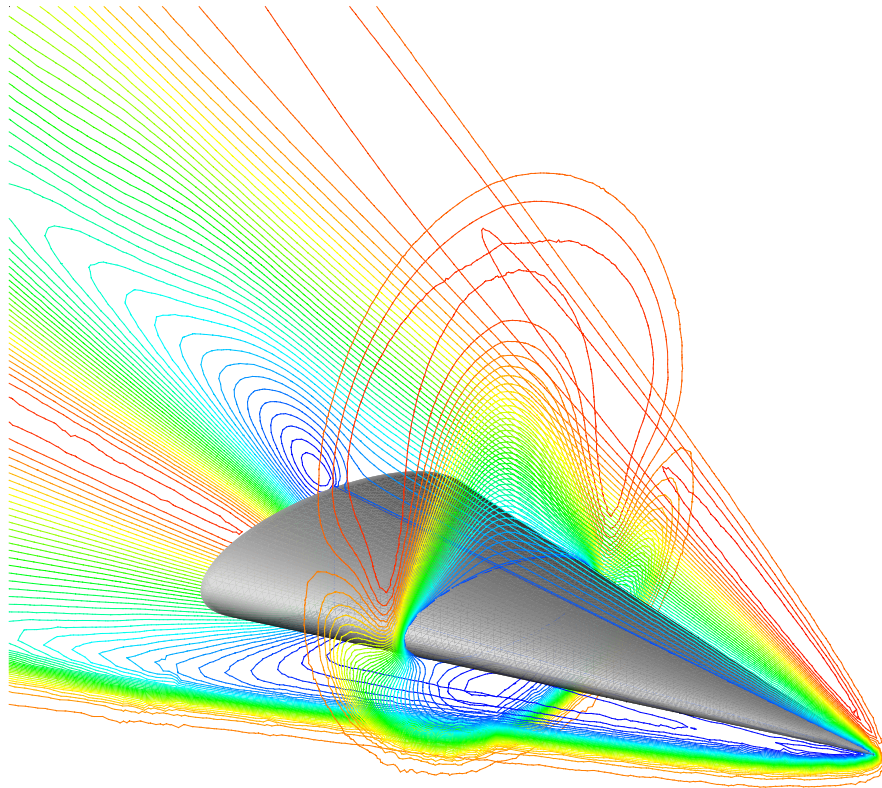


**On steady laminar basic flows and
their global eigenmodes:
An elliptic cone in compressible flow**



VASSILIOS THEOFILIS

(October 2000)

Report Documentation Page		
Report Date 31OCT2000	Report Type N/A	Dates Covered (from... to) -
Title and Subtitle On steady laminar basic flows and global eigenmodes: An elliptic cone in compressible flow	Contract Number	
	Grant Number	
	Program Element Number	
Author(s) Theofilis, Vassilios	Project Number	
	Task Number	
	Work Unit Number	
Performing Organization Name(s) and Address(es) Dr. Vassilios Theofilis Rohnsterrassen 14 Gottingen D-37085 Germany	Performing Organization Report Number	
Sponsoring/Monitoring Agency Name(s) and Address(es) EOARD PSC 802 Box 14 FPO 09499-0200	Sponsor/Monitor's Acronym(s)	
	Sponsor/Monitor's Report Number(s)	
Distribution/Availability Statement Approved for public release, distribution unlimited		
Supplementary Notes The original document contains color images.		
Abstract		
Subject Terms		
Report Classification unclassified	Classification of this page unclassified	
Classification of Abstract unclassified	Limitation of Abstract UU	
Number of Pages 95		

REPORT DOCUMENTATION PAGE			Form Approved OMB No. 0704-0188	
Public reporting burden for this collection of information is estimated to average 1 hour per response, including the time for reviewing instructions, searching existing data sources, gathering and maintaining the data needed, and completing and reviewing the collection of information. Send comments regarding this burden estimate or any other aspect of this collection of information, including suggestions for reducing this burden to Washington Headquarters Services, Directorate for Information Operations and Reports, 1215 Jefferson Davis Highway, Suite 1204, Arlington, VA 22202-4302, and to the Office of Management and Budget, Paperwork Reduction Project (0704-0188), Washington, DC 20503.				
1. AGENCY USE ONLY (Leave blank)		2. REPORT DATE 31 October 2000		3. REPORT TYPE AND DATES COVERED Final 31 October 2000
4. TITLE AND SUBTITLE On steady laminar basic flows and global eigenmodes: An elliptic cone in compressible flow.			5. FUNDING NUMBERS F61775-99-WE049	
6. AUTHOR(S) Dr. Vassilios Theofilis				
7. PERFORMING ORGANIZATION NAME(S) AND ADDRESS(ES) Dr. Vassilios Theofilis Rohnsterrassen 14 Gottingen D-37085 Germany			8. PERFORMING ORGANIZATION REPORT NUMBER	
9. SPONSORING/MONITORING AGENCY NAME(S) AND ADDRESS(ES) EOARD PSC 802 Box 14 FPO 09499-0200			10. SPONSORING/MONITORING AGENCY REPORT NUMBER SPC 99-4049	
11. SUPPLEMENTARY NOTES Color plates				
12a. DISTRIBUTION/AVAILABILITY STATEMENT Public release. Government Rights License. All other rights reserved by the copyright owner.			12b. DISTRIBUTION CODE A	
12. ABSTRACT (Maximum 200 words) The present report is the first step towards global linear instability analysis of three-dimensional flowfields over elliptic cones at hypersonic speeds. The report discusses basic flows which form the variable coefficients of the partial differential equation eigenvalue problem at a small representative class of the parameter values at which the analyses will ultimately be performed. The report illustrates characteristic compressible flowfields recovered at constant Reynolds number and increasing angle of attack and Mach number, keeping for the most part of this work the same resolution of three-dimensional space. The contract tasking states: "The contractor will perform a three-dimensional inviscid analysis of the nonparallel steady compressible basic flow over an elliptic cone. A Compressible direct numerical simulation (DNS) code will be developed. The work will show a comparison between the basic flow results obtained with experimental and independently obtained results. The deliverables are the steady-state flow results and the code used to obtain them.				
14. SUBJECT TERMS EOARD, Separated flows, Compressible flow, Laminar flow			15. NUMBER OF PAGES	
			16. PRICE CODE	
17. SECURITY CLASSIFICATION OF REPORT Unclassified	18. SECURITY CLASSIFICATION OF THIS PAGE Unclassified	19. SECURITY CLASSIFICATION OF ABSTRACT Unclassified	20. LIMITATION OF ABSTRACT Unlimited	

On steady laminar basic flows and their global eigenmodes:

An elliptic cone in compressible flow

B Y VASSILIOS THEOFILIS †

Rohnsterrassen 14, D-37085 Göttingen, GERMANY

tel./fax: +49 551 48 76 25

(31 October 2000)

In the framework of our efforts towards a global nonparallel linear instability analysis of compressible flow over an elliptic cone we discuss here two interconnected aspects, the steady basic flowfield and the associated global eigenmodes. First, we validate and apply the AUSMDV shock-capturing scheme to recover *three-dimensional* steady basic states around an aspect ratio 3 elliptic cone in the range of Mach numbers $0.5 \leq M \leq 4$ at angles of attack $\alpha = 10^\circ$ and 20° and a low Reynolds number value $Re = 10^3$, at which laminar flow is ensured. In doing so we implicitly rely on the global instability analysis which will follow the present effort to identify potential departures from the calculated steady basic states through amplified global eigenmodes. Second, potential extensions of the present work are outlined. One of them is an inviscid global instability analysis on the basis of the generalised Rayleigh equation, presented herein for the first time, which governs small-amplitude three-dimensional global perturbations of essentially two-dimensional compressible basic states. Third, we elaborate on the issue of residuals in time-accurate simulations for the recovery of steady state solutions of the equations of motion. We identify the former as the least stable global eigenmodes of the flow. Based on the present findings, we present an algorithm which permits recovery of the steady state from transient data at a negligible fraction of the otherwise necessary computing effort. Application of the algorithm to extract the three-dimensional flowfield on the elliptic cone is underway.

† This material is based upon work supported by the European Office of Aerospace Research and Development, Air Force Office of Scientific Research, Air Force Research Laboratory, under Contract No. F61775-99-WE049. Research is monitored by Dr. R. Kimmel.

Contents

	PAGE
1. Introduction	3
2. The Basic Flow Computation	6
(a) Governing equations	6
(b) Flux-splitting and the AUSMDV scheme	7
(c) Numerical discretisation	7
3. Basic Flow Results	9
(a) Validation of the AUSMDV scheme	9
(b) Compressible three-dimensional laminar flows over an aspect ratio 3 elliptic cone	10
4. Global Linear Instability Theory	14
(a) Small-amplitude disturbances superimposed upon a steady laminar flow	14
(b) Comments on the quality of the steady laminar basic flows	16
5. The Generalised Rayleigh Equation	17
(a) Two-dimensional inviscid global linear analysis	17
(b) Further simplifications	18
6. On numerical residuals and physical instabilities in steady-state fluid flow calculations	20
(a) The problemacy with residuals	20
(b) Theory	21
(c) Results for the square lid-driven cavity	28
(d) Summary and Epilogue	35
7. Discussion	37
Appendix A. The two-dimensional inviscid linear operators \mathcal{A}_{2d} and \mathcal{B}_{2d}	39
References	41

1. Introduction

Revived interest in affordable hypersonic flow technology (Walker 1999) has resulted in renewed efforts to understand and control the related physical mechanisms of laminar-turbulent flow transition (Kimmel and Walker 1999). One of the configurations in discussion is that of the elliptic cone which is known to have distinct aerodynamic advantages over bodies of revolution in compressible flow at least as early as the pioneering work of Jorgensen (1958). Renewed theoretical and experimental efforts on elliptic cones have been undertaken by Kimmel *et al.* (1997,1999) and Huntley *et al.* (1999) with special emphasis placed on laminar-turbulent flow transition, thus expanding upon knowledge on compressible boundary-layer flow transition on a circular-base cone (Stetson and Kimmel 1992). Kimmel *et al.* (1999) have discovered characteristics of flow transition on the elliptic cone which appear to be intrinsically three-dimensional and distinct from known instability mechanisms on bodies of revolution. Despite substantial progress on the issue, three-dimensional boundary layer transition in high-speed flow presently appears to be far from understood in a satisfactory manner.

The issue of laminar-turbulent transition has a long and successful track record, following the pioneering works of the first half of last century on linear instability in boundary layers on flat-plates and bodies of revolution (Lin 1955). The main limitation of most of the existing analyses is their confinement within the framework of flowfields in which two of the three spatial directions are taken to be homogeneous and are resolved by a periodicity Ansatz. Under these so-called *local* assumptions the classic Rayleigh and Orr-Sommerfeld equations result, respectively, in inviscid and viscous incompressible flow (Drazin and Reid 1981). The compressible counterparts of either equation have been extensively investigated and discussed by Mack (1969, 1984). With the maturing of numerical algorithms and the current progress in hardware technology the assumption of homogeneity in two spatial directions can be relaxed within the framework of a direct numerical simulation (DNS) in which all three spatial directions may, in principle, be taken as inhomogeneous and be resolved; marching the equations of motion forward in time delivers the desired instability information. While DNS is an undisputed approach in terms of its capacity to deliver solutions of the equations of motion, there are two points that deserve discussion with respect to using DNS for instability analyses.

The first point is related with computing effort and the associated cost of a DNS. The latter, though decreasing in recent years in proportion to the continuous increase in hardware capabilities, is still formidable; the storage requirements for resolution of all scales of three-dimensional turbulent flow scale with the $9/4$ – th power of an appropriately defined flow Reynolds number. As a matter of fact, the resolution requirements for a simulation through laminar-turbulent transition into turbulent flow are still higher (e.g. Gilbert and Kleiser 1988) owing to the steep gradients developing during the multi-spike stages of transition. Furthermore, compressibility generally lowers the growth rates of the most amplified linear disturbances in comparison with those in incompressible flow. Consequently, instability analyses of three-dimensional compressible flows using DNS are still rare and when performed are restricted to a small subspace of parameters. Notable examples of compressible flow instability analyses based on DNS have started to appear in the literature (e.g. Pruett and Zang 1992, Zhong 1998). Their obvious strength is that both linear and nonlinear stages of flow instability can be tackled in a self-consistent manner.

The second point is rather more subtle and is related with the potential of confusion of the *different* types of local or global linear instabilities, which potentially coexist in the problem and are all resolved by the DNS. The self-contained work to be found as section 6 of this report elucidates this point in detail. Here it suffices to stress the difference between an *ordinary* differential equation based linear theory, such as an Orr-Sommerfeld type of analysis, and one in which the *partial* differential equation eigenvalue problem is solved. Another point that deserves mention here is that for flows with a mild variation in one spatial direction Herbert (1997 and

references therein) has proposed the concept of parabolised stability equations (PSE) as an alternative tool to both an Orr-Sommerfeld type of analysis and DNS. Using the PSE linear and nonlinear instability analysis results inaccessible to the classic linear theory (and obtainable by DNS) can be successfully recovered at a negligible fraction of the effort required by DNS. However, when the basic flow to be analysed is essentially two- or three-dimensional PSE is inapplicable to its instability analysis. There is clearly room for instability analysis tools beyond a local linear theory based on an Orr-Sommerfeld type of equation and alternative to both DNS and PSE.

Such an analysis tool may be developed within the framework of a global linear instability theory the principles of which are discussed in section 4 and detailed in section 6 b (iii). This theory is analogous in spirit, if not in detail, to the local linear analysis in considering the flowfield as composed of a steady (or time-periodic) so-called 'basic-flow' part upon which small-amplitude three-dimensional disturbances are superimposed. The key difference between global and local theory is that in the former both the basic flow and the amplitude functions of the linear perturbations are essentially *two- or three-dimensional* nonperiodic functions of the respective resolved spatial coordinates. The resulting freedom with the boundary conditions to be imposed on the elliptic global problem permits the recovery of much wider classes of linear instabilities when compared with those delivered by the local analysis. The development of the global linear disturbances in time is studied through the solution of a large non-symmetric complex generalised eigenvalue problem in which the governing equations may be recast upon substitution of the decomposition and linearisation about the basic state. Owing to the orders-of-magnitude higher computing effort compared with the classic linear analysis, global linear analysis results are slowly emerging in the literature, mainly confined to flows possessing special symmetries which reduce the computational effort related with the solution of the eigenvalue problem (e.g. Tatsumi and Yoshimura 1990, Hall and Horseman 1991, Lin and Malik 1996). An incompressible global linear analysis algorithm was developed, in primitive variables and without the restriction to flows with special symmetries, by Theofilis (1998c); the algorithm has been employed, amongst other flows, to the discovery of global instability in separated flat-plate boundary layer flow (Theofilis *et al.* 2000) while its predictions in the classic lid-driven cavity (Theofilis 2000) are in excellent agreement with the experiments of Aidun *et al.* (1991) and Benson and Aidun (1992). A recent review of the global linear analysis results is presented by Theofilis (2001).

The present report is the first step towards global linear instability analysis of three-dimensional flowfields over elliptic cones at hypersonic speeds. To this end, we discuss here the basic flows which form the variable coefficients of the partial differential equation eigenvalue problem at a small representative class of the parameter values at which the analyses will ultimately be performed. The essentials of the numerical issues surrounding the generation of the basic flows are discussed first and laminar steady-state solutions of the equations of motion are subsequently presented. We use this report to illustrate characteristic compressible flowfields recovered at constant Reynolds number and increasing angle of attack and Mach number, keeping for the most part of this work the same resolution of three-dimensional space. Grid adaptation was found to be necessary as the Mach number increases, on account of increasingly stronger discontinuities and steeper gradients in the flow. The necessary but computationally intensive grid refinement studies, which will assess the adequacy of the recovered solutions for an instability analysis†, are left to be addressed when the analysis will be performed at specific sets of parameters.

The analytical description of the elliptic cone surface in a body-fitted cartesian coordinate system $Ox'y'z'$ is provided by one of the roots x' of the equation

† f.e. in terms of convergence of second wall-normal and azimuthal derivatives

$$-\frac{x'^2}{a^2} + \frac{y'^2}{b^2} + \frac{z'^2}{c^2} = 0, \quad (1.1)$$

where a, b, c are the semiaxes of the elliptic cone. The geometry of interest is schematically depicted in figure 1. In this figure the angles of attack α and bank β are also shown. Interestingly, an effect of a nonzero angle β on the global instability analysis results is only to be expected when $\alpha \neq 0$. In that case, at each value of the angle of attack values of angle of bank $0 \leq \beta \leq \pi/2$ must be examined in order for the global instability on the elliptic cone to be fully understood. If $\alpha = 0$, on the other hand, the basic flowfields are invariant against a change in β and the number of parameters in the problem is reduced by one. Another simplification of the global eigenvalue problem in the limiting case $\alpha = 0$, to be discussed in detail in what follows, is the ability to perform an inviscid global analysis in order to extract the essential flow physics while reducing the computing effort. This is achieved by use of the generalised (within the framework of global linear theory) compressible Rayleigh equation, derived and presented for the first time as part of the present work. Further, following the recent discovery of the connection of numerical residuals in steady flow calculations to global linear flow eigenmodes it has become clear that the basic flow issue cannot be treated independently from that of the global linear instability analysis, if the latter is to be performed in a self-consistent manner.

In the following section 2 we discuss essential elements of the approach taken for the generation of basic flow data. In section 3 results on model problems, obtained by employing the AUSMDV scheme chosen for the generation of the basic states, are presented before our attention is focussed on the three-dimensional laminar flowfields on an elliptic cone at several Mach number and angle of attack parameter values. The relation of the basic flows and the linear disturbances generated upon them is exposed in section 4. The outlook with respect to an inviscid analysis of the basic flows obtained is discussed in section 5, where the generalised Rayleigh equation is presented and discussed. In the light of the interplay between basic states and global linear disturbances alluded herein we present in section 6 a self-contained discussion elaborating on the connection between residuals in a direct numerical simulation aiming at recovery of a steady-state solution of the equations of motion and global linear eigenmodes. An efficient algorithm for the recovery of the sought steady-state using transient data is presented. Closing remarks are furnished in section 7.

2. The Basic Flow Computation

(a) Governing equations

Flow is taken to be described by the system of the compressible continuity, Navier-Stokes and energy equations written in conservative form as

$$\frac{\partial \mathbf{q}}{\partial t} = \frac{\partial \{\mathbf{F}_c + \mathbf{F}_v\}}{\partial x} + \frac{\partial \{\mathbf{G}_c + \mathbf{G}_v\}}{\partial y} + \frac{\partial \{\mathbf{H}_c + \mathbf{H}_v\}}{\partial z}, \quad (2.1)$$

with the distinction between convective $(\mathbf{F}_c, \mathbf{G}_c, \mathbf{H}_c)^T$ and viscous $(\mathbf{F}_v, \mathbf{G}_v, \mathbf{H}_v)^T$ fluxes being made on grounds related with the numerical discretisation. The Cartesian spatial coordinates are denoted by x, y and z respectively and t denotes time. The vector of unknowns is $\mathbf{q} = (\rho, \rho u, \rho v, \rho w, E)^T$, ρ is the fluid density, $(u, v, w)^T$ are the velocity components in the directions of x, y and z and E is the internal energy of the fluid. The form of the fluxes is to be found in any textbook on compressible flow and numerical solutions thereof (Hirsch 1988); the convective fluxes, of interest here from the point of view of an inviscid global linear analysis, are given by

$$\mathbf{F}_c = \begin{pmatrix} \rho u \\ \rho u^2 + p \\ \rho uv \\ \rho uw \\ u(E + p) \end{pmatrix}, \quad \mathbf{G}_c = \begin{pmatrix} \rho v \\ \rho uv \\ \rho v^2 + p \\ \rho vw \\ v(E + p) \end{pmatrix}, \quad \mathbf{H}_c = \begin{pmatrix} \rho w \\ \rho uw \\ \rho vw \\ \rho w^2 + p \\ w(E + p) \end{pmatrix}. \quad (2.2)$$

For the purposes of the instability analysis it is convenient to recast the inviscid part of the energy equation in one of the possible non-conservative forms

$$p_t + \gamma p \left(\frac{\partial u}{\partial x} + \frac{\partial v}{\partial y} + \frac{\partial w}{\partial z} \right) + (u \frac{\partial p}{\partial x} + v \frac{\partial p}{\partial y} + w \frac{\partial p}{\partial z}) = 0. \quad (2.3)$$

One point which deserves consideration is whether a perfect gas assumption may be made to close the system of equations; the decision depends on the Mach number values at which global linear instability analysis of the flow is to be performed and affects the calculation of both the basic flow and the instability results. If a perfect gas assumption is made, density, pressure p , temperature T and total energy of the gas are related by

$$\gamma M^2 p = \rho T, \text{ and } p = (\gamma - 1) \left(E - \frac{1}{2} \rho \mathbf{v}^2 \right) \quad (2.4)$$

where γ is the ratio of specific heat coefficients under constant pressure and constant volume, $\gamma = c_p/c_v$, and $\mathbf{v}^2 = (u^2 + v^2 + w^2)$ is the kinetic energy of the fluid per unit mass. Dimensionless numbers characterising the flow are the Mach number M , Reynolds number Re and Prandtl number Pr , evaluated at appropriate conditions and respectively defined as

$$M = u/a_s, \quad Re = \rho u L / \mu, \text{ and } Pr = \mu c_p / k, \quad (2.5)$$

with u the magnitude of a typical velocity, a_s the speed of sound, L a typical length scale in the flow, μ the dynamic viscosity of the medium and k the thermal conductivity coefficient. A further issue arising in hypersonic flow is whether the viscosity may be taken to be a function of temperature alone and, if so, what the most appropriate law describing its dependence on temperature is. In classic linear analyses of compressible flow instability (Mack 1969, 1984) a power-law or Sutherland's formula are used, depending on whether the basic flow model adopted is based on a reduced or the full system of the equations of motion.

(b) *Flux-splitting and the AUSMDV scheme*

A plethora of numerical schemes exist for the discretisation of (2.1) most of which use central differencing for the calculation of the viscous fluxes $(\mathbf{F}_v, \mathbf{G}_v, \mathbf{H}_v)^T$ and different prescriptions for the calculation of the convective fluxes $(\mathbf{F}_c, \mathbf{G}_c, \mathbf{H}_c)^T$. A basic distinction exists between shock-capturing and shock-fitting approaches for the discretisation of the convective fluxes. We discuss here briefly the scheme utilised, namely the AUSMDV. It should be noted that a wealth of modern accurate compact finite-difference alternative numerical methods exist, f.e. the shock-capturing approach of Visbal and Gaitonde (1998) or the shock-fitting algorithm of Zhong (1998, 1999).

The work of Liu and co-workers (e.g. Wada and Liu 1994) presents the essentials of an AUSMDV discretisation. For the sake of exposition of the algorithm used here we adhere with presentation in one spatial dimension. As a first step, it is recognised that the flux vector is composed of momentum flux and pressure force terms, which are treated independently as

$$\mathbf{F}_c = u \begin{pmatrix} \rho \\ \rho u \\ \rho e \end{pmatrix} + \begin{pmatrix} 0 \\ p \\ pu \end{pmatrix}, \quad (2.6)$$

where $E = \rho e$. A consistent pressure splitting follows, according to which $\mathbf{F}_c = \mathbf{F}^+ + \mathbf{F}^-$ with

$$\mathbf{F}^+ = \max(u, 0) \begin{pmatrix} \rho \\ \rho u \\ \rho e \end{pmatrix} + \begin{pmatrix} 0 \\ p^+ \\ (pu)^+ \end{pmatrix}, \quad \mathbf{F}^- = \min(u, 0) \begin{pmatrix} \rho \\ \rho u \\ \rho e \end{pmatrix} + \begin{pmatrix} 0 \\ p^- \\ (pu)^- \end{pmatrix}, \quad (2.7)$$

and

$$p^+ = p \begin{cases} 0, & M \leq -1 \\ (1 + M)/2, & |M| < 1 \\ 1, & M \geq 1 \end{cases}, \quad p^- = p \begin{cases} 1, & M \leq -1 \\ (1 - M)/2, & |M| < 1 \\ 0, & M \geq 1, \end{cases} \quad (2.8)$$

$$(pu)^+ = p \begin{cases} 0, & M \leq -1 \\ (u + a_s)/2, & |M| < 1 \\ u, & M \geq 1 \end{cases}, \quad (pu)^- = p \begin{cases} u, & M \leq -1 \\ (u - a_s)/2, & |M| < 1 \\ 0, & M \geq 1. \end{cases}$$

The extension of this idea to multiple spatial dimensions is straightforward. As it stands this scheme is only first-order accurate in space, while for realistic applications at least second order accuracy is necessary away from discontinuities.

(c) *Numerical discretisation*

Temporal discretisation of (2.1) is performed using a multi-stage Runge-Kutta scheme. For the three-dimensional problem at hand the key additional issue arising, besides the choice of a spatial discretisation scheme, is that of adequate spatial discretisation. This is addressed by performing a surface discretisation of (1.1) first, followed by a consistent discretisation of three-dimensional space in which the elliptic cone is embedded. As a matter-of-fact it has been observed that for the second-order scheme used best results can be achieved when the three-dimensional spatial discretisation is subdivided in two parts, first wrapping a structured grid around the elliptic cone, which is generated conforming with the surface discretisation and then discretising space between the structured glove wrapped around the cone and the far-field boundaries by an unstructured grid generated by an advancing front Delauney algorithm.

The grid used for the $\alpha \neq 0$ calculations to be presented shortly, discretising space between $[-x_\infty \leq x \leq x_\infty] \times [0 \leq y \leq y_\infty] \times [-z_\infty \leq z \leq z_\infty]$ with $x_\infty = y_\infty = z_\infty = 20$, is shown in figures 2-4. The dimensions of the elliptic cylinder are determined by taking the aspect ratio to be constant $A = 3$ and the length of the cone $a = 1$. The relevant parameters of Jorgensen

(1958) determine the other two semiaxes of the cone, $b = 0.87/3.67$ and $c = b/3$. In figure 2 a global view of the discretisation of a half elliptic cone model surface and that of the far-field and symmetry boundaries is shown, in which the different degrees of refinement of the neighbourhood of the object and the far-field can also be seen. A detailed view of the same is presented in figures 3 and 4 viewing the half model from upstream and downstream, respectively. In all three figures the discretisation of the interior of the flowfield is not shown for clarity; in the latter two figures the structured grid, its fine distribution around the model as well as its merging into the unstructured far-field grid can be seen.

Thanks to the hybrid-grid technique used the number of total grid elements contained in this grid is confined to $\sim 5.3 \times 10^6$ resulting in ~ 100 Mbytes of memory required for the storage of the surface- and ~ 300 Mbytes for that of the field-discretisation, respectively; a much higher number of gridpoints would have been necessary had the structured grid in the neighbourhood of the surface been extended to the farfield. The resolution and storage requirements increase proportionately to the number of multigrid cycles or grid adaptation levels in case a multigrid or adaptive-grid solution algorithm is employed in order to accelerate convergence to or refine resolution of the steady-state solution desired. We will return to these points when we discuss basic flow results on the elliptic cone.

3. Basic Flow Results

(a) Validation of the AUSMDV scheme

The substantial progress of numerical algorithms for external aerodynamics over the last decades may be appreciated by referring to classic review articles which periodically summarise the state-of-the-art of the time. Such a work, discussing a wealth of nontrivial validation cases, is that of Woodward and Colella (1984). Besides establishing the characteristics of the scheme utilised for the recovery of the laminar steady-state basic flows on the elliptic cone, we engage in some validations in order to identify the limits of the chosen numerical approach on simple configurations; the conclusions drawn are then expected to carry weight in the three-dimensional geometry in question on which it is neither straightforward nor practical to perform a large number of numerical validation experiments.

The solutions of two one-dimensional Riemann problems are presented in figure 5. The initial conditions for the first problem were proposed by Sod (1978) and are $(\rho_L, M_L, p_L) = (1, 0, 1)$ and $(\rho_R, M_R, p_R) = (0.125, 0, 0.1)$ while those for the second problem, due to Lax (1954), are $(\rho_L, M_L, p_L) = (0.445, 0.698, 3.528)$ and $(\rho_R, M_R, p_R) = (0.5, 0, 0.571)$. The adequate representation of shocks and contact discontinuities at the resolution utilised can be seen in both cases. A third interesting one-dimensional problem, that of a blast wave, has been discussed by Woodward and Colella (1984). The periodic boundary conditions of the first two Riemann problems are replaced here by reflecting walls and the calculation is initialised with the values presented in table 1. Two strong shocks are generated and travel in opposite directions, are reflected by the walls and meet in the centre-part of the domain. The solution at $t = 0.38$ is shown in figure 6. While by visual comparison with the results obtained by the piecewise-parabolic method of Woodward and Colella (1984) the solution obtained appears acceptable, grid refinement reveals interesting (but not unexpected) properties of the AUSMDV method. Using current hardware technology extremely fine grids could be used, the solution at the aforementioned time being obtained within a few minutes of CPU time on a EV6 Alpha processor. In figure 7 the solution at the same time $t = 0.38$ is presented, obtained using $\Delta x = 5, 2, 1$ and 0.5×10^{-4} . In the upper part of this figure the convergence of the solution at the two highest resolutions can be seen. While the location of the shocks is adequately represented at all resolutions, the results at the coarsest resolution (which already uses double the number of points compared with those presented in figure 6) is seen to deliver inaccurate results on at least two counts. First, the details of the flow are smeared out in a manner typical of numerical discretisation schemes of low formal order of accuracy. Second, the peak value of density on the rightmost (expansion) structure is underpredicted, only acquiring its converged value at the highest resolutions. The enlargement of the region of the flow behind the leftmost shock reveals further details. Again, the coarsest resolution of 2000 uniformly distributed points smears the shock over a rather wide distance while as the resolution increases the slope increases but pointwise oscillations appear immediately adjacent to the shock; their amplitude diminishes with further increase of resolution. In table 2 the predicted wall values of the primitive variables are presented. It may be seen that even at the highest resolution no satisfactory convergence has been achieved, at least from the point of view of instability analysis which requires accurate prediction of wall-values including their second derivatives. Of course, such resolutions are unattainable in the context of the three-dimensional solutions sought in the framework of the current investigations and a direct consequence of the first-order accurate scheme chosen. The conclusions drawn from the present one-dimensional validation runs is that the AUSMDV method is capable of predicting accurately the features of unsteady one-dimensional flows encompassing strong shocks, and is much simpler in comparison with elaborate traditional flux-vector splitting schemes, e.g. that due to van Leer. However, for the subsequent instability analysis one should employ either extremely high resolutions (only affordable in one or maximally two spatial dimensions), or solution techniques based on grids

other than uniform (f.e. adaptive grids). We will return to this subject shortly, when we present the elliptic cone results.

Before doing so, however, we discuss the performance of the AUSMDV scheme in two spatial dimensions. A plethora of nontrivial two-dimensional validations have been proposed in the literature, of which we have focussed our attention on the two-dimensional analogon of Sod's problem (in which the initial conditions of the one-dimensional problem are imposed in both spatial directions) and the two cases presented by Woodward and Colella (1984). The result of the two-dimensional Sod problem may be seen at time $t = 2$ in figure 8. The interesting oblique pattern generated by the interaction of shocks and expansion waves and its adequate resolution may be seen in this result. However, this success did not carry over to the two-dimensional problems discussed by Woodward and Colella, at least when the first-order accurate AUSMDV scheme was used. In both the cases of flow over a step and double Mach reflection difficulties with both the accurate implementation of boundary conditions and the diffusive nature of the first-order accurate algorithm have been experienced. While further experimentation has been postponed until the elliptic cone flows have been generated, the implication for the solutions sought is clear, namely that a higher-order accurate version of the discretisation scheme has to be utilised for the generation of the elliptic cone laminar solutions; this conclusion is in line with that drawn earlier on the number of discretisation points necessary for convergence in the one-dimensional validation cases presented. With this experience generated, we turn our attention to the elliptic cone next.

(b) *Compressible three-dimensional laminar flows over an aspect ratio 3 elliptic cone*

In comparison with the validation cases presented the calculation of flow over the elliptic cone presents several additional challenges, the most obvious of which is that related with flow separation. A decision has to be made at the stage of designing the computationally intensive solutions whether to embed the cone into a calculation domain in which the farfield boundaries are placed far away from the three-dimensional conical object or whether the downstream farfield boundary and the surface of the elliptic cone meet. We have chosen the first approach, in anticipation of inconsistencies in the formulation of the boundary conditions at the junction of farfield boundary and cone surface. While no such problem is expected if the downstream farfield boundary is placed several cone lengths downstream of the elliptic cone, one must decide on the form of the base surface; owing to its simplicity a flat (elliptic) base was chosen. This in itself generates a new issue, namely unsteady flow separation at the base, which is distinct from that expected on account of increasing angle of attack but will influence the latter in the context of a three-dimensional calculation, at least in the subsonic regime. Since a steady laminar basic flow is required for the global instability analysis the flow Reynolds number must be kept low enough for such a state to exist. To our knowledge the choice of a Reynolds number which results in steady separation on the configuration in question is an open question but experience with the classic Kármán vortex street suggests that the Reynolds number required to achieve steady separation at base may need to be taken rather small. On the other hand, given sufficient length of the cone at a moderately high Reynolds number the flow will become turbulent (Kimmel *et al.* 1997, 1999) and a global instability analysis would be obsolete. With both considerations in mind we have taken a cone length $a = 1$ and $Re = 10^3$ throughout the following calculations. Additionally, adiabatic wall conditions were imposed and results were obtained in SI units.

In order to avoid convergence problems associated with flow separation in the framework of an unsteady calculation, which would be associated with amplification of the global flow eigenmodes† we chose to perform steady basic flow calculations. It should be stressed at this point that the subsequent global instability analysis has the potential to confirm or refute this

† see detailed discussion in § 6

choice in terms of the damping or amplification of the global eigenmodes recovered. The true physical solution, at least in its linear limit, can be predicted using a two-step approach; first the steady-state equations of motion are iterated until a steady-state solution is recovered and subsequently a global instability analysis of the obtained steady solution is performed. If all eigenmodes recovered by the global analysis are damped the steady-state solution satisfies the unsteady equations of motion as well; if unstable eigenmodes exist the computed steady-state solution will be linearly modified in the manner predicted by the global instability analysis.

Parameters which have to be considered other than the Reynolds number are the angles of attack α and bank β , defined in the schematic representation of the elliptic cone geometry in figure 1; these determine, respectively, flow separation from the elliptic cone surface and symmetry-breaking of the flowfield around the cone. All calculations to be presented have been performed using $\beta = 0$ which led to the decision to impose symmetry about $y = 0$. Whether this decision is justified is left to be assessed by comparisons with three-dimensional solutions around the entire elliptic cone. Solutions around the entire cone are at least twice as expensive as those presented in what follows and have thus been left for future extensions/refinements of the present work. Taking $\alpha = 0$ as well results in the ability to perform calculations on one quarter of the elliptic cone, imposing symmetry about $z = 0$ also. The flowfields resulting in this limit are those closest to fulfilling the fundamental assumption of the global linear instability theory, according to which the flow dependence on two spatial directions, those defining the plane normal to the elliptic cone surface, dominate over that along the cone generator. However, this limiting case may not be as representative of realistic situations in which flow separation from the elliptic cone surface on account of $\alpha \neq 0$ and the consequent fulfillment of inviscid instability analysis criteria is the predominant flow feature. In the following calculations we have thus refrained from imposing symmetry about $z = 0$ and have considered two angles of attack, $\alpha = 10^\circ$ and 20° . Finally, the target Mach number M of interest corresponds to hypersonic flow, $M = 8$. We devised a straightforward but conservative strategy to achieve the latter target, commencing calculations at low Mach number and angle of attack and gradually increasing the values of both parameters as a steady state at a given pair of (M, α) is approached. In this process single (non-optimal) grid calculations are performed; close to the steady state a multigrid convergence acceleration technique can be employed and the gridpoint distribution may be optimised by following the particular flow features (e.g. high gradients). In this respect a database of steady states at intermediate parameter values has been generated for future reference. It should also be stressed here that at this stage of the present effort we are interested in trends as parameters change and not in the machine-accurate convergence of the solution at a single set of parameters. Hence we perform a large but reasonable number of iterations towards the steady state. On the hardware utilised (EV6 Alpha processor) 10^4 iterations were performed at each set of parameters at a cost of ~ 180 CPU hrs each. While no statement can be made regarding the convergence of these results prior to performance of simulations at the same parameters and higher resolutions, the reduction of the residuals in the iterative solution by approximately three orders of magnitude compared with the respective initial conditions warrants a qualitative description of the findings.

In figures 9-25 we present three-dimensional flowfields around the aspect ratio 3 elliptic cone in the range $0.5 \leq M \leq 4$. The actual calculation results have been mirrored about $y = 0$ in order to generate a three-dimensional impression. In these figures the primitive variables in the neighbourhood of the cone are shown as colour-coded contour lines drawn on two planes, the symmetry plane $y = 0$ when available and the plane meeting the cone at $x = 0.7$. We start at the subsonic Mach number $M = 0.5$ at which the results of figures 9-11 and 12-14, respectively pertaining to the angles of attack $\alpha = 10^\circ$ and 20° , are compared. Separation at the base of the cone is clearly visible in figures 9 and 11 while the contours of v in figure 10 indicate vortical motion near the surface of the elliptic cone. Note also that in both these and the results that follow $v(y = 0) \equiv 0$ on account of the imposed symmetry. However, it can be seen in the results

of $u(z < 0)$ and even clearer on those of $w(z > 0)$ that the condition of symmetry is only satisfied in the immediate vicinity of the cone and further iterations are necessary before the solution has converged in the far-field as well.

Turning to comparisons with the solution obtained at the larger angle of attack $\alpha = 20^\circ$ one notes that again, further iterations are necessary for the condition of symmetry across $y = 0$ to be satisfied. On the other hand, comparison of the results of figures 10 and 13 gives a visual impression of the strengthening of separation from the cone surface. A better visualisation of this result might have been possible by implementing the λ_2 vortex identification criterion of Jeong and Hussain (1995); this is currently in progress alongside detailed data analysis. What is clearly visible in the contours presented is that the separation zone at the base of the cone is substantially enlarged when the angle of attack increases. In an incompressible environment this would affect the flow on the cone surface itself; it is expected that as the Mach number increases the effect of this flow feature, or potential modifications to it, will not affect flow near the tip of the cone where the global analysis is envisaged to be performed. Nevertheless, a fairing of the cone base, for instance by smoothly blending the cone itself with a prolate spheroid/ellipsoid body, might moderate the strength of the separated area behind the cone; this direction is also currently being pursued. From the point of view of the global instability analysis, it is interesting to note that the condition necessary for the analysis, namely that flow gradients along the cone generators are much smaller than those along the wall-normal direction, appears to be fulfilled in the results at both angles of attack.

We next keep the angle of attack constant at $\alpha = 20^\circ$ and increase the free-stream flow Mach number to $M = 2$; the results for the primitive variables, obtained after a preset number of 10^4 iterations, which started using the solution presented in figures 12-14 as initial condition, are to be found in figures 15-19. From a physical point of view, the expected characteristic of supersonic flow Mach cone is to be seen in these results. The shock emanates from the cone tip while expansions are to be seen at the cone base as a result of the strong curvature jump. An interesting point may be made with respect to the global analysis of this flowfield in terms of its potential self-similarity with respect to translation along the x -spatial direction. In figure 20, in which the solution for w is replotted, one notices that a transformation might exist within a specific x -interval which reduces the dependence of the basic flow from three to two spatial dimensions. This issue is currently being examined; should such a transformation be established the original objective of the present effort to provide a two-dimensional basic state for the global instability analysis would be materialised in a manner consistent with the flow physics rather by an ad-hoc imposition of the global instability analysis condition on the basic flow. From a numerical point of view, the fact that there is room for improvement of resolution is also evident; additionally to the boundary layer which must be well resolved at all Mach numbers the shock wave poses new challenges to the grid presented in figure 2 in terms of resolution of both the neighbourhood of the cone tip as well as the Mach cone. One way to improve resolution is by local redistribution of the available gridpoints following some means of grid adaptation commensurate with the gradients in the flow.

The need for such a refinement of the solution approach became stronger at the higher Mach number of $M = 4$. While the qualitative features of the flow at this Mach number are analogous with those at $M = 2$, the shock is now stronger and thinner. We hence performed a large number of iterations using the solution at $M = 2, \alpha = 20^\circ$ as initial condition; however the rate of decay of residuals was unacceptably slow and we had to resort to grid adaptation, increasing the number of gridpoints by 30% compared with that shown in figure 2. Subsequently 10^4 more iterations were performed, producing the results shown in figures 21-25. Qualitatively, the obtained solutions appear to be sufficiently smooth, though not yet converged to machine accuracy. From these results it appears that flow separation at the base of the cone does not affect flow on the cone surface itself, the determining factors for the latter being the cone aspect

ratio and the angle of attack considered. However, as already stated, this conclusion is drawn on the basis of three-dimensional solutions of the *steady* equations of motion and its weight can only be verified after the global analysis has been performed. Our current efforts aim at recovery of solutions at the target Mach number $M = 8$ using the results at $M = 4$ as initial conditions. Though straightforward, the achievement of this target appears to be more challenging in terms of the computing effort required in comparison with the solutions at lower Mach numbers. Both systematic grid adaptation and multigrid algorithm have been found to be necessary in preliminary calculations. In parallel, we intend to pursue multigrid solutions in order to refine the results at all Mach numbers shown herein in order to achieve satisfactory convergence before embarking upon data probing and global instability analysis.

4. Global Linear Instability Theory

(a) *Small-amplitude disturbances superimposed upon a steady laminar flow*

Linear instability theory considers the amplification of small-amplitude perturbations superimposed upon a steady laminar so-called basic flow. In its most general form any flow quantity is decomposed into an $O(1)$ component denoted by \mathbf{Q}_b and an $O(\varepsilon)$ perturbation term denoted by \mathbf{Q}_p according to

$$\mathbf{Q}(x, y, z, t) = \mathbf{Q}_b(x, y, z) + \varepsilon \mathbf{Q}_p(x, y, z) \exp \Omega t + c.c. \quad (4.1)$$

The vectors $\mathbf{Q}_b = (\bar{\rho}, \bar{u}, \bar{v}, \bar{w}, \bar{p})^T$ and $\mathbf{Q}_p = (\hat{\rho}, \hat{u}, \hat{v}, \hat{w}, \hat{p})^T$ respectively denote the basic and disturbance fields, both of which are nonperiodic three-dimensional functions of space. Taking $\varepsilon \ll 1$ and substituting (4.1) into the governing system of equations the $O(1)$ basic-flow related terms are subtracted out, themselves taken to satisfy the governing equations (2.1) at this order. Linear terms of $O(\varepsilon)$ are retained while higher-order terms in ε are neglected. An eigenmode Ansatz in time is permissible on account of the independence of the coefficients of the linearised system of equations on time and complex conjugation is considered in (4.1) since both Ω and the disturbance eigenfunctions \mathbf{Q}_p may in general be complex, while both \mathbf{Q} and \mathbf{Q}_b are real. On the other hand, the $O(1)$ basic flow terms, including second spatial derivatives thereof, form the variable coefficients of the linear instability problem; the quality of the results of the instability problem critically depends on the quality by which the $O(1)$ terms are prescribed. We term the analysis based on (4.1) a *three-dimensional* linear instability analysis. The study of three-dimensional linear disturbances satisfying (4.1) can currently only be accomplished by a DNS for \mathbf{Q} , in which spatial derivatives are calculated in a decoupled (usually parallel) manner and either the linearised or the full nonlinear system of governing equations is marched in time until a regime of exponential amplification or decay of perturbations is identified and results for the temporal amplification rate of disturbances Ω are obtained through $\partial \mathbf{Q} / \partial t$ in the DNS signal. A point that should be stressed here regards the interplay of steady basic flow and three-dimensional global eigenmodes, namely that the very existence of a steady laminar three-dimensional basic state \mathbf{Q}_b suggests that *all* three-dimensional global linear disturbances of the flow are *stable*. Consequently, the performance of a global linear analysis by numerical solution of the eigenvalue problem, besides being intractable by current hardware technology, may be of modest interest from a physical point of view; the strength of a DNS-based instability analyses then is its ability to address nonlinear flow instability. Instability analyses of one-dimensional basic compressible flows that utilise DNS have a somewhat longer history (Erlebacher and Hussaini 1990, Pruett and Zang 1992) than linear analyses of two- and three-dimensional basic states which are slowly emerging (Pruett and Chang 1998; Zhong 1998, 1999).

Certain classes of basic flows may be taken to be homogeneous in one spatial direction while the other two directions are resolved. Specifically, if

$$\partial / \partial z \ll \partial / \partial x \text{ and } \partial / \partial z \ll \partial / \partial y, \quad (4.2)$$

holds in the basic flow problem, then the Ansatz

$$\mathbf{Q}(x, y, z, t) = \mathbf{Q}_b(x, y) + \varepsilon \mathbf{Q}_p(x, y) \exp i\{\lambda z - \Omega t\} + c.c. \quad (4.3)$$

can be considered for linear disturbances superimposed upon \mathbf{Q}_b . In this case the linear instability analysis may proceed either by means of DNS in a manner conceptually analogous with that used for the instability study based on (4.1) or by recasting the linearised system of equations as a partial-differential-equation based eigenvalue problem. In a temporal framework the objective becomes the determination of Ω and the associated amplitude eigenfunctions $\mathbf{Q}_p = (\hat{\rho}, \hat{u}, \hat{v}, \hat{w}, \hat{p})^T$ given a periodicity length L_z in the homogeneous z spatial direction which is

associated with the real wavenumber parameter λ through $\lambda = 2\pi/L_z$. Here $\mathbf{Q}_p = (\hat{\rho}, \hat{u}, \hat{v}, \hat{w}, \hat{p})^T$ are again three-dimensional functions of space but in contrast to those in (4.1) they are periodic in z . Prerequisite for the analysis in either a DNS or an eigenvalue problem framework is the existence of a steady (or time-periodic) laminar two-dimensional state $\mathbf{Q}_b(x, y)$. The results of the two approaches are identical as far as the leading instability eigenmode is concerned, while the eigenvalue problem has the additional merit over DNS of being able to provide details of the flow eigenspectrum which are difficult either to obtain or to identify in the DNS. We term the analysis based on Ansatz (4.3) a *two-dimensional* linear instability approach, while on account of the inhomogeneity of more than one spatial directions in both the basic flow problem and that of the corresponding linear theory, the instability theories based on either (4.1) or (4.3) are termed *global* linear analyses.

By contrast to the global analyses, consideration of two spatial directions as homogeneous and their consequent resolution by Fourier series leads to the classic *local* linear instability theory, in which the so-called *parallel-flow approximation* is made for the basic flow, such that

$$\partial \mathbf{Q}_b / \partial x \ll \partial / \partial y, \quad \partial \mathbf{Q}_b / \partial z \ll \partial / \partial y. \quad (4.4)$$

The corresponding decomposition becomes

$$\mathbf{Q}(x, y, z, t) = \mathbf{Q}_b(y) + \varepsilon \mathbf{Q}_p(y) \exp i\{\kappa x + \lambda z - \Omega t\} + c.c. \quad (4.5)$$

We term the local linear analysis based on (4.5) an *one-dimensional* analysis. The analogon of Ansatz (4.5) in a circular cone geometry is

$$\mathbf{Q}(r, \theta, z, t) = \mathbf{Q}_b(r) + \varepsilon \mathbf{Q}_p(r) \exp i\{n\theta + \lambda z - \Omega t\} + c.c. \quad (4.6)$$

where r denotes the radial, θ the azimuthal and z the downstream direction and n is taken to be an integer. While a DNS is also possible and indeed common practice as far as nonlinear instability analysis of compressible flows is concerned (e.g. Pruett and Zang 1992) an one-dimensional linear instability analysis is efficiently performed by means of numerical solution of the ordinary-differential-equation based generalised eigenvalue problem which results when (4.5) is substituted into the governing equations, the resulting system is linearised and terms of $O(\varepsilon)$ only are retained and solved for.

A local linear instability analysis is the first to be considered from a physical point of view and the most straightforward to perform as far as numerical solutions of the eigenvalue problem are concerned. Mack (1969, 1984) presented excellent summaries of the early work which led to the discovery of instability modes particular to compressible flow while Malik (1991) has discussed alternative numerical methods for the accurate and efficient solution of the ODE-based linear eigenvalue problem. Owing to the numerical challenges presented by the global linear analyses, the vast majority of linear instability work performed to-date is confined within the framework of the local approach based on (4.5). The one-dimensional basic flow $\mathbf{Q}_b(y)$ is obtained using approaches of different degrees of sophistication, based on numerical solutions of the boundary-layer, the Thin-Layer- or the Parabolised-Navier-Stokes equations (e.g. Kimmel *et al.* 1999). Within the framework of an inviscid one-dimensional linear instability analysis either a consistent approach is taken, typically in open systems, in which an inviscid steady laminar basic flow forms the variable coefficients of the linear eigenvalue problem or a non-rational approach is followed, typically in wall-bounded flows, in which viscosity is retained in the basic but not in the disturbance equations. On the other hand, within the framework of the two-dimensional linear instability analysis which forms the target of the present investigations, a steady laminar two-dimensional flow, i.e. a basic flow consisting of all three velocity components, density and pressure, all of which are functions of two spatial coordinates, must be provided.

(b) *Comments on the quality of the steady laminar basic flows*

As far as the basic flows \mathbf{Q}_b necessary for the analyses are concerned, short of resorting to DNS, these are obtained by means of approaches consistent with the subsequent linear instability analysis performed. Boundary layer (Mack 1969, Duck 1990, Karabis *et al.* 1999) and Parabolised Navier-Stokes (PNS) solutions (Kimmel *et al.* 1997, 1999) have been obtained, as well as solutions delivered by Navier-Stokes solvers appropriate for aerodynamic calculations (Dietz and Hein 1999). In all cases crucial for the success of the subsequent instability analysis is the accuracy by which the flowfield is described. Specifically, second derivatives of flow quantities in the radial direction must be accurately provided in the basic flow, a result straightforward to achieve in the context of boundary-layer but nontrivial in the context of PNS or Navier-Stokes computations. Indeed, in the elliptic cone problem of interest here, the basic flow issue is far from having been resolved in a satisfactory manner, with not only different approaches (e.g. boundary-layer vs. Navier-Stokes) but also different calculations within the same approach delivering results for the same configuration which are in substantial disagreement with each other (Kimmel *et al.* 1997). The implications for any type of subsequent linear instability analysis of discrepancies in the basic flow are evident.

Furthermore, regarding a global instability analysis an additional constraint is posed by the number of discrete points on which basic flow information can be provided so that the instability analysis may be performed within computationally affordable limits. In other words, what is necessary is a basic field \mathbf{Q}_b of highest quality on as low a number of points as possible. This requirement is typically fulfilled by employing numerical methods of high formal accuracy, typically spectral (Canuto *et al.* 1987) or compact finite-difference schemes (Visbal and Gaitonde 1998; Gaitonde and Visbal 1999). Experience with both instability analyses and DNS comparing spectral and high-order compact finite-difference methods has shown that either discretisation delivers satisfactory results, although the compact finite-difference methods typically require three-times the number of discretisation points per spatial direction in order to match the accuracy of the spectral methods (Theofilis 1998b). In the context of the coupled spatial discretisation of two spatial directions a spectral method may thus be preferable.

However, in compressible flow the issue of existence and location of shocks must be considered in conjunction with linear instability analysis. Instability analyses based on the decomposition (4.5) have to-date typically been performed on the assumption of exclusion of shocks from the computation domain. This assumption must be viewed critically in the context of one-dimensional compressible linear analyses, where two types of instabilities are known to exist, the compressible analoga of the Tollmien-Schlichting instabilities of incompressible flow (Tollmien 1929) and so-called Mack-modes particular to compressible flow (Mack 1969). Both types of eigenmodes decay rapidly outside the boundary layer but at a different rate, with the Mack modes penetrating deeper into the free-stream than the TS-like instabilities. In the case of conical geometries inviscid analysis has revealed the existence of instabilities the eigenfunctions of which are of oscillatory nature with their rate of decay being a nonlinear function of the respective eigenvalue (Duck 1990, Shaw and Duck 1992). The consistency of the results of such analyses has to be verified *a posteriori* by comparison with the shock location at specific flow conditions. For both local and global linear analyses the condition must be fulfilled that the shock position is well beyond the boundary-layer edge, such that either homogeneity of the perturbations or asymptotic boundary conditions based on the existence of realisable free-stream conditions may be imposed. These considerations have led to the identification of the two alternatives for the calculation of laminar steady-state basic flows in the present work, a shock-capturing scheme based on one variant of the AUSMDV method (Wada and Liu 1994) and a shock-fitting approach based on DNS (Zhong 1998). On account of satisfactory experience gathered with the former scheme on a related problem (Hein *et al.* 1999) the AUSMDV scheme was chosen.

5. The Generalised Rayleigh Equation

(a) Two-dimensional inviscid global linear analysis

Returning to the global instability problem, substitution of (4.1) into (2.1) leads to the linearised three-dimensional compressible continuity, Navier-Stokes and energy equations. In supersonic flow Mack (1969) has shown that the essential physical one-dimensional linear instability mechanisms may be well-understood from an inviscid analysis point of view, viscosity moderately modifying the quantitative results but not their qualitative trends. Here we discuss the inviscid linearised system first, as well as possible simplifications which make the global linear instability problem tractable from a numerical point of view. The assumption of a steady basic flow

$$\frac{\partial \bar{\rho}}{\partial t} = \frac{\partial \bar{u}}{\partial t} = \frac{\partial \bar{v}}{\partial t} = \frac{\partial \bar{w}}{\partial t} \equiv 0 \quad (5.1)$$

leads to the three-dimensional inviscid linearised disturbance equations, in symbolic form written as

$$\mathcal{A}_{3d} \mathbf{Q}_p = \mathcal{B}_{3d} \frac{\partial \mathbf{Q}_p}{\partial t}. \quad (5.2)$$

As has been mentioned, the discretisation of the linear operators \mathcal{A}_{3d} and \mathcal{B}_{3d} , in which the three-dimensional basic flow is used as the variable coefficients, by means of an eigenvalue problem in which all three spatial directions are treated in a coupled manner is impractical with current hardware technology and uninteresting from a physical point of view, since the existence of a converged three-dimensional steady-state solution is synonymous with stability of all three-dimensional global flow eigenmodes. In order to proceed with the analysis the simplification is made that the basic flow is independent of one spatial direction, say z , † i.e.

$$\frac{\partial \bar{\rho}}{\partial z} = \frac{\partial \bar{u}}{\partial z} = \frac{\partial \bar{v}}{\partial z} = \frac{\partial \bar{w}}{\partial z} = \frac{\partial \bar{p}}{\partial z} \equiv 0. \quad (5.3)$$

This permits the introduction in (5.2) of eigenmodes for the disturbance quantities in z and t , such that

$$\mathbf{Q}_p(x, y, z, t) = \hat{\mathbf{Q}}(x, y) \exp i(\lambda z - \Omega t) \quad (5.4)$$

and results in a linearised system of the form

$$\mathcal{A}_{2d} \hat{\mathbf{Q}} = \Omega \mathcal{B}_{2d} \hat{\mathbf{Q}}. \quad (5.5)$$

where $\hat{\mathbf{Q}} = (\hat{\rho}, \hat{u}, \hat{v}, \hat{w}, \hat{p})^T$ are the two-dimensional amplitude functions of the three-dimensional perturbations $\mathbf{Q}_p(x, y, z, t)$. The entries of \mathcal{A}_{2d} and \mathcal{B}_{2d} may be found in Appendix A. As it stands, the linearised system (5.5) offers no numerical simplification over the incompressible primitive-variables formulation discussed by Theofilis (1998c); indeed, the existence of an additional equation further aggravates the already large memory and runtime requirements for numerical solution of the partial-differential-equation based eigenvalue problem. If a complex shift-and-invert is performed in order for one, instead of two matrices appearing in (5.5) to be stored, in excess of $O(1.5\text{Gbytes})$ of storage for the resulting matrix are necessary; an interesting window of its eigenvalues may be calculated by Krylov subspace iteration methods at a cost of approximately one CPU hour of supercomputing time at a single flow condition. As a matter of fact, the solution of the compressible viscous global linear instability eigenvalue problem requires the same amount of computing effort as the inviscid problem (5.5) so that solution of the viscous problem may be preferable from the point of view of consistency of the basic flow and the global instability analysis approaches.

† Attention is drawn to the fact that the homogeneous direction is denoted by z in this section, and does not refer / is not to be confused with the coordinate system used on the elliptic cone

(b) Further simplifications

Several simplifications of the system of inviscid linear disturbance equations are offered by a basic flow which possesses a single velocity component, that in the direction of the wavenumber vector. Physically, this situation is realisable by considering zero-angle-of-attack flow over the elliptic cone. The system (5.5) then becomes

$$i\lambda\bar{w}\hat{\rho} + (\bar{\rho}D_x + \bar{\rho}_x I)\hat{u} + (\bar{\rho}D_y + \bar{\rho}_y I)\hat{v} + i\lambda\bar{\rho}\hat{w} = i\Omega\hat{\rho} \quad (5.6)$$

$$i\lambda\bar{\rho}\bar{w}\hat{u} + \hat{p}_x = i\Omega\bar{\rho}\hat{u} \quad (5.7)$$

$$i\lambda\bar{\rho}\bar{w}\hat{v} + \hat{p}_y = i\Omega\bar{\rho}\hat{v} \quad (5.8)$$

$$\bar{\rho}\bar{w}_x\hat{u} + \bar{\rho}\bar{w}_y\hat{v} + i\lambda\bar{\rho}\bar{w}\hat{w} + i\lambda\hat{p} = i\Omega\bar{\rho}\hat{w} \quad (5.9)$$

$$(\gamma\bar{p}D_x + \bar{p}_x I)\hat{u} + (\gamma\bar{p}D_y + \bar{p}_y I)\hat{v} + i\lambda\gamma\bar{p}\hat{w} + i\lambda\bar{w}\hat{p} = i\Omega\hat{p}. \quad (5.10)$$

A first simplification offered by (6.9-5.10) in comparison with (5.5) is that the former may be written as a real eigenvalue problem, requiring half the storage and computing time to solve in comparison with the latter problem. This fact may be seen clearly by eliminating $\hat{\rho}$, \hat{u} , \hat{v} and \hat{w} from (6.9-5.10), which results in

$$\mathcal{L}\hat{p} + \left[\left(\frac{\bar{p}_x}{\gamma\bar{p}} - \frac{\bar{\rho}_x}{\bar{\rho}} \right) - \frac{2\lambda\bar{w}_x}{[\lambda\bar{w} - \Omega]} \right] \hat{p}_x + \left[\left(\frac{\bar{p}_y}{\gamma\bar{p}} - \frac{\bar{\rho}_y}{\bar{\rho}} \right) - \frac{2\lambda\bar{w}_y}{[\lambda\bar{w} - \Omega]} \right] \hat{p}_y + \left(\frac{\bar{\rho}[\lambda\bar{w} - \Omega]^2}{\gamma\bar{p}} \right) \hat{p} = 0 \quad (5.11)$$

where $\mathcal{L} \equiv D_{xx} + D_{yy} - \lambda^2$, $D_x = \partial/\partial x$ and $D_y = \partial/\partial y$. This is the compressible counterpart of the Rayleigh equation within the framework of two-dimensional linear instability, in which the (Mach-number related) terms arising from compressibility are grouped in brackets. The incompressible analogon of (5.11) has been discussed by Hall and Horseman (1991) in the context of inviscid secondary instability of Görtler vortices.

From a numerical point of view it may be seen that the major difference between the incompressible and the compressible two-dimensional Rayleigh equations is that the former constitutes a linear while the latter is a cubic eigenvalue problem in Ω (in temporal) or in λ (in spatial) global linear theory. The nonlinearity in the eigenvalue might lead to using an iterative method for the solution of (5.11). In classic one-dimensional inviscid linear instability analyses (Mack 1969) one deforms the path of integration into the complex plane with a uniquely determined contour indentation; however, this uniqueness is lost in the context of inviscid global linear calculations and the issue of the correct integration path in analyses in which two complex spatial coordinates have to be taken simultaneously into account is far from having been resolved (Duck, personal communication). A direct solution algorithm, on the other hand, requires use of a companion matrix approach (Bridges and Morris 1984; Theofilis 1995) which results in a discrete problem whose size equals that of numerical solution of three equations. This is the second simplification offered by the two-dimensional Rayleigh equation in comparison with (6.9-5.10), namely the savings of two out of five equations, which results in a compressible two-dimensional global eigenvalue problem which is actually less expensive than viscous incompressible global linear instability in primitive variables (Theofilis 1998c).

The third simplification that the existence of a single basic velocity component permits is the possibility to impose symmetries in the sought disturbance solutions. Symmetries have been imposed in order to tackle the incompressible two-dimensional linear instability problems in a rectangular duct (Tatsumi and Yoshimura 1990) and in the infinite swept attachment-line boundary layer (Lin and Malik 1996). In the case of hypersonic flow over an elliptic cone the instability problem could be addressed in the context of numerical solutions in one quadrant alone, resulting in a matrix of size sixteen times smaller than that quoted earlier as necessary

for solution of the incompressible global linear instability problem in primitive variables. Such savings offers much more flexibility regarding good resolution of the global eigenfunctions in comparison with the full problem based on (5.5) and greatly facilitates parametric studies, albeit only in one of the physically interesting cases, that of zero-angle of attack flow. In order to address flow oncoming obliquely to the axis of symmetry of the elliptic cone the full problem (5.5) must be addressed and this is done best in the context of a consistent viscous calculation.

6. On numerical residuals and physical instabilities in steady-state fluid flow calculations

The preceding discussion repeatedly refers to the interplay between the existence of a steady-state solution of the equations of motion and amplification of global eigenmodes of this solution. Our concern here is with the identification of the origin and classification of the different qualitative forms which the numerically obtained transient solution assumes, when a DNS is performed in order to recover a steady-state solution of the system of equations governing fluid flow motion. For reasons of feasibility of the related partial-derivative eigenvalue problem we restrict the discussion to the recovery of two-dimensional steady basic states. Within the unifying framework of the extension of the linear instability theory of Tollmien (1929) to nonparallel two-dimensional steady basic states, residuals encountered in the simulation as the latter approaches convergence are either identified as or associated with the least damped of the two-dimensional global linear eigenmodes of the steady-state flow. The inability to converge to a steady-state is shown to be linked with the global linear flow eigenmodes approaching a neutrally stable state and interacting nonlinearly. With the origin of the residuals established, an algorithm is presented which permits recovery of the converged steady-state solution from transient data at substantially less computing effort compared with that necessary for the integration of the system of equations until convergence. Nonparallel linear instability theory of the three-dimensional eigenmodes of the converged two-dimensional steady-state may also be used to quantify the differences between the results of two- and three-dimensional DNS. Rather than remaining within the framework of the elliptic cone we use the well-documented two-dimensional incompressible lid-driven cavity flow as a demonstrator of these ideas.

(a) The problemacy with residuals

A steady-state solution \mathbf{Q}_b of the two-dimensional incompressible continuity and Navier-Stokes equations which describe flow in a prescribed two-dimensional domain Σ bounded by $\partial\Sigma$ is sought numerically. A plethora of numerical approaches for the accurate and efficient integration of either the steady or the unsteady equations of motion exists (e.g. Kim and Moin 1985) so that this problem may be considered solved in principle. However, in performing a time-accurate integration of the equations of motion one observes that, depending on the values of parameters such as the flow Reynolds number, in the limit of large time either a steady-state solution is obtained (e.g. Briley 1971) or unsteady, sometimes periodic, motion sets in (e.g. Pauley *et al.* 1990; Goodrich *et al.* 1990). The first question arising is what type of physical information is not considered by solving the steady as opposed to the unsteady equations of motion and what is the physical interpretation of the critical conditions beyond which the steady and unsteady formulations deliver different results. Both physical and numerical experience suggest that at low Reynolds numbers the two formulations may be used interchangeably. For example, essentially identical results with those of Ghia *et al.* (1982) and Schreiber and Keller (1983) have been obtained by a multitude of subsequent investigators who used the time-dependent equations of motion to describe flow in the square lid-driven cavity at Reynolds numbers up to $Re = 10^4$. On the other hand, the question of existence of a steady-state solution delivered by the unsteady version of the equations of motion at $Re = 10^4$ has been recently re-opened (E and Liu 1996) while it is well known that Hopf bifurcations exist in both the aspect-ratio two singular lid-driven cavity at $Re < 5000$ (Goodrich *et al.* 1990) and its regularised square counterpart at $Re \approx 10^4$ (Shen 1991). Consensus exists that at high Reynolds numbers the unsteady formulation is capable of delivering physics inaccessible to the steady version of the equations of motion; however, the origin of the differences between the results of the two formulations is presently not understood in a satisfactory manner. This is an alternative way of posing the first question, namely *what are the unsteady effects that manifest themselves at high Reynolds numbers?*

The next question arises from the very concept of two-dimensionality. The results of numerical

solutions of the three-dimensional analoga of the incompressible continuity and Navier-Stokes equations are in most cases in substantial qualitative and quantitative disagreement with their two-dimensional counterparts (Burggraf 1966) relegating two-dimensional DNS to the realm of academic interest. Within the scope of two-dimensional solutions being of interest three-dimensionality of physical space could be addressed by considering the flow to be independent of the third spatial direction. Homogeneity in this third direction could, in turn, be discussed in the context of a three-dimensional simulation, nonperiodic in the same two spatial directions as the two-dimensional one and periodic in the third. Advances in both algorithms and hardware and, not least, a considerable amount of knowledge on the differences between two- and three-dimensional numerical simulation results lead one to employ a DNS algorithm for flow with two nonperiodic and one periodic spatial direction (e.g. Spalart 1988) in the founded expectation that a three-dimensional so-called 'spatial' DNS is the only means capable of capturing all physical phenomena at a certain Reynolds number. The second question which may be posed at this point regards *the origin of the differences between the results of such two- and three-dimensional direct numerical simulations*. Associated, one may ask whether there exists an alternative means to spatial DNS for the description of the origins of the three-dimensional phenomena encountered.

The objective of the present effort is to put both questions within the unified framework of nonparallel linear instability of the steady state \mathbf{Q}_b . With the aid of the well-studied lid-driven cavity flow example we demonstrate the intimate link between numerical residuals in steady-state fluid flow calculations and linear two-dimensional eigenmodes of the converged steady state \mathbf{Q}_b . In the next section 6 (b) we present theoretical arguments, first analysing the behaviour of numerical residuals near convergence towards the steady-state solution from a numerical point of view. Subsequently we discuss solutions of the partial derivative eigenvalue problem governing linear instability of nonparallel two-dimensional steady-state flows, which shed light on residuals from a physical viewpoint. With the origin of residuals established from a physical point of view we construct and present an algorithm which permits recovery of the converged steady-state solution from transient results of the time-marching procedure, the latter taken well before convergence. In section 6 (c) we present results of application of the algorithm. First, the link between the results of nonparallel linear instability theory and different types of behaviour of numerical residuals in the DNS is demonstrated in this section and the aforementioned questions are answered. Subsequently, examples of recovery of the converged steady-state from transient data and assessment of the substantial savings in the computing effort materialised by use of the proposed algorithm are presented in this section. Closing remarks on the far-reaching implications of the present findings are made in section 6 (d) where suggestions for the extension of the analysis presented to compressible flow and flow with three nonperiodic spatial directions, such as that on the elliptic cone, are made.

(b) Theory

(i) ON RESIDUALS AND THE PHENOMENOLOGY OF THEIR BEHAVIOUR

While in an computation based on the steady system of equations governing fluid flow motion, such as that used for the basic flows on the elliptic cone presented in the previous section, residuals are viewed as departure from the steady state which have to be eliminated in an efficient manner by a specific solution algorithm (e.g. multigrid), in a time-accurate integration one may view transients as solutions of the equations of motion at every time-step and attempt to attach physical significance to characteristic patterns of their behaviour. By contrast to the previous sections here we concentrate on a time-accurate integration of the unsteady equations of motion and monitor the behaviour of residuals, defined as the difference between the transient solution and the converged steady state, in flow regimes where the latter exists. Physical space is three-dimensional; without loss of generality we may take the Cartesian coordinates x and y to be defined on Σ while z denotes the third spatial coordinate in the direction of Σ . Along the

first two coordinates the velocity vector has components u and v , while pressure is denoted by p . The equations of motion are marched in time t until $\mathbf{q} = (u, v, p)^T$, the transient solution, converges to \mathbf{Q}_b . Assuming that the latter exists and keeping the domain Σ unchanged, the following qualitative observations are made.

First, at any Reynolds number Re at which \mathbf{Q}_b exists, close to convergence the residuals decay exponentially in amplitude. Second, refinement of the discretisation of the domain Σ at constant Re results in convergence of the rate at which the residuals decay. Third, the (converged) rate of decay of residuals is a function of the flow Reynolds number; as Re increases residuals decay slower and the associated time of integration of the equations of motion until convergence increases. Fourth, on occasion, the residuals decay at a specific constant rate for a number of decades before this rate of decay changes to a different constant value at which residuals further decay until convergence. Fifth, systematically increasing Re , instead of monotonic convergence of residuals an oscillatory behaviour of \mathbf{q} in the neighbourhood of \mathbf{Q}_b is observed. Ultimately, a value of Reynolds number is reached past which no \mathbf{Q}_b exists. At first sight the existence of a physical mechanism which unifies such diverse patterns of behaviour of the numerical solution seems unlikely.

(ii) A NUMERICAL POINT OF VIEW ON THE BEHAVIOUR OF RESIDUALS NEAR CONVERGENCE

However, it is straightforward to provide an explanation of the first observation on the behaviour of residuals, which also provides a handle to the link between numerical residuals and physical flow instabilities. We assume that the solution \mathbf{q} is close to converging to the sought two-dimensional field $\mathbf{Q}_b = (\bar{u}, \bar{v}, \bar{p})^T$ such that it may be decomposed into the latter and small two-dimensional residuals $\tilde{\mathbf{q}}_{2D} = (\tilde{u}_{2D}, \tilde{v}_{2D}, \tilde{p}_{2D})^T$ superimposed upon it, according to

$$\mathbf{q}(x, y, t) = \mathbf{Q}_b(x, y) + \varepsilon \tilde{\mathbf{q}}_{2D}(x, y, t), \quad (6.1)$$

with $\varepsilon \ll 1$. We next substitute the decomposition (6.1) into the continuity and Navier-Stokes equations and assume that the steady-state solution satisfies the equations of motion at $O(1)$, such that it may be subtracted out of the resulting system at this order. Subsequently, based on the smallness of the amplitude of the residuals, we linearise about \mathbf{Q}_b and rearrange the system at $O(\varepsilon)$ such that the vector of residuals represents the unknowns; terms of $O(\varepsilon^2)$ are neglected. Since the coefficients of the resulting linear system of equations for the determination of $\tilde{\mathbf{q}}_{2D}$ at $O(\varepsilon)$ are independent of time t we may introduce an eigenmode decomposition in this coordinate, according to

$$\tilde{\mathbf{q}}_{2D}(x, y, t) = \hat{\mathbf{q}}_{2D}(x, y) e^{\sigma t} \quad (6.2)$$

with $\hat{\mathbf{q}}_{2D} = (\hat{u}_{2D}, \hat{v}_{2D}, \hat{p}_{2D})^T$. The physical significance of the parameter σ will be discussed shortly; from a numerical point of view it represents the rate at which the residuals $\tilde{\mathbf{q}}_{2D}$ decay in the neighbourhood of \mathbf{Q}_b . For simplicity we present only the real part of the admissible solutions of (6.2) although it is clear that both $\hat{\mathbf{q}}_{2D}$ and σ may, in general, be complex while $\tilde{\mathbf{q}}_{2D}$ is always real. Convergence of the solution \mathbf{q} towards \mathbf{Q}_b may be monitored by reference to either the local behaviour of the solution \mathbf{q} at a position (x_0, y_0) on Σ or by monitoring a suitably defined global criterion such as the energy contained in the residuals $\tilde{\mathbf{q}}_{2D}$; alternatives have been discussed by Theofilis (1998a). Here we follow the first approach and recover the parameter σ by monitoring the solution at two time-levels, $t - \Delta t$ and t , where Δt may but need not be the time-step in the numerical solution algorithm. Combining (6.1) and (6.2) it follows that the time-behaviour of the solution may be monitored by

$$\sigma = \ln[\mathbf{q}^t / \mathbf{q}^{t-\Delta t}] / \Delta t \approx d \ln[\mathbf{q}^t] / dt, \quad (6.3)$$

where

$$\mathbf{q}^t = |\mathbf{q}(x_0, y_0, t) - \mathbf{Q}_b(x_0, y_0)|. \quad (6.4)$$

The approximation in (6.3) holds as equality in the case of linear dependence of $\ln[\mathbf{q}^t]$ on time t . Decay of residuals is indicated by $\sigma < 0$. A first statement is thus in place without reference to a particular flow, through the analytical result that an exponential decay of residuals near convergence should be observed as a consequence of the separability of the linearised system of equations for the determination of residuals in time.

(iii) A PHYSICAL POINT OF VIEW BASED ON NONPARALLEL LINEAR INSTABILITY THEORY

Explanation of the further observations made in section 6 b (i) requires calling upon an extension of the classic linear instability theory proposed by Tollmien (1929), which describes the behaviour of small-amplitude disturbances superimposed upon an one-dimensional steady-state basic profile, into a new theory which is concerned with small-amplitude perturbations superimposed upon a steady two-dimensional field. In so doing, the many and often questionable assumptions related with the so-called parallel-flow approximation are relaxed and the linear instability of nonparallel basic states may be analysed. The penalty to be paid in resolving two spatial dimensions simultaneously is the need for numerical solution of a partial-derivative-based eigenvalue problem instead of the straightforward ordinary-differential-equation-based system of the Orr-Sommerfeld and Squire equations (Drazin and Reid 1981). One of the early successes of the nonparallel two-dimensional linear instability analysis was the discovery of inviscid short-wave instability of two-dimensional eddies by Pierrehumbert (1986) while the first viscous linear analysis in two non-periodic spatial dimensions known to us is the work of Lee *et al.* (1989) on the instability of flow in a rectangular enclosure under the influence of gravity and temperature gradient. More recent viscous analyses, in step with modern developments in algorithms and hardware, have been presented by Theofilis (1998c).

We re-interpret the transient solution \mathbf{q} in three-dimensional physical space as one composed of small-amplitude three-dimensional perturbations $\tilde{\mathbf{q}} = (\tilde{u}, \tilde{v}, \tilde{w}, \tilde{p})^T$ superimposed upon $\mathbf{Q}_b = (\bar{u}, \bar{v}, \bar{w}, \bar{p})^T$, the latter again taken to be two-dimensional. Linearisation about \mathbf{Q}_b is permissible on account of the smallness of perturbations compared with the steady-state \mathbf{Q}_b and the resulting system for the determination of $\tilde{\mathbf{q}}$ is separable in both t and z on account of the steadiness and the two-dimensionality of the basic flow \mathbf{Q}_b . Eigenmodes are introduced in these directions such that

$$\tilde{\mathbf{q}}(x, y, z, t) = \hat{\mathbf{q}}(x, y) e^{i[\lambda z - \Omega t]} + c.c. \quad (6.5)$$

with $\hat{\mathbf{q}} = (\hat{u}, \hat{v}, \hat{w}, \hat{p})^T$ and \hat{w} being the disturbance velocity component in the z -direction. Complex conjugation is introduced in (6.5) since $\tilde{\mathbf{q}}$ is real while all three of $\hat{\mathbf{q}}, \lambda$ and Ω may be complex. In the framework of a temporal linear nonparallel instability analysis used presently we write the linearised system in the form of an eigenvalue problem for the complex quantity Ω , while λ is taken to be a real wavenumber parameter describing an eigenmode in the z -direction. The real part of Ω is related with the frequency of the instability mode while its imaginary part is the growth/damping rate; a positive value of $\Omega_i \equiv \text{Im}\{\Omega\}$ indicates exponential growth of the instability mode $\tilde{\mathbf{q}}$ in time t while $\Omega_i < 0$ denotes decay of $\tilde{\mathbf{q}}$ in time. In the present framework the three-dimensional space comprises Σ extended periodically in z and characterised by a wavelength L_z in this direction which is associated with the wavenumber of each eigenmode, λ , through $L_z = 2\pi/\lambda$.

The system for the determination of Ω and $\hat{\mathbf{q}}$ takes the form of a complex nonsymmetric generalised eigenvalue problem

$$[\mathcal{L} - (\mathcal{D}_x \bar{u})] \hat{u} - (\mathcal{D}_y \bar{u}) \hat{v} - \mathcal{D}_x \hat{p} = -i\Omega \hat{u}, \quad (6.6)$$

$$-(\mathcal{D}_x \bar{v}) \hat{u} + [\mathcal{L} - (\mathcal{D}_y \bar{v})] \hat{v} - \mathcal{D}_y \hat{p} = -i\Omega \hat{v}, \quad (6.7)$$

$$-(\mathcal{D}_x \bar{w}) \hat{u} - (\mathcal{D}_y \bar{w}) \hat{v} + \mathcal{L} \hat{w} - i\lambda \hat{p} = -i\Omega \hat{w}, \quad (6.8)$$

$$\mathcal{D}_x \hat{u} + \mathcal{D}_y \hat{v} + i\lambda \hat{w} = 0 \quad (6.9)$$

subject to appropriate boundary conditions on $\partial\Sigma$. The linear operator

$$\mathcal{L} = (1/Re) (\mathcal{D}_x^2 + \mathcal{D}_y^2 - \lambda^2) - \bar{u}\mathcal{D}_x - \bar{v}\mathcal{D}_y - i\lambda\bar{w}$$

with $\mathcal{D}_x = \partial/\partial x$, $\mathcal{D}_x^2 = \partial^2/\partial x^2$, $\mathcal{D}_y = \partial/\partial y$ and $\mathcal{D}_y^2 = \partial^2/\partial y^2$. Comparison of (6.1-6.2) and (6.5) reveals that the two formalisms are related in the limit $\lambda \rightarrow 0$. However, \hat{w} is not taken *a priori* to vanish within the framework of nonparallel linear instability; three-dimensionality of physical space is preserved and the existence of a two-dimensional steady-state solution \mathbf{Q}_b is the result of $\tilde{\mathbf{q}} \rightarrow 0$ as $t \rightarrow \infty$. The comparison of (6.1-6.2) and (6.5) highlights two further key ideas. On the one hand,

residuals acquire the physical interpretation of one of the linear eigenmodes which pertain to the steady-state \mathbf{Q}_b and have $\lambda = 0$;

on the other hand,

the rate of decay of the residuals σ is nothing but the damping rate Ω_i of this linear perturbation,

as delivered by numerical solution of the partial-derivative eigenvalue problem (6.6-6.9). Another question naturally arising concerns the physical behaviour of the system when the least stable member of the linear eigenspectrum which pertains to \mathbf{Q}_b and has $\lambda = 0$ becomes unstable. The answer is clearly that

the existence of an unstable ($\lambda = 0$)–eigenmode is mutually exclusive with the ability to obtain a converged \mathbf{Q}_b .

From the point of view of the global linear instability theory based on the partial derivative eigenvalue problem (6.6-6.9) the unsteady behaviour of two-dimensional flow may be related to ($\lambda = 0$)–eigenmodes approaching conditions of neutral stability and interacting nonlinearly.

The answer to the second question posed in section 6 (a) may now also be obtained without reference to a specific flow example. The existence of a steady-state \mathbf{Q}_b in a 2D numerical simulation is synonymous with the fact that all ($\lambda = 0$)–eigenmodes of the flow have $\Omega_i < 0$. Modes having $\lambda \neq 0$, on the other hand, may be either growing or decaying linearly. In case $\Omega_i < 0 \forall \lambda$, a three-dimensional numerical simulation performed at some parameters in a three-dimensional domain defined by Σ and an *arbitrary* periodic extent L_z in the z -direction will deliver *identical* results for a converged \mathbf{Q}_b compared with that of a two-dimensional simulation performed at the same parameters in the domain Σ . The situation changes in case a bracket of wavenumbers $\lambda \in [\lambda_1, \lambda_2]$ exists which corresponds to unstable modes. The largest wavenumber λ_2 defines a length $L_{z2} = 2\pi/\lambda_2$; if the three-dimensional simulation is performed with $L_z < L_{z2}$ again no difference is to be expected between its result for \mathbf{Q}_b and that of a two-dimensional simulation. Both will converge to the same steady-state solution \mathbf{Q}_b since all wavenumbers of modes defined by an L_z constrained as above correspond to $\Omega_i < 0$. However, if $L_z > L_{z2}$ at least one mode in the three-dimensional simulation will be unstable, which will result in the two- and three-dimensional simulations producing different solutions.

We return to the observation of oscillatory behaviour of the residuals near convergence and

differentiate between exponentially decaying residuals of either sinusoidal or apparently non-linear nature. A linear decay of $\ln[\mathbf{q}^t]$ is a consequence of $(\lambda = 0)$ —linear eigenmodes being stationary, i.e. having $\Omega_r \equiv \text{Re}\{\Omega\} = 0$. However, other stable two-dimensional member of the eigenspectrum of \mathbf{Q}_b need not correspond to stationary modes; damped travelling modes having $\Omega_r \neq 0$ will manifest themselves in the time-accurate simulation as residuals of sinusoidal character the magnitude of which decays exponentially. On the other hand, the unambiguously linear dependence of $\ln[\mathbf{q}^t]$ on t in the neighbourhood of \mathbf{Q}_b is the consequence of the existence of a spectrum comprising modes which are clearly separated in parameter space from one another. The co-existence of several two-dimensional eigenmodes of approximately the same damping rate can lead to their nonlinear interaction and difficulty to observe a behaviour governed by non-parallel linear instability theory. Comparison of power spectral analysis of the time-dependent DNS signal and the results of the partial-derivative eigenvalue problem (6.6-6.9) may shed light upon the two-dimensional eigenmodes involved in such a nonlinear interaction.

(iv) ON THE TIME OF INTEGRATION UNTIL CONVERGENCE

Straightforward rearrangement of (6.1-6.2) delivers an estimate of the time necessary (under linear conditions) for the least stable global mode present in the numerical solution to be reduced from an amplitude A_0 to a lower level A_1 , which may be calculated from

$$T_{A_1/A_0} = \ln(A_1/A_0)/(-\Omega_i), \quad (6.10)$$

where Ω_i is the damping rate of the mode in question. The worst case scenario in a time-accurate integration is that the solution will be attracted by the least-stable global eigenmode developing upon \mathbf{Q}_b and having $\lambda = 0$ throughout the course of the simulation. An upper bound for the time necessary for the steady-state to be obtained may then be offered by (6.10) in which Ω_i is the damping rate of this mode. Defining, for example, convergence as the reduction of an $O(1)$ residual by 10 orders of magnitude results in an integration time of $T_{10^{-10}} \approx 23/|\Omega_i|$. This is a conservative estimate since it is occasionally observed that other stronger damped eigenmodes will come into play early in the simulation and the least-damped eigenmode will only determine the late stages of the convergence process.

An associated point concerns the misconception which often exists that initialising the numerical solution for \mathbf{Q}_b at some Reynolds number from a state which is 'close' to the one desired, for instance using the converged solution at a somewhat different Reynolds number, may reduce the integration time in the context of a time-accurate solution. The present analysis shows this to be a misplaced expectation. If there exists an $O(1)$ deviation between the target solution and its initial estimate, the deviation has to be reduced in magnitude during an integration of the equations of motion for the length of time determined by the least damped two-dimensional $(\lambda = 0)$ —eigenmode at the specific Reynolds number. It is this eigenmode of the flow and not the initial state which determines the length of the integration time for \mathbf{Q}_b . The ideas discussed in the previous subsection on the other hand, lead to an algorithm application of which may save substantial amounts of the integration time necessary for reduction of residuals to machine-roundoff level.

(v) RECOVERY OF THE CONVERGED SOLUTION \mathbf{Q}_b FROM TRANSIENT DATA

Having identified small-amplitude residuals in the calculation as the least damped global two-dimensional eigenmodes of the flow, it is now possible to utilise this information in order to recover the converged steady-state solution from transient data, without having to pursue the time integration of the equations of motion until convergence in time is obtained. Combining (6.1), (6.2) and (6.5) one obtains

$$\mathbf{q}(x, y, t) = \mathbf{Q}_b(x, y) + \varepsilon \left[\hat{\mathbf{q}}_r \cos \Omega_r t - \hat{\mathbf{q}}_i \sin \Omega_r t \right] e^{\sigma t}, \quad (6.11)$$

where $\hat{\mathbf{q}}_r \equiv \text{Re}\{\hat{\mathbf{q}}\}$, $\hat{\mathbf{q}}_i \equiv \text{Im}\{\hat{\mathbf{q}}\}$ and $\hat{\mathbf{q}}$ is one of the $(\lambda = 0)$ -linear eigenmodes in (6.5). It should be stressed here that the following discussion is applicable to transient data for which (6.11) holds, namely, solutions for which the entire time-dependence of the solution is exhibited in the residuals; in other words, the present analysis is based on the self-consistent premises that $\partial \mathbf{Q}_b / \partial t = 0$. Further, it is noted that $\hat{\mathbf{q}}$ may but need not be the least-damped member of the eigenspectrum of \mathbf{Q}_b ; the only prerequisite for the validity of the following discussion is that the transient solution has reached a regime of exponential decay of residuals. A final point is that the signal near convergence need not be composed of a single damped eigenmode as (6.11) implies. However, the elements of the theory for the recovery of \mathbf{Q}_b from a signal being composed of several stationary ($\Omega_r = 0$) and travelling ($\Omega_r \neq 0$) linearly damped eigenmodes may be exposed by reference to (6.11) on which we focus our attention.

The calculation of \mathbf{Q}_b from transient data for \mathbf{q} follows in two stages. First, elementary signal analysis techniques deliver the results for Ω_r and σ . Second, once Ω_r and σ have converged in time (6.11) may be used to calculate \mathbf{Q}_b . The circular frequency Ω_r is calculated from the the period of oscillations in the time-signal of \mathbf{q} which, in turn, is identified by the maxima in the signal. Independently, in order to calculate σ we re-write (6.11) as

$$\frac{\partial^3 \mathbf{q}}{\partial t^3} + (\sigma^2 + \Omega_r^2) \frac{\partial \mathbf{q}}{\partial t} - 2\sigma \frac{\partial^2 \mathbf{q}}{\partial t^2} = 0. \quad (6.12)$$

This expression may be evaluated at those times that $\partial \mathbf{q} / \partial t = 0$ in the course of the time-integration, i.e. at the same times that Ω_r is calculated. At these times the magnitude of σ is given by

$$\sigma = \frac{1}{2} \frac{(\partial^3 \mathbf{q} / \partial t^3)}{(\partial^2 \mathbf{q} / \partial t^2)} \Big|_{(\partial \mathbf{q} / \partial t) = 0}. \quad (6.13)$$

In case $\Omega_r = 0$, a monotonic dependence of $\partial \mathbf{q} / \partial t$ on t is usually observed from the beginning of the calculation until convergence, with $\partial \mathbf{q} / \partial t = 0$ only at convergence. In this case, the magnitude of σ may be calculated using

$$\sigma = \frac{(\partial^2 \mathbf{q} / \partial t^2)}{(\partial \mathbf{q} / \partial t)}. \quad (6.14)$$

With σ and Ω_r converged in time (6.11) may be written as a linear system of three equations at three times $t_1 = t$, $t_2 = t + \Delta t$ and $t_3 = t + 2\Delta t$ for three unknowns, \mathbf{Q}_b , $\hat{\mathbf{q}}_r$ and $\hat{\mathbf{q}}_i$ with the transient solution $\mathbf{q}_n \equiv \mathbf{q}(x, y, t_n)$ known at these times. Simple algebra delivers the desired converged steady-state solution \mathbf{Q}_b as

$$\mathbf{Q}_b = \frac{\mathbf{q}_1 e^{2\sigma\Delta t} - 2 \mathbf{q}_2 e^{\sigma\Delta t} \cos \Omega_r \Delta t + \mathbf{q}_3}{e^{2\sigma\Delta t} - 2 e^{\sigma\Delta t} \cos \Omega_r \Delta t + 1}. \quad (6.15)$$

As an aside, the spatial structure $(\hat{\mathbf{q}}_r, \hat{\mathbf{q}}_i)$ of the linear eigenmode $\hat{\mathbf{q}}$ may also be recovered to within an arbitrary constant from the same linear system. Equivalently, if only the converged steady-state solution is of interest, the expression

$$\mathbf{Q}_b = \frac{1}{\Omega_r^2 + \sigma^2} \left\{ (\Omega_r^2 + \sigma^2) \mathbf{q} - 2\sigma \frac{\partial \mathbf{q}}{\partial t} + \frac{\partial^2 \mathbf{q}}{\partial t^2} \right\} \quad (6.16)$$

may be used for the recovery of \mathbf{Q}_b from transient data for \mathbf{q} and its first two time-derivatives. Either of (6.15) or (6.16) may be used for the cases of residuals corresponding to stationary ($\Omega_r = 0$) or travelling ($\Omega_r \neq 0$) single linear eigenmodes.

This idea may be extended to extract \mathbf{Q}_b from a DNS signal comprising several linearly

decaying eigenmodes superimposed upon the steady-state solution,

$$\mathbf{q} = \mathbf{Q}_b + \sum_n \varepsilon_n (q_{n,r} \cos \Omega_{n,r} t - q_{n,i} \sin \Omega_{n,r} t) e^{\sigma_n t}. \quad (6.17)$$

As an example, in the case of one stationary

$$\varepsilon_1 \mathbf{q}_{1,r} e^{\sigma_1 t} \quad (6.18)$$

and one travelling

$$\varepsilon_2 (\mathbf{q}_{2,r} \cos \Omega_r t - \mathbf{q}_{2,i} \sin \Omega_r t) e^{\sigma_2 t} \quad (6.19)$$

linear disturbance being present in the signal, one may first extract information for the damping rate of the stationary mode from the signal itself and for the damping rate and frequency of the travelling disturbance from the first time-derivative of the DNS signal for \mathbf{q} . Subsequently, one may solve the $(2NxNy) \times (2NxNy)$ system defined by writing

$$(\sigma_2^2 + \Omega_r^2) \mathbf{Q}_b + (\sigma_1^2 + \sigma_2^2 + \Omega_r^2 - 2\sigma_1\sigma_2) \varepsilon_1 \mathbf{q}_{1,r} e^{\sigma_1 t} = \frac{\partial^2 \mathbf{q}}{\partial t^2} - 2\sigma_2 \frac{\partial \mathbf{q}}{\partial t} + (\sigma_2^2 + \Omega_r^2) \mathbf{q} \quad (6.20)$$

at two consecutive times t_1 and t_2 for \mathbf{Q}_b and $\varepsilon_1 \mathbf{q}_{1,r}$, where Nx and Ny are the number of points discretising the x - and y -spatial directions, respectively.

The accuracy by which Ω_r and σ are determined depends on that by which the first three time-derivatives of \mathbf{q} are calculated; this, in turn, depends on the time-step in the calculation and the number of fields stored in order for backward differentiation formulae to be applied. Since the time-step is controlled by CFL considerations, it is advisable to store a reasonably high number of fields in order for high accuracy of Ω_r and σ and, in turn, of \mathbf{Q}_b to be obtained. The calculations to be presented in what follows have been performed using five-point backward differencing formulae on an equidistant grid (Abramowitz and Stegun 1956).

At conditions at which a steady-state solution exists most two-dimensional global eigenmodes of the converged steady-state are heavily damped ($\sigma_n = O(1)$ in equation (6.17)). Consequently, if the time-integration of the equations of motion is pursued long enough, only a handful of ($\lambda = 0$)-global eigenmodes will survive and persist in the DNS signal. Clearly, it is the least damped of the global instabilities that will determine the ultimate behaviour of the solution. In determining whether one integrates the equations of motion until all but the least-damped of the eigenmodes have subsided in order to apply (6.15) or (6.16) or one recovers \mathbf{Q}_b at an earlier time from a signal in which a number of damped eigenmodes still persist one should take into account the following factors.

First, the efficiency of the specific DNS algorithm determines whether the cost of integrating the equations of motion until convergence is acceptable at given flow parameters. The cost of computing Ω_r , σ , intermediate values of \mathbf{Q}_b and monitoring convergence of all these quantities, possibly for several eigenmodes, must also be weighed against the straightforward approach of pursuing the time-integration in the DNS until convergence. However, at all Reynolds numbers studied in the prototype flow monitored both σ and Ω_r of individual modes have converged within the first quarter to half of the total integration time, making further time-integration superfluous. While the integration time until convergence is short at low Reynolds numbers, on account of large damping rates of the least-damped linear eigenmodes, at increasingly large Reynolds numbers the magnitude of the damping rates becomes increasingly smaller and application of the ideas exposed in this section becomes increasingly attractive in order for substantial savings in computing effort to be materialised.

(c) *Results for the square lid-driven cavity*

An example flow in which these ideas may be illustrated is the classic lid-driven cavity (Burggraf 1966). In its function as a testbed for numerous algorithms this flow has generated a substantial amount of information which is relevant to the preceding discussion. Calculations for Q_b were performed using a two-dimensional spectrally-accurate algorithm for direct numerical simulation of flow in nonperiodic geometries. The code is based on a real-space eigenvalue-decomposition of the spectral collocation differentiation matrices extending ideas discussed by Ku *et al.* (1988) and uses one member of the low-storage second-order accurate time-integration schemes put forward by Spalart *et al.* (1991). A spectral algorithm was chosen in order for optimal accuracy to be obtained on a low number of collocation points, the latter being dictated by the maximum number of points on which numerical solution of the partial-derivative eigenvalue problem is feasible using current computer technology. Solutions were obtained using Jacobi polynomials for the spatial discretisation at resolutions depending on the Reynolds number and ranging from 32^2 to 128^2 spectral collocation points. The time-steps at the different Reynolds numbers were kept well below those dictated by the CFL condition in order for reasonable accuracy of the results of σ to be ensured. In view of our arguments being based on nonparallel linear instability analysis and the well-known sensitivity of linear instability analysis results on the accuracy of the basic flow, we first present a validation of both the basic flow and the partial derivative eigenvalue problem.

(i) VALIDATION STUDIES

The accuracy of the converged steady-state solutions is first assessed by comparison with the established works of Ghia *et al.* (1982) and Schreiber and Keller (1983). Converged basic states have been calculated at several Reynolds numbers of which we present calculations at $Re = 400, 1000, 3200$ and 4000 , the first three obtained on 32^2 and the last on 48^2 Legendre collocation points. At $Re = 400$ and 1000 both aforementioned works present results while at the higher Reynolds numbers we compare our calculations individually with either work. Interestingly, aside from the locations and maximum values of streamfunction and vorticity in the primary vortex core, Schreiber and Keller (1983) analysed and presented their results in the form of a converging series calculated by Richardson extrapolation. Comparisons are presented in a twofold manner. The comparison of our calculations for the location and maxima in the stream-function $\bar{\psi}$ and the vorticity $\bar{\zeta}$ with those of the reference works is shown in Table 3; note that Schreiber and Keller (1983) define ζ to have an opposite sign to that of Ghia *et al.* (1982) and the present work. Although the overall agreement of all results is quite reasonable marginal differences exist. These may be attributed to the different grids used in all three works, making an interpolation procedure necessary for detailed comparisons. To this end, we employed a piecewise cubic procedure to transfer our results onto the (different) maxima of the benchmark calculations. Our interpolated values as well as the results of Ghia *et al.* (1982) and Schreiber and Keller (1983) are presented in Table 4b, where the individual comparisons demonstrate a substantially more satisfactory agreement of our calculations with both benchmark works at low Re -values and especially with the Richardson extrapolated results of Schreiber and Keller (1983) at the highest Reynolds number monitored.

It is well-known from comparisons of three-dimensional DNS results and one-dimensional Orr-Sommerfeld-based linear instability analysis that details of the steady basic state strongly influence the accuracy of the growth/damping rates of linear eigenmodes (Kleiser and Schumann 1980). The remaining differences between our results for the two-dimensional steady-states in the lid-driven cavity and those of the benchmark works are next assessed in this light, from the point of view of their influence on the global linear instability analysis results. Two solutions of the partial derivative eigenvalue problem (6.6-6.9) for the lid-driven cavity exist, those of Ramanan and Homsy (1994) (RH) and Ding and Kawahara (1998) (DK). These authors have

presented linear instability analyses of the square lid-driven cavity flow which deliver consistent results at low Re but predict different critical Reynolds number values for linear amplification of three-dimensional perturbations. While individual comparisons are certainly possible, at high Reynolds numbers neither work presents results for the two-dimensional global linear instabilities which are central to the theme of the present paper. We therefore refrain here from discussion of three-dimensional linear instability and the issue of a linear critical Reynolds number and monitor a low value of the Reynolds number, $Re = 200$, at which both RH and DK present results at $\lambda = 0$.

Table 5 shows the tabulated values of RH, the graphically reproduced results of DK and our solutions of the partial-derivative eigenvalue problem (6.6-6.9). The overall agreement of the previous and the present instability analyses is quite good and all results indicate the experimentally established fact of stability of the two-dimensional flow in the lid-driven cavity at this Reynolds number (Burggraf 1966). Regarding the quality of the basic flow, it may be inferred from the results of Table 5 that the basic states of both RH and DK and the present work are practically identical for the purposes of the linear instability analysis that follows, at least at the Reynolds numbers discussed.

(ii) NUMERICAL RESIDUALS AND ($\lambda = 0$) LINEAR EIGENMODES IN THE SQUARE LID-DRIVEN CAVITY

Figs. 26-30 show the convergence histories of the two-dimensional DNS at several Reynolds numbers, with the qualitative behaviour of residuals discussed earlier observed. The convergence of the rate of decay of residuals σ , calculated using (6.3-6.4), is shown in Table 6 at $Re = 100, 200$ and 300. Also shown is the damping rate Ω_i of the least-damped eigenmode having $\lambda = 0$ as obtained by linear analysis, based on the partial-derivative eigenvalue problem (6.6-6.9), of the converged steady-state \mathbf{Q}_b corresponding to each Reynolds number. The excellent agreement between the two quantities leaves little room for doubt that numerical residuals may be identified as being the least-damped ($\lambda = 0$)—eigenmode of the corresponding converged steady-state. It is interesting to note here that such an agreement could *not* be obtained when we followed the commonly-used procedure to terminate the steady-state calculation after a decay of residuals by an arbitrarily defined seemingly adequate small number of orders of magnitude, say 5-6. Such poorly converged in time basic states may be viewed as comprising a small unsteady component the linear instability analysis of which is bound to deliver erroneous results. Further, it is worth mentioning that the prediction (6.10) of the time necessary to integrate the equations of motion until convergence in time is in line with the results of Table 6 and Fig. 26.

A clearly defined single value of σ which determines the behaviour of residuals in the entire course of the time-integration is a result of a two-dimensional eigenspectrum of \mathbf{Q}_b in which the least damped two-dimensional ($\lambda = 0$)—eigenmodes are stationary and well separated in parameter space from their more stable counterparts. The situation becomes more intricate, but still amenable to analysis, as the Reynolds number increases. Qualitative differences may be found between the results of Figs. 26 and 27, although all simulations were started from the same initial condition $\psi = \zeta = 0$. While in both sets of results a short initial transient is followed by exponential decay of residuals, in the first set this decay pursues at the same rate for almost two decades while in the second two different rates of exponential decay of residuals are demonstrated. Inspection of the full spectra delivered by numerical solution of (6.6-6.9) at each Reynolds number reveals that as the Reynolds number increases an increasingly larger number of eigenmodes, both stationary and travelling appear in the eigenspectrum of \mathbf{Q}_b , having damping rates approximately equal with that of the least damped eigenmode. As a consequence, the numerical solution may initially be attracted to a different than the least damped ($\lambda = 0$)—eigenmode but its long-time behaviour will be determined by the latter disturbance. In both

the $Re = 500$ and the $Re = 1000$ results of Fig. 27 the damping rates Ω_i of the least and the next more stable mode are presented as symbols superimposed upon the curves used to determine σ .

Yet another qualitatively different behaviour is observed in the time-signal of \mathbf{q} as a consequence of a further increase of the Reynolds number. Alongside the least damped stationary mode travelling disturbances appear, as seen in the results of Figs. 28-30. In all three figures $\sigma(t)$ assumes the form of exponentially decaying disturbances. However, while at the lowest Reynolds number a clearly identifiable sinusoidal perturbation may be seen, having $\Omega_r \approx 0.97 \pm 0.01$, a barely perceptible deviation from a single oscillatory disturbance ($\Omega_r \approx 0.954 \pm 0.012$) may be seen at $Re = 5000$; at $Re = 7500$ the solution demonstrates a behaviour which might be interpreted either as nonlinearity or as superposition of two exponentially decaying linear sinusoidal disturbances having frequencies of $\Omega_r = 0.933$ and 0.945 . In order to analyse these observations we pursue two independent paths. First, we perform a nonparallel linear instability analysis of the converged steady state at each Reynolds number and monitor the least-stable member of the eigenspectrum, which turns out to be a stationary linear eigenmode. Second, we perform a discrete Fourier transform (DFT) of the DNS signal for \mathbf{q} at $Re = 2500, 5000$ and 7500 and compare the results with the eigenvalues of the travelling disturbances delivered by the linear instability analysis.

Table 7 shows that a progressive deviation of the rate of decay of the residuals from the damping rate of the least-damped eigenmode occurs as Re increases. This result suggests that as the Reynolds number increases nonlinear interaction of the least stable eigenmodes may cause a departure of the numerical solution from a behaviour predicted by nonparallel linear theory. The role that the least stable members of the full eigenvalue spectrum play in the dynamics of the flow may be inferred from the results of Figs. 31- 33. In Fig. 31 we present the DFT of the DNS signal for $\psi(0.5, 0.5)$ scaled by the maximum value of the spectral density. A single peak at $2\pi f \approx 1$, albeit of somewhat wide support, dominates over two much smaller peaks at $2\pi f = 0$ and $2\pi f \approx 2$. Shown are also the results of (6.6-6.9) for Ω_r , arbitrarily placed on the vertical axis for readability. An one-to-one correspondence between the peaks in the spectrum and the values of Ω_r for stationary and travelling linear eigenmodes is clearly identifiable. Interestingly, the width of the support of the peaks is found to be associated with the existence of more than one eigenvalues in the partial-derivative eigenvalue problem spectrum, at both $\Omega_r \approx 1$ and $\Omega_r \approx 2$. The origin of the existence of only harmonics of the first travelling eigenmode in the full eigenvalue spectrum deserves further investigation. It should be noted here that a Krylov subspace iteration method has been used for the solution of the partial-derivative eigenvalue problem, which results in only a window of the eigenvalue spectrum being captured at any single calculation. The number of converged eigenvalues recovered increases as the subspace dimension increases. However, the neighbourhood of $(\Omega_r, \Omega_i) = 0$ has been well resolved in all results presented here. A higher Krylov subspace dimension has been found to deliver additional eigenvalues at higher frequencies.

While the agreement between the frequencies in the DNS signal and those of the nonparallel linear analysis of the converged steady state is evident, the results of Fig. 31 do not provide any information on the damping rates Ω_i of the disturbances whose frequency lies at $\Omega_r \approx 1$ in relation to those at different frequencies. For our argument that the residuals in the calculation may be identified as the least stable of the two-dimensional ($\lambda = 0$)–eigenmodes to be valid, the damping rate of the linear disturbances at $\Omega_r \approx 1$ must be lower than that of modes with higher frequencies; this is a point to which we will return shortly. Qualitatively analogous results are obtained at $Re = 5000$, seen in Fig. 32. Besides the slight shift towards lower frequencies, the quantitative difference with the results at $Re = 2500$ is that the strength of the eigenmodes at $\Omega_r \approx 2$ is substantially larger than that of their counterparts at $Re = 2500$ in relation to the strength of the respective modes at $\Omega_r \approx 1$; this is the origin of the slight deviation from a purely sinusoidal behaviour of the signal at this Reynolds number, seen in Fig. 29. Further, additional

eigenmodes appear alongside the counterparts of those seen at $Re = 2500$ at $\Omega_r = 0$ and $\Omega_r \approx 1$ and new modes appear at $\Omega_r \approx 3$ and $\Omega_r \approx 4$. Finally, at $Re = 7500$, the pattern discovered at the lower Reynolds number values qualitatively repeats itself, with the appearance of additional modes at the same and new at high-frequencies; furthermore a new mode which does not fit in the period-doubling scenario discussed also is present in the linear instability analysis results, which the DFT reveals to be too weak to play an important role in the dynamics of the flow at this Reynolds number value.

We return to the question of damping rates of the linear instability modes and present in Fig. 34 the full spectrum of eigenvalues in the neighbourhood of $\Omega = 0$ at $Re = 2500, 5000$, and 7500 . Results of significance in this figure are the following. First, as the Reynolds number increases the flow becomes less stable to two-dimensional linear ($\lambda = 0$)–eigenmodes. Second, in all three Reynolds numbers the least stable modes are stationary disturbances. Third, perfect symmetry about $\Omega_r = 0$ may be observed in the results, as should be expected from the ability to reformulate (6.6-6.9) as a real eigenvalue problem. Consistent with the DFT results of the signal discussed earlier, the eigenmodes at $\Omega_r \approx 1$ are less stable than their counterparts at higher frequencies. Comparing, for example, the $Re = 5000$ eigenmodes $(\Omega_r, \Omega_i) = (0.967, -0.0158)$ and $(\Omega_r, \Omega_i) = (1.921, -0.0319)$ one finds that, if introduced at the same initial amplitude in the flow, the second mode would be reduced by a given number of orders of magnitude in amplitude in approximately half as long an integration time as that required for the first mode to experience the same reduction of amplitude.

(iii) THE CRITICAL REYNOLDS NUMBER OF ($\lambda = 0$)–LINEAR DISTURBANCES

The preceding discussion leads to re-examination of the question of a critical Reynolds number for linear growth of two-dimensional global instabilities in the square lid-driven cavity. Consistent with well-established numerical solutions for the steady-state in this flow the nonparallel linear instability analysis results of § 6 (c) ii deliver a least damped stationary ($\lambda = 0$)–eigenmode which has a damping rate whose magnitude decreases with increasing Reynolds number. The dependence of Ω_i on Re for this mode has been obtained at several Reynolds numbers and is presented by symbols in Fig. 35. Analysis of the results for the damping rate of the least-damped eigenmode as function of the Reynolds number delivers a curve-fit of the data by using

$$\Omega_i = -109.071 Re^{-1.068}. \quad (6.21)$$

The curve defined by (6.21) is also shown in Fig. 35 by a solid line and has been found to deliver reasonably accurate predictions of Ω_i at $Re > 1000$, where the calculated data may be collapsed onto a single curve. The upper bound of the Reynolds-number range in which (6.21) may be used with confidence to predict the rate of decay of residuals and the associated time of integration of the equations of motion until a steady-state solution is reached must be $Re \approx 10^4$, a value below which a multitude of two-dimensional numerical solutions have demonstrated the existence of converged two-dimensional states. In the framework of the current nonparallel linear instability analysis this should manifest itself by \mathbf{Q}_b losing its stability in a linear framework to amplified two-dimensional perturbations having $\lambda = 0$. However, as has been mentioned, the existence of a converged steady-state solution is synonymous with all global eigenmodes of the flow being stable. Another possibility is that the nonlinear interaction of two-dimensional global neutrally-stable disturbances as the Reynolds number increases may be held responsible for the observed inability to obtain a converged steady state solution. However, from (6.21) it follows that $\Omega_i < 0$, $\forall Re$ and the flow remains stable to all two-dimensional ($\lambda = 0$)–eigenmodes. Two aspects of this prediction should be stressed here. First, (6.21) is a curve-fit, at best valid up to the highest Reynolds number used to produce it, $Re = 7500$. Second, the filling-up of the eigenspectrum and the associated nonlinear interaction of some of the least stable eigenmodes as the Reynolds number increases, causes a systematic departure of the numerical solution for \mathbf{q}

from one determined by a single eigenmode of the nonparallel linear instability theory, as already shown in the results of Table 7. On the other hand, the trend predicted by (6.21) is correct, namely that the damping rates of two-dimensional global linear instabilities as Re increases are exponentially small in magnitude. As such, an increasingly large number of global modes may be considered neutrally stable at large Reynolds numbers; it is therefore likely that the second scenario, namely nonlinear interaction of near neutrally stable two-dimensional global flow eigenmodes is responsible for the observed loss of ability to obtain a steady-state solution of the equations of motion at $Re > 10^4$ (f.e. E and Liu 1996).

(iv) OBTAINING THE CONVERGED STEADY-STATE SOLUTION FROM NON-CONVERGED TRANSIENT DATA

The preceding discussion has demonstrated the association of residuals in two-dimensional incompressible DNS calculations with the two-dimensional global linear instability modes of the converged steady state. In this section we present examples of recovery of steady-state solutions from transient DNS data using this information and the algorithm of § 6 (b) v. We stress that the applicability of the algorithm is intimately linked with the quality of the DNS and the initial conditions used for the simulation, since both determine when, for what length of time and to which linear eigenmode the time-accurate solution will be attracted in the course of the time-integration. Here we present a discussion of some parameters which affect the results returned by the algorithm in a few Reynolds number cases of those on which the algorithm was validated.

Results at $Re = 100$ and 1000 are shown in Table 8; at each Reynolds number we have performed three sets of calculations, two direct numerical simulations and one solution of the partial-derivative eigenvalue problem. Both DNS start from the initial condition $\psi = \zeta = 0$ for the flow streamfunction and vorticity, respectively. On the one hand, the converged 'exact' steady state \mathbf{Q}_b has been calculated by marching the equations of motion until such a time \bar{t} that the residuals were reduced to machine-roundoff level, using 64-bit arithmetic and monitoring convergence along the lines discussed in § 6 (c) i. On the other hand, we have run another DNS but marched the equations of motion until such a time \tilde{t} was reached at which a linear regime was identified by the convergence in time of Ω_r (when applicable) and σ . The time-marching was then interrupted and either (6.15) or (6.16) was solved for the respective 'estimated' steady-state solution $\tilde{\mathbf{q}}$. Finally, the partial-derivative eigenvalue problem (6.6-6.9) was solved for two-dimensional disturbances ($\lambda = 0$) developing upon \mathbf{Q}_b and the eigenvalue spectrum pertaining to the flow at each Reynolds number was recovered. The results were compared both in terms of the magnitude of the relative discrepancy of the two DNS-obtained solutions $\Delta \mathbf{q} \equiv |(\tilde{\mathbf{q}} - \mathbf{Q}_b)/\mathbf{Q}_b|$ and by monitoring the difference between σ in the second set of DNS and Ω_i . Table 8 shows the resolutions and time-steps used in several simulations, the time \bar{t} at which a converged steady-state solution $(\bar{\psi}, \bar{\zeta})$ was obtained by DNS and the time \tilde{t} at which the damping rate of residuals converged to within a predefined tolerance of relative discrepancy 10^{-6} between successive values of σ and the results for $\tilde{\psi}$ were calculated. The value of σ as well as the relative discrepancy $\Delta \tilde{\psi} \equiv |(\tilde{\psi}(\tilde{t}) - \bar{\psi})/\bar{\psi}|$ between the estimated and the exact steady-states is also shown; the level at which the eigenmode being damped is present in the transient solution at time \tilde{t} may be inferred from $\Delta \psi$.

The most significant result of this table is the ratio \tilde{t}/\bar{t} . The case $Re = 100$ is typical of one in which the least-stable eigenmode determines the transient behaviour of the DNS throughout most of the time-integration process. With the results for σ converging quite quickly, the desired converged steady-state may be obtained at a time between a quarter at the coarsest and a fifth at the finest resolution of the time required by the time-marching algorithm for the residuals to be eliminated. The result for σ is only marginally affected by resolution and time-step; the precise times at which σ converges are affected by a small amount when refining the grid, with the finest resolution results converging earlier. In all cases use of the algorithm of § 6 (b) v

results in substantial savings compared with the otherwise necessary computing effort. The spatial distribution of the difference $\Delta\tilde{\psi}$, obtained using 48 collocation points to discretise each spatial direction, is shown in Fig. 36; aside from the level of $\Delta\tilde{\psi}$ it is interesting to notice that the discrepancy between the two solutions attains its maximum values in the centre of the cavity and neither the singularity of the boundary conditions nor the corner vortices are manifested in this quantity. The same qualitative behaviour was shown by all distributions of $\Delta\tilde{\psi}$ at lower resolutions. An estimate of the converged solution $\tilde{\psi}$ obtained by application of (6.15) at $\tilde{t} = 15$ may be found in Fig. 37, drawn as contours at the levels presented by Ghia *et al.* (1982). No cosmetic post-processing of the results has been applied, with values presented at the collocation points used. As it is to be expected by the results of Table 8 the agreement between $\tilde{\psi}$ and the result of Ghia *et al.* (1982) is remarkable.

At $Re = 1000$, σ converges at approximately the same fraction of total integration time as in the $Re = 100$ results. However, compared with the $Re = 100$ case where the discrepancy between estimated and converged steady-states is three to four orders of magnitude smaller compared with that shown by $\Delta\psi$, here only one order of magnitude difference between the maxima of $\Delta\tilde{\psi}$ and $\Delta\psi$ is shown. Though small, the discrepancy between $\tilde{\psi}$ and $\bar{\psi}$ is much larger than roundoff level, implying that elimination of the least stable eigenmode from the time-dependent signal for ψ at $Re = 1000$ does not suffice to deliver the desired $\bar{\psi}$. Another observation that may be made by comparing the results of the $Re = 100$ and $Re = 1000$ cases is that at approximately the same value of $\tilde{t}/\bar{t} \approx 0.23$, $\Delta\tilde{\psi}$ is higher by about an order of magnitude at $Re = 1000$ compared with that at $Re = 100$. In searching for an explanation of this behaviour, three factors may be recalled. First, convergence of σ between successive values is a necessary but not sufficient condition for the algorithm of § 6 (b) v to deliver accurate results; the converged σ should be compared with the corresponding damping rates Ω_i in the least-stable part of the eigenspectrum of the converged steady-state \mathbf{Q}_b . Second, as the Reynolds number increases the damping rates of all global eigenmodes decrease, suggesting that increasingly longer integration times are necessary in the case of a higher Reynolds number in order for the residuals to subside to the same level as in a lower Reynolds number case. Third, the separation of the eigenvalues in the global spectrum plays a significant role in attracting the transient solution. A distinction must be made between the early and the late stages of the transient behaviour of the DNS solution. In the latter it is the least-damped eigenmode which must eventually be damped in order for a steady-state to be obtained. During the early stages of the simulation, on the other hand, an arbitrary initial condition may need a large number of damped global eigenmodes in order to be reconstructed. It is, therefore, conceivable that at the early stages of the simulation a number of eigenmodes other than the least-damped one are present in the transient solution. However, as time progresses, increasingly more of these additional eigenmodes subside on account of their large damping rates, to the effect that only the least-damped mode remains to determine the behaviour of the residual. In other words, as time progresses, equation (6.17) reduces to (6.11) and the theory of § 6 (b) v focussing on a single damped eigenmode is applicable.

This conjecture may easily be put to test by simply permitting the time integration in the second DNS to proceed beyond \tilde{t} while monitoring on the one hand σ against Ω_i and on the other hand $\Delta\tilde{\psi}$ in the process; the results may be found in Table 9. At both the lower and the higher Reynolds number further integration of the equations of motion in time results in all but the least-stable eigenmode being eliminated from the signal, as clearly demonstrated by the progressive agreement between the damping rate of residuals σ and the damping rate Ω_i of the least stable ($\lambda = 0$)-global flow eigenmode. Consistent with this result is the increasingly improved accuracy by which the algorithm of § 6 (b) v returns the estimate of the converged steady state, as shown by the minimum and maximum values of $\Delta\psi$ also cited. Interestingly, $\bar{\psi}$ may be recovered at the same low level of discrepancy in the two Reynolds number cases, f.e.

$O(10^{-8})$ at $Re = 100, \tilde{t}/\bar{t} = .25$ and $Re = 1000, \tilde{t}/\bar{t} = .35$, although the agreement of σ with Ω_i in the $Re = 100$ is about an order of magnitude better than that in the $Re = 1000$ case.

(v) THREE-DIMENSIONALITY AS A CONSEQUENCE OF AMPLIFIED ($\lambda \neq 0$) TWO-DIMENSIONAL LINEAR EIGENMODES

Finally, we turn our attention to the differences between two- and three-dimensional simulations on account of growing global linear instability modes. While the physics behind the instability mechanisms is universal, the lid-driven cavity flow example serves again as a demonstrator, with the differences between two- and three-dimensional numerical simulation results in this flow being well established (Ku *et al.* 1987). Here we call upon the global linear instability theory to discuss their straightforward explanation.

It is possible that while the ($\lambda = 0$)-eigenmodes at a certain Reynolds number are damped there exist unstable $\lambda \neq 0$ global flow eigenmodes. Indeed, Ding and Kawahara (1998) have shown that at $Re = 950$ the flow is unstable to modes having $\lambda \in [\lambda_l, \lambda_h]$ with $\lambda_l = 2\pi/L_h \approx 6.6$ and $\lambda_h = 2\pi/L_l \approx 8.3$, while the domain of unstable wavenumbers systematically broadens in both directions on the λ -axis as the Reynolds number increases. There exist two possibilities of introduction of three-dimensionality by means of DNS, either by considering spanwise periodicity (pDNS) or by taking an aperiodic spanwise domain bounded by solid walls (aDNS). In the case of pDNS the integration domain in the spanwise direction is defined through discrete integer multiples of a fundamental wavenumber λ_0 such that $L_z = 2\pi/(n\lambda_0), n = 1, 2, \dots$, while in aDNS L_z is a continuous free parameter. We discuss the two possibilities separately; in both cases we restrict the discussion to simulations performed under initial and boundary conditions such that linear instability mechanisms alone can drive nonlinearity.

If a three-dimensional pDNS is performed at $Re = 950$ and a spanwise length of the integration domain L_z is chosen such that $\lambda_0 > 8.3$, that is $L_z < 0.76$, neither λ_0 nor any of the harmonics of this global linear eigenmode can be amplified. As a consequence one may predict, without performing the three-dimensional simulation, that the latter will converge in time to the same steady-state solution to which a two-dimensional ($\partial/\partial z \equiv 0$) simulation converges. At the same Reynolds number value, a choice of spanwise wavelength $L_z \in [L_l, L_h] = [0.76, 0.95]$ will result in exponential amplification and, eventually, turbulent flow on account of the unstable fundamental wavenumber which is implicitly defined by a spanwise wavelength within this range. Finally, if $L_z > 0.95$ two distinct situations may be obtained; with the fundamental wavenumber being stable ($\lambda_0 < 6.6$), L_z may be taken such that none of its harmonics fit within the domain of unstable wavenumbers at this Reynolds number, or an L_z may be chosen such that some harmonic may be amplified. While in the first case the two-dimensional steady-state solution will be obtained, the result of a three-dimensional simulation in the second case will be transition to a turbulent flow state. The case of an aDNS may be perceived as a special case of a pDNS, since the homogeneous Dirichlet conditions imposed on the disturbance quantities are a subset of those admissible in a periodic simulation. Here there exist two possibilities, depending on whether L_z is smaller or larger than L_l . In the first case two- and three-dimensional simulations will deliver identical converged steady-state solutions while in the second, which includes the well-studied case of a cubic cavity, transition to turbulence should be expected on account of at least one three-dimensional ($\lambda \neq 0$) eigenmode having a wavenumber which fits into $\lambda \in [6.6, 8.3]$ at this Reynolds number value. At higher Reynolds number values the situation is qualitatively analogous for aDNS, with the dichotomy in wavenumbers being determined by the highest neutrally stable wavenumber value. For pDNS, on the other hand, the analogous discussion to that at $Re = 950$ applies at $L_z < L_l$ and $L_z \in [L_l, L_h]$. There exists a Reynolds number value, though, at which $\lambda_h \geq 2\lambda_l$; in such a situation, if $L_z > L_h$ there will always be some harmonic of λ_0 which will correspond to an unstable mode having $\lambda = n\lambda_0 \in [\lambda_l, \lambda_h]$ which will be liable to linear amplification in the three-dimensional simulation and eventual departure of the three-

from the two-dimensional numerical simulation results. The lid-driven cavity with its large body of numerical results is but one example of demonstration of this behaviour; we are currently applying these ideas in the compressible elliptic cone flowfield.

(d) *Summary and Epilogue*

The questions raised in § 6 (a) may be answered within the unifying framework of global linear instability analysis of a two-dimensional steady solution of the equations of motion. Aided by the results of a numerically well-studied incompressible flow problem we were able to attach physical significance to the transient behaviour of two-dimensional time-dependent incompressible direct numerical simulation results. What is commonly known as residual in the simulation is either the least damped two-dimensional ($\lambda = 0$)–linear eigenmode of the converged steady state itself, or can be related to a small number of the least damped modes of the full eigenvalue spectrum. As the Reynolds number increases, all global two-dimensional eigenmodes become increasingly less damped, until a parameter value is reached beyond which no steady-state solution exists. The physical information which is suppressed in two-dimensional simulations based on the steady formulation of the equations of motion concerns the dynamical behaviour of these two-dimensional linear eigenmodes. While unsteadiness should not be interpreted as amplification of the global linear ($\lambda = 0$)–eigenmodes, on the simple grounds of the absence of a converged steady-state upon which the latter would develop, the process leading to unsteadiness is directly linked with the diminishing magnitude of damping rates of the global linear modes as the flow Reynolds number increases, and the associated prevalence of nonlinearity.

When a steady-state solution exists, the insight gained from the association of the transient behaviour in two-dimensional DNS with the results of the nonparallel linear instability analysis of the converged steady-state may be utilised in a threefold manner. First, an algorithm may be constructed, to recover the steady-state solution from transient data taken well before convergence, thus making further time-integration of the equations of motion redundant. The algorithm, whose building elements were presented in § 6 (b) v, is based on identification of the parameters pertaining to the linear eigenmodes which determine the transient behaviour of the solution, namely the damping rate σ and the frequency Ω_r of the least stable eigenmodes. Results shown in § 6 (c) iv on the example problem studied have demonstrated that up to three-quarters of the otherwise necessary computing effort may be saved by application of the theory of § 6 (b) v. Second, the results of a nonparallel linear instability analysis of the converged steady-state can be used as a quality test of the obtained solution, if the latter has been obtained using a time-accurate solution approach. The rate of decay of the residual which ultimately has to be damped in order for a converged steady-state to be obtained should equal the damping rate of the least-stable eigenmode, if both numbers are substantially larger than zero in magnitude. Disagreement of these two quantities indicates that the obtained steady-state still contains an unsteady component which must be eliminated by further time-integration, or by application of the ideas of § 6 (b) v. Third, the time necessary for the reduction of residuals to machine-roundoff level may also be estimated using nonparallel linear instability theory and is inversely proportional to the damping rate of the least damped linear eigenmode. Using the value of the damping rate obtained by extrapolation of data at lower Reynolds numbers one predicts that in the square lid-driven cavity at $Re = 10^4$ a steady-state solution, if one exists, may be obtained after integrating the unsteady equations of motion for time in excess of $t = 4000$ as calculated from (6.10) and non-dimensionalised with the lid-velocity and the cavity length.

Well before the flow tends to lose its stability to two-dimensional linear eigenmodes, three-dimensional ($\lambda \neq 0$)–disturbances may be amplified. Depending on the size of the observation window in the third spatial dimension, this amplification of three-dimensional global disturbances can explain the differences between the results of the two- and three-dimensional DNS. Again, caution is warranted at this point not to confuse amplification of the global, two-

dimensional instabilities discussed here with solutions of the classic ordinary-differential-equation based eigenvalue problem, which are incorporated in those of (6.6-6.9); both mechanisms may provide amplification, as the laminar separation bubble flow example has clearly demonstrated (Theofilis *et al.* 2000). Conversely, nonparallel linear instability theory provides a handle to probe into the physics of the flow in (three-dimensional) physical space using two-dimensional DNS results, before resorting to computationally intensive three-dimensional spatial DNS, at least as far as the response of the flow to small-amplitude excitations is concerned. Solution of the partial-derivative eigenvalue problem not only answers the question whether new physics is to be learnt by performing the three-dimensional DNS at a given set of parameters but also provides information on the physical mechanism which leads flow to deviate from two-dimensionality.

Based on the findings presented we may extend the discussion, in the form of proposed future work, to both one and three nonperiodic spatial directions. Both an one-dimensional and a three-dimensional steady-state solution \mathbf{Q}_b may be recovered by application of the ideas discussed herein for the case of two nonperiodic spatial directions. In the case of an one-dimensional profile \mathbf{Q}_b being sought by time-marching the equations of motion, taking two spatial directions as periodic and resolving the third, the associated linear instability problem to be solved is based on the classic system of the one-dimensional Orr-Sommerfeld and Squire linear instability equations to which (6.6-6.9) reduce if the dependence of the basic flow on one of the two resolved spatial directions, say x , is neglected such that this spatial direction may be taken as homogeneous as far as the disturbance field is concerned. The linear mode associated with the residuals is the least stable member of the spectrum obtained at $\kappa = \lambda = 0$, κ and λ being the wavenumbers along the periodic spatial directions, x and z . It is well appreciated in this case that agreement of the time-accurate simulation results and those of the one-dimensional linear instability problem is a minimum simulation quality criterion (Kleiser and Schumann 1980; Canuto *et al.* 1987). However, given current hardware capabilities, it is likely that an one-dimensional \mathbf{Q}_b will be sought by a direct algorithm, rather than by time-marching the unsteady equations of motion.

An extension of the algorithm presented for the recovery of a two-dimensional \mathbf{Q}_b is also possible in the case of flow developing in three nonperiodic spatial directions. In this case the existence of a steady-state \mathbf{Q}_b is synonymous with stability of all eigenmodes of the flow but current hardware technology makes the solution of the corresponding three-dimensional partial derivative eigenvalue problem impractical. On the other hand the ideas presented in section 6 (b) v may be used in order to recover a three-dimensional steady state once a regime of linear damping of residuals has been identified. This is of immediate interest in the case of the elliptic cone geometry, where recovery of the converged steady laminar three-dimensional steady state by application of the ideas presented in this section is currently being actively pursued.

7. Discussion

This report commences presentation of our efforts towards global linear instability analysis of high-speed flow around elliptic cones. We have presented the framework within which the analysis is envisaged to be performed and it has been argued that a global linear analysis in which all three spatial directions are resolved is most efficiently performed by DNS. Our ultimate concern is with a global linear analysis in which two spatial directions are resolved while the third is taken to be homogeneous. Strictly, no such homogeneous spatial direction exists in the flow over an elliptic cone; however the dependence of the basic flow quantities on the directions normal to the cone surface dominates over that along the cone generators and the global analysis may be performed by resolving the former two and neglecting the third spatial direction when addressing the eigenvalue problem. Instead of making this simplifying assumption when computing the basic flow also, we have expanded the scope of our original intention to perform a two-dimensional solution for the basic flow and have opted for a numerical solution of the full three-dimensional problem. We chose the AUSMDV shock-capturing scheme for the discretisation of the convective fluxes in the equations of motion. The scheme was validated and its satisfactory performance in resolving flow discontinuities was established before it was to the elliptic cone geometry.

Solutions of the steady three-dimensional equations of motion were obtained next. A half-cone model was considered and symmetry was imposed on the solution, implying that all the results obtained herein pertain to angle of bank $\beta = 0$. The elliptic cone was terminated by a planar surface and the object was embedded into three-dimensional space which extended well away from the surface of the elliptic cone object. Terminating the cone with a planar surface resulted, as expected, in large flow separation at the base both in subsonic and supersonic flow. In forthcoming basic flow calculations we intend to investigate a compound object composed of the same elliptic cone and a half prolate spheroid/ellipsoid joined together so as to minimise the curvature jump at base and thus reduce the intensity of separation[†] behind the cone.

Instead of devoting our efforts entirely to the refinement of the solution at a single set of parameters, the approach taken in generating solutions of the equations of motion was the creation of a database of initial conditions at different parameters. This approach is expected to assist subsequent global linear instability studies by providing appropriate attractors for fine-resolution basic flow calculations, as required. In order to ensure laminar flow we have kept a constant low Reynolds number value $Re = 10^3$ and permitted variation of the angle of attack and the flow Mach number. Subsonic flow solutions were obtained at $M = 0.5, \alpha = 10^\circ$ and $M = 0.5, \alpha = 20^\circ$ while the same hybrid grid permitted recovery of supersonic solutions at $M = 2, \alpha = 20^\circ$. At $M = 4, \alpha = 20^\circ$ the sharpness of the gradients developing called for an adaptation of the calculation grid, firstly using the solution gradients to redistribute the available gridpoints in three-dimensional space and subsequently increasing the number of points by some 30% compared with those at the lower Mach number values. The same trend has been observed at preliminary studies at $M > 4$, where even higher resolutions to those used herein are expected to be necessary.

We then turned our attention to the instability analysis of the recovered flowfields. It has been argued that a global three-dimensional linear instability analysis, in which a converged steady three-dimensional basic flow forms the variable coefficients of the partial-differential-equation three-dimensional eigenvalue problem, is uninteresting from a physical point of view in its own right. Instead, we have focussed our attention on the two-dimensional eigenvalue problem and presented the equations governing alternative forms of inviscid global two-dimensional linear analysis. In the limit of $\alpha = 0$ we have derived the extension of the Rayleigh equation governing global inviscid instability of compressible flows. In case the analysis of a flowfield in which $\alpha \neq 0$

[†] itself a source of global instability (Theofilis *et al.* 2000)

is of interest, it has been argued that no numerical advantage exists in considering an inviscid analysis; the global instability studies is then best performed in a viscous framework.

Finally, in view of the intimate connection between global instability analysis and steady-state solutions of the equations of motion, we have devoted substantial efforts in identifying residuals in time-accurate simulations as the least stable global eigenmodes of the converged in time steady-state solution. This knowledge, independently verified on the classic lid-driven cavity, permits utilising global linear theory to construct a theoretically-founded convergence acceleration technique towards a steady-state solution of the equations of fluid flow motion. An algorithm has been presented using which the desired steady state may be recovered by simple algebraic operations on transient data taken well before the time-integration procedure has converged. In the worked example substantial savings in computing effort have been materialised compared with the otherwise necessary time-integration until 'residuals' are reduced to machine roundoff level. Extension of this idea on a three-dimensional basic flow is currently underway using the elliptic cone geometry. Results will be reported in due course.

Appendix A. The two-dimensional inviscid linear operators \mathcal{A}_{2d} and \mathcal{B}_{2d}

$$\mathcal{A}_{2d} = \begin{pmatrix} a_{11} & a_{12} & a_{13} & a_{14} & a_{15} \\ a_{21} & a_{22} & a_{23} & a_{24} & a_{25} \\ a_{31} & a_{32} & a_{33} & a_{34} & a_{35} \\ a_{41} & a_{42} & a_{43} & a_{44} & a_{45} \\ a_{51} & a_{52} & a_{53} & a_{54} & a_{55} \end{pmatrix}, \quad (\text{A } 1)$$

$$\begin{aligned} a_{11} &= \bar{u}D_x + \bar{v}D_y + (\bar{u}_x + \bar{v}_y + i\lambda\bar{w})I \\ a_{12} &= \bar{\rho}D_x + \bar{\rho}_x I \\ a_{13} &= \bar{\rho}D_y + \bar{\rho}_y I \\ a_{14} &= i\lambda\bar{\rho}I \\ a_{15} &= 0 \\ \\ a_{21} &= \bar{u}^2 D_x + \bar{u}\bar{v}D_y + (2\bar{u}\bar{u}_x + \bar{u}_y\bar{v} + \bar{u}\bar{v}_y + i\lambda\bar{u}\bar{w})I \\ a_{22} &= 2\bar{\rho}\bar{u}D_x + \bar{\rho}\bar{v}D_y + (2\bar{\rho}_x\bar{u} + 2\bar{\rho}\bar{u}_x + \bar{\rho}_y\bar{v} + \bar{\rho}\bar{v}_y + i\lambda\bar{\rho}\bar{w})I \\ a_{23} &= \bar{\rho}\bar{u}D_y + (\bar{\rho}_y\bar{u} + \bar{\rho}\bar{u}_y)I \\ a_{24} &= i\lambda\bar{\rho}\bar{u}I \\ a_{25} &= D_x \\ \\ a_{31} &= \bar{u}\bar{v}D_x + \bar{v}^2 D_y + (\bar{u}_x\bar{v} + \bar{u}\bar{v}_x + 2\bar{v}\bar{v}_y + i\lambda\bar{v}\bar{w})I \\ a_{32} &= \bar{\rho}\bar{v}D_x + (\bar{\rho}_x\bar{v} + \bar{\rho}\bar{v}_x)I \\ a_{33} &= \bar{\rho}\bar{u}D_x + 2\bar{\rho}\bar{v}D_y + (\bar{\rho}_x\bar{u} + \bar{\rho}\bar{u}_x + 2\bar{\rho}_y\bar{v} + 2\bar{\rho}\bar{v}_y + i\lambda\bar{\rho}\bar{w})I \\ a_{34} &= i\lambda\bar{\rho}\bar{v}I \\ a_{35} &= D_y \\ \\ a_{41} &= \bar{u}\bar{w}D_x + \bar{v}\bar{w}D_y + (\bar{u}_x\bar{w} + \bar{u}\bar{w}_x + \bar{v}_y\bar{w} + \bar{v}\bar{w}_y + i\lambda\bar{w}^2)I \\ a_{42} &= \bar{\rho}\bar{w}D_x + (\bar{\rho}_x\bar{w} + \bar{\rho}\bar{w}_x)I \\ a_{43} &= \bar{\rho}\bar{w}D_y + (\bar{\rho}_y\bar{w} + \bar{\rho}\bar{w}_y)I \\ a_{44} &= \bar{\rho}\bar{u}D_x + \bar{\rho}\bar{v}D_y + (\bar{\rho}_x\bar{u} + \bar{\rho}\bar{u}_x + \bar{\rho}_y\bar{v} + \bar{\rho}\bar{v}_y + 2i\lambda\bar{\rho}\bar{w})I \\ a_{45} &= i\lambda \\ \\ a_{51} &= 0 \\ a_{52} &= (\gamma\bar{p}D_x + \bar{p}_x)I \\ a_{53} &= (\gamma\bar{p}D_y + \bar{p}_y)I \\ a_{54} &= i\lambda\gamma\bar{p}I \\ a_{55} &= \bar{u}D_x + \bar{v}D_y + (\gamma\bar{u}_x + \gamma\bar{v}_y + i\lambda\bar{w})I \end{aligned}$$

and

$$\mathcal{B}_{2d} = \mathbf{i} \begin{pmatrix} b_{11} & b_{12} & b_{13} & b_{14} & b_{15} \\ b_{21} & b_{22} & b_{23} & b_{24} & b_{25} \\ b_{31} & b_{32} & b_{33} & b_{34} & b_{35} \\ b_{41} & b_{42} & b_{43} & b_{44} & b_{45} \\ b_{51} & b_{52} & b_{53} & b_{54} & b_{55} \end{pmatrix}, \quad (\text{A } 2)$$

$$\begin{aligned} b_{11} &= I \\ b_{12} &= 0 \\ b_{13} &= 0 \\ b_{14} &= 0 \\ b_{15} &= 0 \end{aligned}$$

$$\begin{aligned} b_{21} &= \bar{u}I \\ b_{22} &= \bar{\rho}I \\ b_{23} &= 0 \\ b_{24} &= 0 \\ b_{25} &= 0 \end{aligned}$$

$$\begin{aligned} b_{31} &= \bar{v}I \\ b_{32} &= 0 \\ b_{33} &= \bar{\rho}I \\ b_{34} &= 0 \\ b_{35} &= 0 \end{aligned}$$

$$\begin{aligned} b_{41} &= \bar{w}I \\ b_{42} &= 0 \\ b_{43} &= 0 \\ b_{44} &= \bar{\rho}I \\ b_{45} &= 0 \end{aligned}$$

$$\begin{aligned} b_{51} &= 0 \\ b_{52} &= 0 \\ b_{53} &= 0 \\ b_{54} &= 0 \\ b_{55} &= I \end{aligned}$$

References

- M. Abramowitz and I. Stegun 1970
Handbook of mathematical functions.
Dover.
- C. K. Aidun, and N. G. Triantafillopoulos and J. D. Benson 1991
Global stability of a lid-driven cavity with throughflow: Flow visualization studies.
Phys. Fluids A **3**, 2081–2091.
- J. D. Benson and C. K. Aidun 1992
Transition to unsteady nonperiodic state in a through-flow lid-driven cavity.
Phys. Fluids A **4**, 2316–2319.
- T. J. Bridges and P. J. Morris 1984
Differential eigenvalue problems in which the parameter appears nonlinearly.
J. Comp. Phys. **55**, 437.
- W. R. Briley 1971
A numerical study of laminar separation bubbles using the Navier-Stokes equations.
J. Fluid Mech. **47**, 713–736.
- O. R. Burggraf 1966
Analytical and numerical studies of the structure of steady separated flows.
J. Fluid Mech. **24**, 113–151.
- C. Canuto, M. Y. Hussaini, A. Quarteroni, and T. A. Zang 1987
Spectral methods in fluid dynamics. Springer.
- P. G. Drazin and W. H. Reid (1981)
Hydrodynamic Stability.
Cambridge University Press.
- G. Dietz and S. Hein 1999
Entropy-layer instabilities over a blunted flat plate in supersonic flow.
Phys. Fluids **11** (1), 7–9.
- Y. Ding and M. Kawahara 1998
Linear stability of incompressible flow using a mixed finite element method.
J. Comp. Phys. **139**, 243–273.
- P. W. Duck 1990
The inviscid axisymmetric stability of the supersonic flow along a circular cylinder.
J. Fluid Mech., **214**, 611–637.
- W. E and J.-G. Liu 1996
Vorticity boundary condition and related issues for finite-difference schemes. *J. Comp. Phys.* **124**, 368–382.
- G. Erlebacher and M. Y. Hussaini 1990
Numerical experiments in supersonic boundary layer stability.
Phys. Fluids A, **2**, 94–104.
- D. Gaitonde and M. Visbal 1999
Further development of a Navier-Stokes solution procedure based on higher-order formulas.
AIAA Pap., **99-0557**.
- U. Ghia, K. N. Ghia and C. T. Shin 1982
High-*Re* solutions for incompressible flow using the Navier-Stokes equations and a multigrid method.
J. Comp. Phys. **48**, 387–411.
- N. Gilbert and L. Kleiser 1986
Subcritical transition to turbulence in channel flows.
In *Direct and Large Eddy Simulation of Turbulence* (U. Schumann and R. Friedrich, eds.), 1–18.
- J. W. Goodrich, K. Gustafson and K. Halasi 1990
Hopf bifurcation in the driven cavity.
J. Comp. Phys., **90**, 219–261.
- P. Hall and N. Horseman 1991
The linear inviscid secondary instability of longitudinal vortex structures in boundary layers.
J. Fluid Mech., **232**, 357–375.
- S. Hein, I. Rosenboom, G. Günther and V. Hannemann 1999
Erste Untersuchungen zur Anwendbarkeit des DLR-TAU-Codes zur Grundströmungsberechnung für nachfolgende Instabilitätsanalysen mit NOLOT/PSE.
DLR *IB 223-99 A30*, 38 pp.

- Th. Herbert 1997
Parabolized stability equations.
Ann. Rev. Fluid Mech., **29**, 245–283.
- C. Hirsch 1988
Numerical computation of internal and external flows. John Wiley & Sons. 2 Vols.
- M. Huntley, A. J. Smits, P. Wu, and R. Miles 1999
Mhz rate imaging of boundary-layer transition on elliptic cones at Mach 8.
AFOSR Contractors' Meeting in Unsteady Aerodynamics and Hypersonics. Wright-Patterson AFB, Dayton OH, Sept. 1999
- J. Jeong and F. Hussain 1995
On the identification of a vortex. *J. Fluid Mech.* **285**, 69–94.
- L. H. Jorgensen 1958
Elliptic cones alone and with wings at supersonic speeds.
NACA Rep. 1378, 975–998.
- A. Karabis, S. J. Shaw, and V. Theofilis 1999
On the inviscid spatial instability of supersonic boundary-layer flow along bodies of revolution.
IUTAM Symposium on Laminar-Turbulent Transition V, Sedona, AZ 1999 (to appear).
- J. Kim and P. Moin 1985
Application of a fractional-step method to incompressible Navier-Stokes equations.
J. Fluid Mech. **59**, 308–323.
- R. L. Kimmel, M. A. Klein, and S. N. Schwoerke 1997
Three-dimensional hypersonic laminar boundary layer computations for transition experiment design.
J. Spacecrafts and Rockets **34** (4), 409–415.
- R. L. Kimmel, J. Poggie, and S. N. Schwoerke 1999
Laminar-turbulent transition in a Mach 8 elliptic cone flow.
AIAA J. **37** (9), 1080–1087.
- R. L. Kimmel and S. H. Walker 1999
Research directions in hypersonic boundary layer transition.
(unpublished).
- L. Kleiser and U. Schumann 1980
Treatment of incompressibility and boundary conditions in 3-D numerical simulations of plane channel flows.
3rd GAMM-Conference on numerical methods in fluid dynamics, (E. H. Hirschel, ed.), 165–173.
- H. C. Ku, R. S. Hirsch and T. D. Taylor 1987
A pseudospectral method for solution of the three-dimensional incompressible Navier-Stokes equations. *J. Comput. Phys.* **70**, 449–462.
- P. D. Lax 1954
Weak solutions of nonlinear hyperbolic equations and their numerical computations.
Comm. Pure App. Math., **7**, 159 – 193.
- N. Y. Lee, W. W. Schultz and J. P. Boyd 1989
Stability of fluid in a rectangular enclosure by spectral method.
Int. J. Heat Mass Transfer, **32**, 513–520.
- C. C. Lin 1955
The Theory of Hydrodynamic Stability.
Cambridge University Press.
- R.-S. Lin and M. R. Malik 1996
On the stability of attachment-line boundary layers. Part 1. The incompressible swept Hiemenz flow.
J. Fluid Mech., **311**, 239–255.
- L. Mack 1969
Boundary layer stability theory.
Doc. 900-277, Jet Propulsion Laboratory, Pasadena, CA. 1.1–15.7 (2 Vols).
- L. Mack 1984
Boundary layer linear stability theory.
AGARD Rep. 709, 3.1–3.81.
- M. R. Malik 1991
Numerical methods for hypersonic boundary layer stability.
J. Comp. Phys. **86**, 376–413.

- L. L. Pauley, P. Moin and W. C. Reynolds 1990
The structure of two-dimensional separation.
J. Fluid Mech. **220**, 397–411.
- R. T. Pierrehumbert 1986
A universal shortwave instability of two-dimensional eddies in an inviscid fluid.
Phys. Rev. Lett. **57**, 2157–2159.
- C. D. Pruett and T. A. Zang 1992
Direct numerical simulation of laminar breakdown in high-speed axisymmetric boundary layers.
Theor. Comp. Fluid Dynamics, **3**, 345–367.
- C. D. Pruett and C.-L. Chang 1998
Direct numerical simulation of hypersonic boundary-layer flow on a flared cone.
Theor. Comp. Fluid Dynamics, **11**, 49–67.
- N. Ramanan and G. M. Homsy 1994
Linear stability of lid-driven cavity flow.
Phys. Fluids, **6**(8), 2690–2701.
- S. J. Shaw and P. W. Duck 1992
The inviscid stability of supersonic flow past heated or cooled axisymmetric bodies.
Phys. Fluids A, **4** (7), 1541–1557.
- J. Shen 1991
Hopf bifurcation of the unsteady regularized driven cavity flow.
J. Comp. Physics, **95**, 228–245.
- R. Schreiber and H. B. Keller 1983
Driven cavity flows by efficient numerical techniques.
J. Comp. Physics, **49**, 310–433.
- G. Sod 1978
A survey of several finite-difference methods for systems of nonlinear hyperbolic conservation laws.
J. Comp. Physics, **22**, 1 – 31.
- P. R. Spalart 1988
Direct simulation of a turbulent boundary layer up to $Re_\theta=1410$. *J. Fluid Mech.* **187**, 61–98”.
- P. R. Spalart, R. D. Moser and M. M. Rogers 1991
Spectral methods for the Navier-Stokes equations with one infinite and two periodic directions.
J. Comp. Physics, **96**, 297–324.
- K. F. Stetson and R. L. Kimmel 1992
On hypersonic boundary-layer stability.
AIAA Paper 92-0737.
- T. Tatsumi and T. Yoshimura 1990
Stability of the laminar flow in a rectangular duct.
J. Fluid Mech. **212**, 437–449.
- V. Theofilis 1995
Spatial stability of incompressible attachment-line flow.
Theor. Comp. Fluid Dynamics, **7**, 159–171.
- V. Theofilis 1998a
On linear and nonlinear instability of the incompressible swept attachment-line boundary layer. *J. Fluid Mech.* **355**, 193–227.
- V. Theofilis 1998b
On the resolution of critical flow regions in inviscid linear and nonlinear instability calculations.
J. Eng. Math., **34**, 111–129.
- V. Theofilis 1998c
Linear instability in two spatial dimensions.
Fourth European CFD Conference ECCOMAS '98, (K.D. Papailiou *et al.* eds.) 547–552.
- V. Theofilis 2000
Globally unstable basic flows in open cavities.
AIAA-Paper No. 2000-1965. 6th AIAA/CEAS Aeroacoustics Conference, June 12–14, Lahaina, Hawaii, USA.
- V. Theofilis, S. Hein and U. Ch. Dallmann 2000
On numerical residuals and physical instabilities in incompressible steady-state fluid flow calculations.
Phil. Trans. Roy. Soc. London A, **358** (to appear).

- V. Theofilis 2001
Advances in global linear instability theory.
Prog. Aero. Sciences (invited).
- W. Tollmien 1929
Über die Entstehung der Turbulenz.
Nachr. Wiss. Ges. Göttingen 21–44.
- M. Visbal and D. Gaitonde 1998
High-order accurate methods for unsteady vortical flows on curvilinear meshes.
AIAA Pap., **98-0131**.
- Y. Wada and M.-S. Liou 1994
A flux-splitting scheme with high-resolution and robustness for discontinuities.
NASA TM 106452 23 pp.
- S. H. Walker 1999
AFOSR Contractors' meeting in unsteady aerodynamics and hypersonics.
Wright-Patterson AFB, Dayton OH, Sept. 1999
- P. Woodward and P. Colella 1984
The numerical simulation of two-dimensional fluid flow with strong shocks.
J. Comp. Physics, **54**, 115–173.
- X. Zhong 1998
High-order finite-difference schemes for numerical simulation of hypersonic boundary-layer transition.
J. Comp. Physics, **144** (2), 662–709.
- X. Zhong 1999
DNS of boundary-layer receptivity to freestream sound for hypersonic flows over blunt elliptical cones.
IUTAM Symposium on Laminar-Turbulent Transition V, Sedona, AZ 1999 (to appear).

List of Figures:	Page:
1 Sketch of the elliptic cone geometry.	57
2 Global view of the grid utilised. Only the surface and farfield discretisation are shown.	58
3 Detail of the near-field discretisation of the elliptic cone surface and the symmetry plane, viewing downstream the cone. The hybrid grid can be seen clearly on the symmetry plane.	59
4 Detail of the near-field discretisation of the elliptic cone surface and the symmetry plane, viewing upstream the cone. The discretisation of the cone base is also seen in this plot.	60
5 Two shock-tube problems solved by an AUSMDV flux-vector splitting. The primitive variables ρ, u, p and T are presented for Sod's problem in the upper figure and for Lax's problem in the lower figure at times $t = 2$ and 1.3 , respectively. In both cases a uniform grid with $\Delta x = 1/100$ has been used.	61
6 The solution to the blast wave problem at $t = 0.38$ obtained on a uniform grid with $\Delta x = 1/1000$.	62
7 Convergence history of the blast wave problem solution (upper) and detail of this result (lower).	63
8 Isosurface of pressure at $t = 2$ in the two-dimensional Sod problem.	64
9 An aspect-ratio $A = 3$ elliptic cone model at $Re = 10^3, M = 0.5, \alpha = 10^\circ$; shown are contour lines equidistributed between the minimum and maximum values of the x -wise velocity component u on the planes $x = 0.7$ and $y = 0$.	65
10 An aspect-ratio $A = 3$ elliptic cone model at $Re = 10^3, M = 0.5, \alpha = 10^\circ$; shown are contour lines equidistributed between the minimum and maximum values of the y -wise velocity component v on the plane $x = 0.7$. The condition $v \equiv 0$ is satisfied on the symmetry plane on account of the symmetry imposed.	66
11 An aspect-ratio $A = 3$ elliptic cone model at $Re = 10^3, M = 0.5, \alpha = 10^\circ$; shown are contour lines equidistributed between the minimum and maximum values of the z -wise velocity component w on the planes $x = 0.7$ and $y = 0$.	67
12 An aspect-ratio $A = 3$ elliptic cone model at $Re = 10^3, M = 0.5, \alpha = 20^\circ$; shown are contour lines equidistributed between the minimum and maximum values of the x -wise velocity component u on the planes $x = 0.7$ and $y = 0$.	68
13 An aspect-ratio $A = 3$ elliptic cone model at $Re = 10^3, M = 0.5, \alpha = 20^\circ$; shown are contour lines equidistributed between the minimum and maximum values of the y -wise velocity component v on the plane $x = 0.7$. The condition $v \equiv 0$ is satisfied on the symmetry plane on account of the symmetry imposed.	69
14 An aspect-ratio $A = 3$ elliptic cone model at $Re = 10^3, M = 0.5, \alpha = 20^\circ$; shown are contour lines equidistributed between the minimum and maximum values of the z -wise velocity component w on the planes $x = 0.7$ and $y = 0$.	70

	List of Figures (continued):	Page:
15	An aspect-ratio $A = 3$ elliptic cone model at $Re = 10^3$, $M = 2.0$, $\alpha = 20^\circ$; shown are contour lines equidistributed between the minimum and maximum values of ρ on the planes $x = 0.7$ and $y = 0$.	71
16	An aspect-ratio $A = 3$ elliptic cone model at $Re = 10^3$, $M = 2.0$, $\alpha = 20^\circ$; shown are contour lines equidistributed between the minimum and maximum values of the x -wise velocity component u on the planes $x = 0.7$ and $y = 0$.	72
17	An aspect-ratio $A = 3$ elliptic cone model at $Re = 10^3$, $M = 2.0$, $\alpha = 20^\circ$; shown are contour lines equidistributed between the minimum and maximum values of the y -wise velocity component v on the plane $x = 0.7$. The condition $v \equiv 0$ is satisfied on the symmetry plane on account of the symmetry imposed.	73
18	An aspect-ratio $A = 3$ elliptic cone model at $Re = 10^3$, $M = 2.0$, $\alpha = 20^\circ$; shown are contour lines equidistributed between the minimum and maximum values of the z -wise velocity component w on the planes $x = 0.7$ and $y = 0$.	74
19	An aspect-ratio $A = 3$ elliptic cone model at $Re = 10^3$, $M = 2.0$, $\alpha = 20^\circ$; shown are contour lines equidistributed between the minimum and maximum values of p on the planes $x = 0.7$ and $y = 0$.	75
20	A qualitatively self-similar flowfield pattern of the z -wise velocity component w obtained on the elliptic cone at $M = 2$, $\alpha = 20^\circ$.	76
21	An aspect-ratio $A = 3$ elliptic cone model at $Re = 10^3$, $M = 4.0$, $\alpha = 20^\circ$; shown are contour lines equidistributed between the minimum and maximum values of ρ on the planes $x = 0.7$ and $y = 0$.	77
22	An aspect-ratio $A = 3$ elliptic cone model at $Re = 10^3$, $M = 4.0$, $\alpha = 20^\circ$; shown are contour lines equidistributed between the minimum and maximum values of the x -wise velocity component u on the planes $x = 0.7$ and $y = 0$.	78
23	An aspect-ratio $A = 3$ elliptic cone model at $Re = 10^3$, $M = 4.0$, $\alpha = 20^\circ$; shown are contour lines equidistributed between the minimum and maximum values of the y -wise velocity component v on the plane $x = 0.7$. The condition $v \equiv 0$ is satisfied on the symmetry plane on account of the symmetry imposed.	79
24	An aspect-ratio $A = 3$ elliptic cone model at $Re = 10^3$, $M = 4.0$, $\alpha = 20^\circ$; shown are contour lines equidistributed between the minimum and maximum values of the z -wise velocity component w on the planes $x = 0.7$ and $y = 0$.	80
25	An aspect-ratio $A = 3$ elliptic cone model at $Re = 10^3$, $M = 4.0$, $\alpha = 20^\circ$; shown are contour lines equidistributed between the minimum and maximum values of p on the planes $x = 0.7$ and $y = 0$.	81

List of Figures (concluded):	Page:
26 Convergence history of stream function $\psi(0.5, 0.5)$ against time (left) and slope of this curve (right). Lower to upper curves, $Re = 100, 200$ and 300 , respectively.	82
27 Convergence history of $\psi(0.5, 0.5)$ against time at $Re = 500$ (upper left) and its slope (upper right); lower left and right, respectively, the corresponding results at $Re = 1000$. In both cases superimposed and denoted by symbols are the eigenvalues of the two least stable stationary modes.	83
28 a) The dependence of the function $d(\ln \psi^t)/dt$ on time t , showing the exponential decay of a single travelling mode ($\Omega_r \approx 0.97 \pm 0.01$) superimposed upon the least damped exponentially decaying stationary disturbance at $Re = 2500$.	84
29 b) $Re = 5000$	85
30 c) $Re = 7500$	86
31 a) The correspondence of the frequencies of the damped linear ($\lambda = 0$) two-dimensional eigenmodes of the converged steady-states at different Reynolds numbers and those obtained from discrete Fourier transforms of the DNS signals. $Re = 2500$.	87
32 b) $Re = 5000$	88
33 c) $Re = 7500$	89
34 The filling up of the eigenvalue spectrum as Reynolds number increases; $Re = 2500$ (diamond), 5000 (square), and 7500 (triangle).	90
35 The dependence of the damping rate Ω_i of the least damped two-dimensional eigenmode of the converged steady-state at a Reynolds number on Re as predicted by the model (6.21) denoted by the solid line, and as calculated by numerical solution of the eigenvalue problem (6.6-6.9) denoted by the symbols.	91
36 The spatial distribution of the difference $\Delta\tilde{\psi}(x, y) \equiv \tilde{\psi} - \bar{\psi}$ at $Re = 100$ using $Nx = Ny = 48$ Jacobi collocation points.	92
37 An estimate of the converged solution $\tilde{\psi}$ at $Re = 100$ obtained by evaluating (6.15) at $t = 15$ and using $Nx = Ny = 48$ Jacobi collocation points. Iso-contours are drawn at the levels shown by Ghia <i>et al.</i> (1982)	93

Variable	Left state (subscript $_L$) $0.0 < x < 0.1$	Middle state (subscript $_M$) $0.1 \leq x \leq 0.9$	Right state (subscript $_R$) $0.9 \leq x \leq 1.0$
ρ	1	1	1
u	0	0	0
p	10^3	10^{-2}	10^2

Table 1. *Initial conditions for the blast-wave problem*

$\Delta x \times 10^4$	ρ	u	p	T
$x = 0$				
10	0.1624	0.0116	73.9501	0.0001
5	0.1580	0.0057	72.4378	0.0000
2	0.1531	0.0023	70.3934	0.0000
1	0.1507	0.0012	69.3482	0.0000
0.5	0.1493	0.0006	68.8574	0.0000
$x = 1$				
10	0.3201	-0.0003	19.2320	0.0000
5	0.3170	-0.0002	19.2811	0.0000
2	0.3140	-0.0001	19.2941	0.0000
1	0.3124	-0.0000	19.2941	0.0000
0.5	0.3113	-0.0000	19.2939	0.0000

Table 2. Convergence of the wall values of the primitive variables in the blast wave problem

		$Re = 400$		
		Ghia <i>et al.</i> (1982)	Schreiber and Keller (1983)	present results
Primary	ψ	-0.1139	-0.1140	-0.1139
	ζ	2.29469	2.281	2.29584
	(x, y)	(0.5547, 0.6055)	(0.5571, 0.6071)	(0.5535, 0.6054)
LL	ψ	1.42×10^{-5}	1.45×10^{-5}	1.40×10^{-5}
	ζ	-0.0570	-0.0471	-0.05685
	(x, y)	(0.0508, 0.0469)	(0.0500, 0.0429)	(0.0510, 0.0466)
LR	ψ	6.42×10^{-4}	6.44×10^{-4}	6.41×10^{-4}
	ζ	-0.4335	-0.394	-0.44802
	(x, y)	(0.8906, 0.1250)	(0.8857, 0.1143)	(0.8852, 0.1217)

		$Re = 1000$		
		Ghia <i>et al.</i> (1982)	Schreiber and Keller (1983)	present results
Primary	ψ	-0.117929	-0.11603	-0.118902
	ζ	2.04968	2.02600	2.068251
	(x, y)	(0.5313, 0.5625)	(0.52857, 0.56429)	(0.529654, 0.565018)
LL	ψ	2.31×10^{-4}	2.17×10^{-3}	2.354097×10^{-4}
	ζ	-0.36175	-0.302	-0.337187
	(x, y)	(0.0859, 0.0781)	(0.08571, 0.07143)	(0.081549, 0.077839)
LR	ψ	1.75×10^{-3}	1.70×10^{-3}	1.744028×10^{-3}
	ζ	-1.15465	-0.999	-1.097921
	(x, y)	(0.8594, 0.1094)	(0.86429, 0.10714)	(0.867381, 0.114469)

		$Re = 3200$			
		Primary	UL	LL	LR
GGS	ψ	-0.12038	7.27682×10^{-4}	9.7823×10^{-4}	3.14×10^{-3}
	ζ	1.98860	-1.71161	-1.06301	-2.27365
	(x, y)	(0.5165, 0.5469)	(0.0547, 0.8984)	(0.0859, 0.1094)	(0.81255, 0.0859)
present	ψ	-0.12181	7.11201×10^{-4}	1.12331×10^{-3}	2.82648×10^{-3}
	ζ	1.961154	-1.65335	-1.16397	-2.24381
	(x, y)	(0.51722, 0.54089)	(0.0524, 0.8981)	(0.08106, 0.12052)	(0.82281, 0.084648)

		$Re = 4000$			
		Primary	UL	LL	LR
SK	ψ	-0.11237		1.12×10^{-3}	2.80×10^{-3}
	ζ	1.805		-1.067	-2.145
	(x, y)	(0.51875, 0.53750)		(0.08125, 0.11875)	(0.81875, 0.07500)
present	ψ	-0.12203	1.073×10^{-3}	1.24736×10^{-3}	2.95426×10^{-3}
	ζ	1.94949	-1.91234	-1.27899	-2.42032
	(x, y)	(0.51597, 0.53846)	(0.06098, 0.90387)	(0.08055, 0.12482)	(0.81640, 0.07983)

Contract No. F61775-99-WE049.

Table 3. Location and value of the maxima of the primary and the lower-left (LL), lower-right (LR) and upper-left (UL) secondary vortices in the steady state solution for ψ and ζ at $Re = 400, 1000, 3200$ and 4000 ; comparisons with Ghia *et al.* (1982) (GGS) and Schreiber and Keller (1983) (SK).

$Re = 400$								
	Primary			UL			LL	
	ψ	ζ		ψ	ζ		$10^5\psi$	ζ
							$10^4\psi$	LR ζ
GGS	-0.113909	2.29469				1.41951	-0.05697	6.42352
present	-0.113989	2.29463				1.47210	-0.05711	6.42406
SK	-0.11399*	2.2898*				1.45	-0.04710	6.440
present	-0.113982	2.29184				1.40	-0.04766	6.373
								-0.4335
								-0.4329
								-0.3940
								-0.4030
$Re = 1000$								
	Primary			UL			LL	
	ψ	ζ		ψ	ζ		$10^4\psi$	ζ
							$10^3\psi$	LR ζ
GGS	-0.117929	2.04968				2.31129	-0.36175	1.75102
present	-0.118902	2.06839				2.37806	-0.36575	1.77911
SK	-0.11894*	2.0677*				2.1700	-0.302000	1.700
present	-0.118905	2.068234				2.3151	-0.312162	1.763
								-1.1547
								-1.1486
								-0.9990
								-1.0481
$Re = 3200$								
	Primary			UL			LL	
	ψ	ζ		$10^4\psi$	ζ		$10^3\psi$	ζ
							$10^3\psi$	LR ζ
GGS	-0.120377	1.9886	7.27	-1.71161	0.98	-1.06301	3.14	-2.27365
present	-0.121777	1.9612	7.08	-1.73137	1.09	-1.00607	2.77	-2.25511
$Re = 4000$								
	Primary			UL			LL	
	ψ	ζ		ψ	ζ		$10^3\psi$	ζ
							$10^3\psi$	LR ζ
SK	-0.12202*	1.9498*				1.1200	-1.0670	2.8000
present	-0.122026	1.94960				1.2411	-1.1427	2.9228
								-2.14500
								-2.31944

Table 4. Comparison of the interpolated values of our solutions on the maxima presented by Ghia et al. (1982) and Schreiber and Keller (1983). An asterisk denotes Richardson-extrapolated data in the latter work.

λ	Ω_r	RH Ω_i	DK Ω_i	present results Ω_r	present results Ω_i
1	± 0.00	-0.34	-0.3183	± 0.0000	-0.3297
2	± 0.00	-0.23	-0.2248	± 0.0000	-0.2267
3	± 0.11	-0.29	-0.2924	± 0.1073	-0.2954
4	± 0.28	-0.30	-0.2969	± 0.2810	-0.2956
5	± 0.43	-0.34	-0.3431	± 0.4260	-0.3404
6	± 0.58	-0.39	-0.3893	± 0.5821	-0.3844
7	± 0.67	-0.41	-0.4073	± 0.6733	-0.4013
8	± 0.72	-0.45	-0.4637	± 0.7232	-0.4587
9	± 0.76	-0.54	-0.5504	± 0.7622	-0.5473

Table 5. Comparison of the least stable eigenmode at $Re = 200$ against the results of Ramanan and Homsy (1994) (RH) and the graphically (digitally) reproduced growth rate result of Ding and Kawahara (1998) (DK).

Resolution	<i>Re</i>		
	100	200	300
	σ	σ	σ
16×16	-0.5404	-0.3248	-0.2865
24×24	-0.5407	-0.3319	-0.2843
32×32	-0.5409	-0.3318	-0.2842
40×40	-0.5409	-0.3318	-0.2842
Ω_i	-0.5410	-0.3319	-0.2845

Table 6. Numerical results for the rate of decay of residuals σ as a function of resolution at different low Reynolds numbers. Also shown the result of numerical solution of (6.6-6.9) for the imaginary part of the eigenvalue Ω_i , using the respective converged steady-state as basic flow.

Re	Ω_i	$\frac{ \Omega_i - \sigma }{ \sigma } \times 100$
2500	-0.0253	1.2
5000	-0.0112	8.9
7500	-0.0093	17.8

Table 7. Numerical results for the damping rate Ω_i of the least stable ($\lambda = 0$)-eigenmode at $Re = 2500, 5000$ and 7500 and its discrepancy in percentage terms from the rate of decay of residuals σ .

$Re = 100$				
Resolution	16×16	24×24	32×32	
Δt	0.01	0.01	0.005	
\bar{t}	50.43	50.42	49.005	
\tilde{t}	12.71	12.79	11.07	
$-\sigma$	0.540246	0.540214	0.540876	
$\max(\Delta\tilde{\psi})$	5.3(-8)	8.8(-7)	4.6(-6)	
$\min(\Delta\tilde{\psi})$	3.6(-9)	7.9(-8)	5.1(-7)	
$\max(\Delta\psi)$	3.4(-4)	3.5(-4)	1.0(-3)	
$\min(\Delta\psi)$	1.5(-5)	1.2(-3)	1.6(-2)	

$Re = 1000$				
Resolution	24×24	32×32	40×40	
Δt	0.01	0.01	0.01	
\bar{t}	325.93	323.61	324.33	
\tilde{t}	77.82	77.53	77.81	
$-\sigma$	0.065808	0.065657	0.065336	
$\max(\Delta\tilde{\psi})$	2.9(-6)	9.5(-5)	3.1(-5)	
$\min(\Delta\tilde{\psi})$	4.9(-7)	3.2(-6)	3.3(-6)	
$\max(\Delta\psi)$	3.7(-4)	3.6(-4)	2.5(-4)	
$\min(\Delta\psi)$	3.7(-4)	5.1(-4)	3.3(-4)	

Table 8. Recovery of $\tilde{\psi}$ from transient data at $Re = 400$ and 1000 as function of resolution and time-step used in the DNS. $x(y) \equiv x \times 10^y$.

$\frac{\bar{t}}{\bar{\tau}} \times 100$	$\max(\Delta\psi)$	$\min(\Delta\psi)$	$\frac{ \sigma - \Omega_i }{ \Omega_i } \times 100$
$Re = 100$			
22.59	4.6(−6)	5.1(−7)	0.023
25.02	4.0(−8)	1.9(−8)	0.018
30.90	2.5(−9)	1.2(−9)	0.011
35.12	1.8(−10)	1.0(−10)	0.009
$Re = 1000$			
23.99	3.1(−5)	3.3(−6)	3.97
25.02	1.3(−5)	1.5(−6)	3.35
30.23	2.1(−6)	1.2(−7)	0.65
35.02	1.5(−8)	5.8(−9)	0.24

Table 9. Recovery of \mathbf{Q}_i at several Reynolds numbers from transient data at times beyond that at which ω converges. The discrepancy between σ and Ω_i of the least stable eigenmode is also presented. $Re = 100$ run on a 32^2 grid; $Re = 1000$ run on a 40^2 grid. $x(y) \equiv x \times 10^y$.

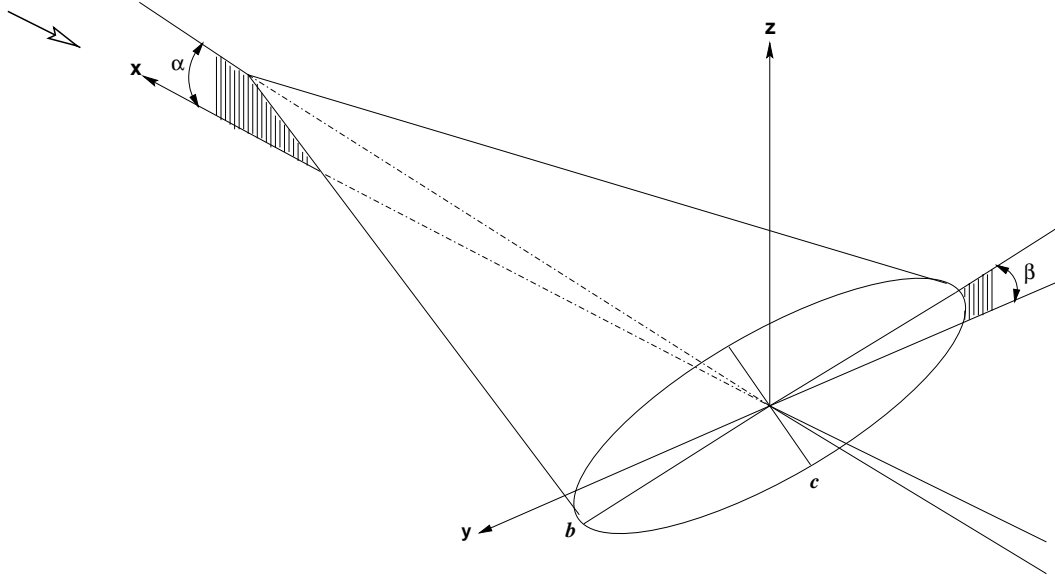


Figure 1. Sketch of the elliptic cone geometry.

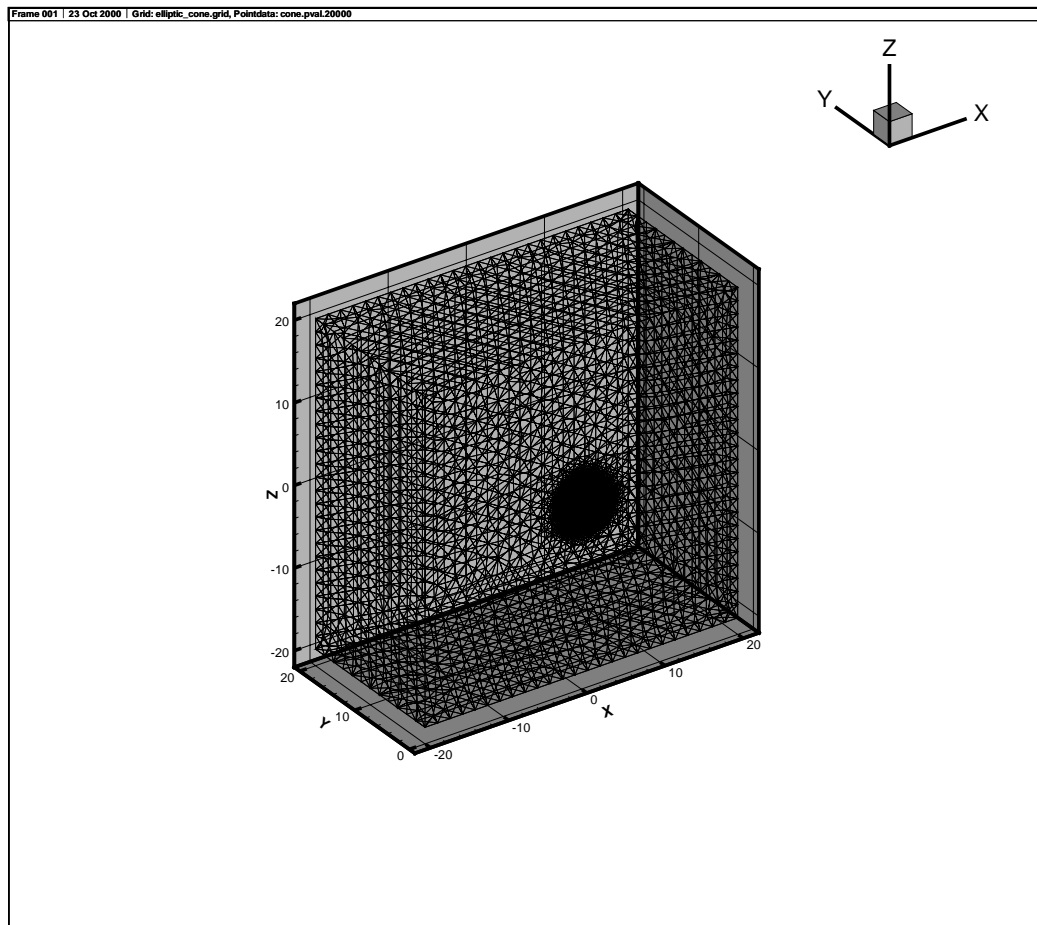


Figure 2. Global view of the grid utilised. Only the surface and farfield discretisation are shown.

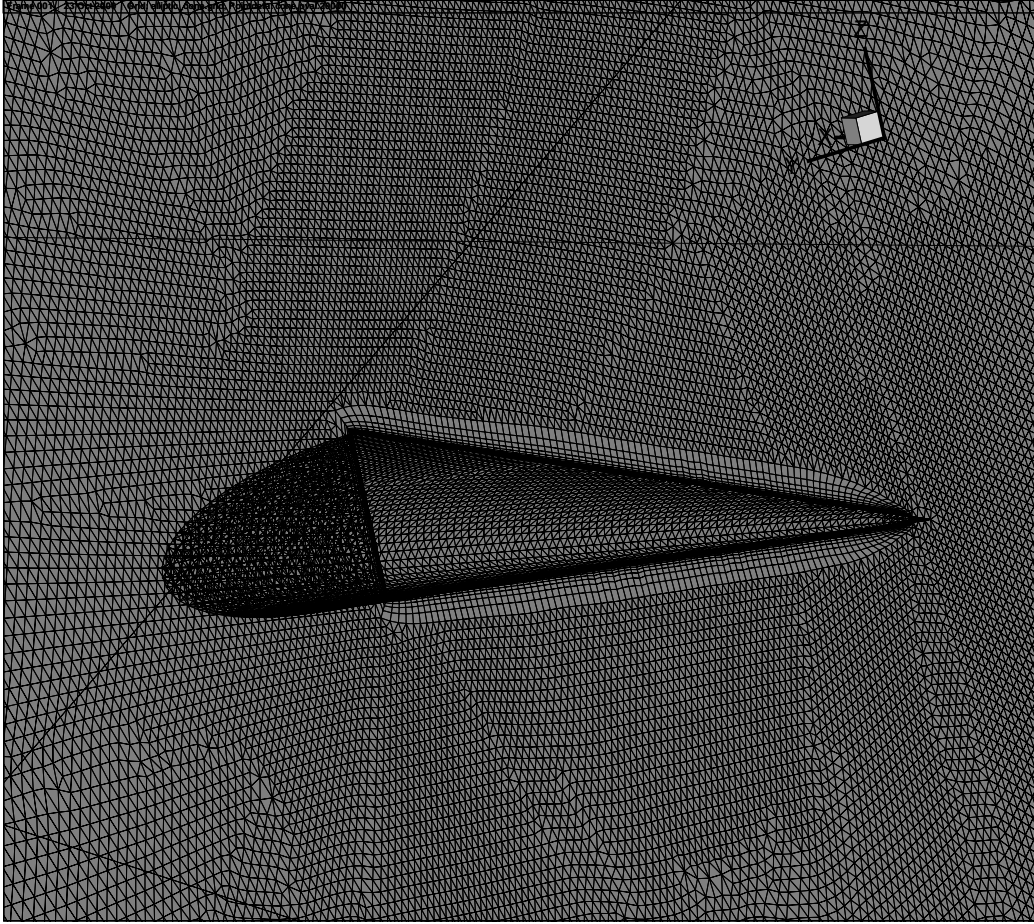


Figure 3. Detail of the near-field discretisation of the elliptic cone surface and the symmetry plane, viewing downstream the cone. The hybrid grid can be seen clearly on the symmetry plane.

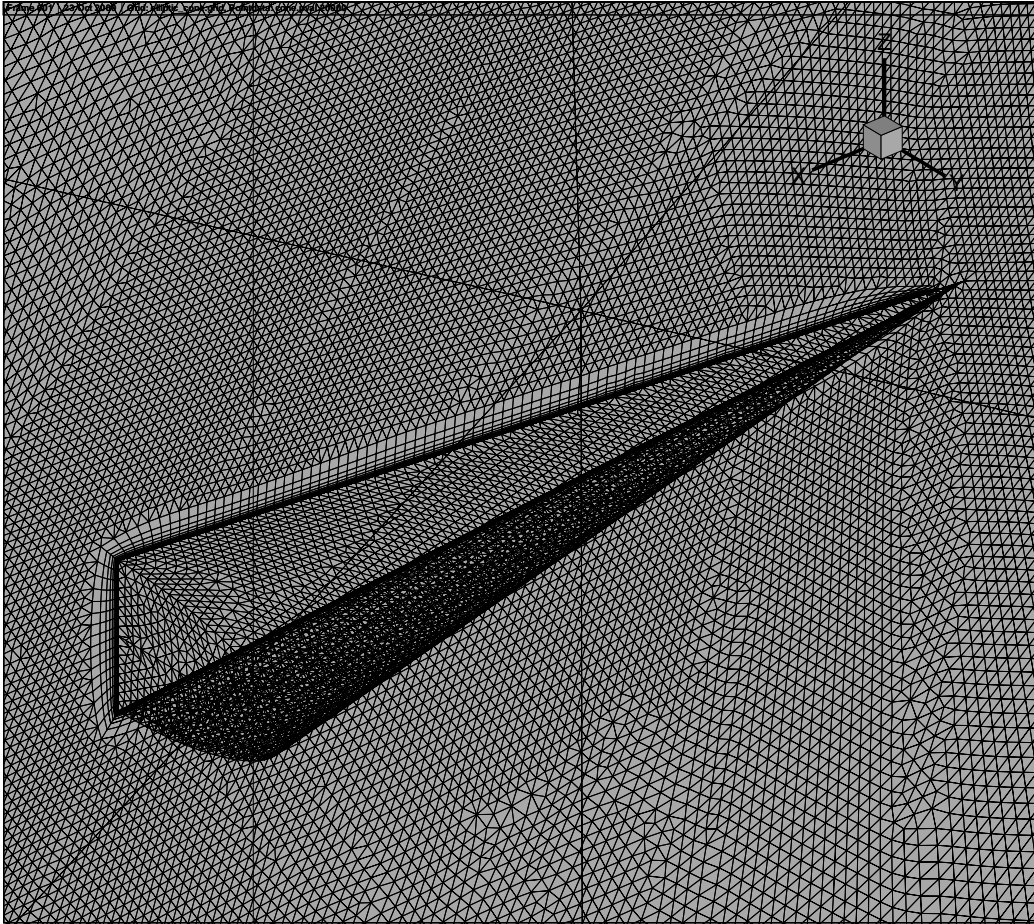


Figure 4. Detail of the near-field discretisation of the elliptic cone surface and the symmetry plane, viewing upstream the cone. The discretisation of the cone base is also seen in this plot.

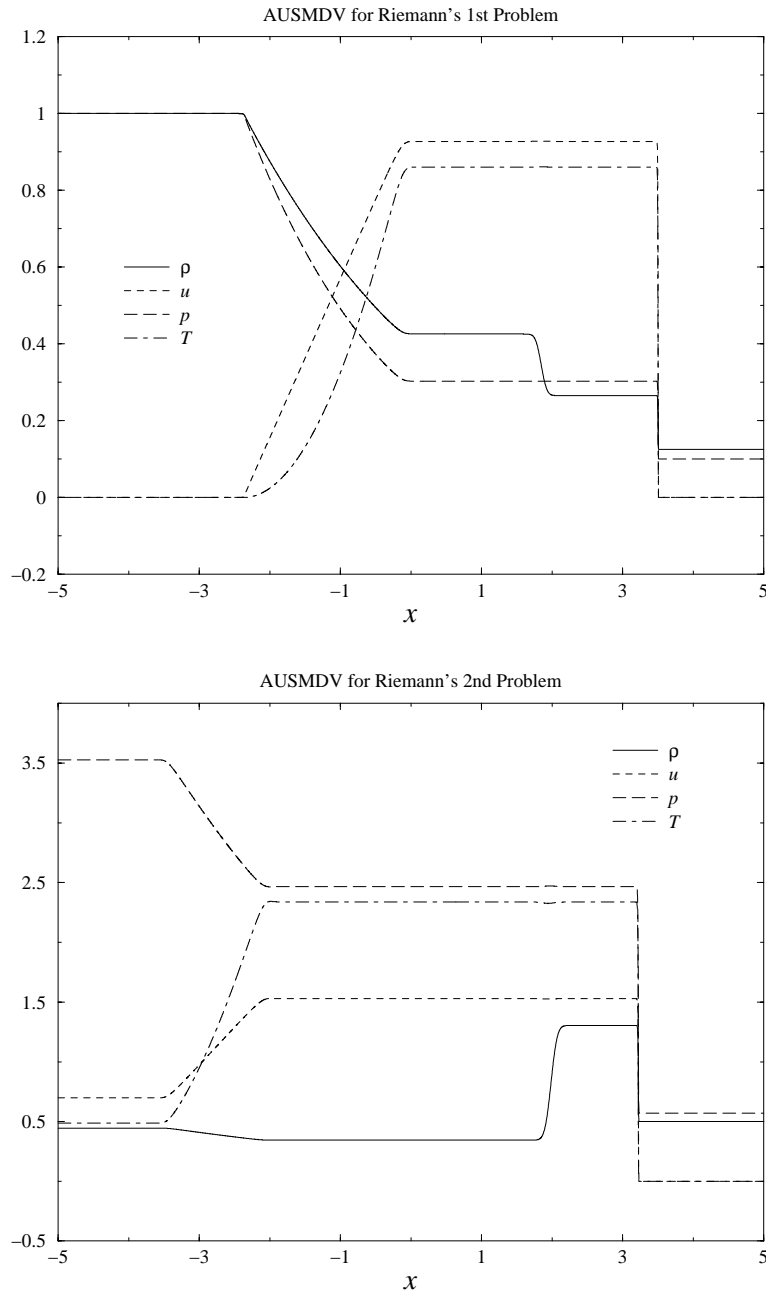


Figure 5. Two shock-tube problems solved by an AUSMDV flux-vector splitting. The primitive variables ρ, u, p and T are presented for Sod's problem in the upper figure and for Lax's problem in the lower figure at times $t = 2$ and 1.3, respectively. In both cases a uniform grid with $\Delta x = 1/100$ has been used.

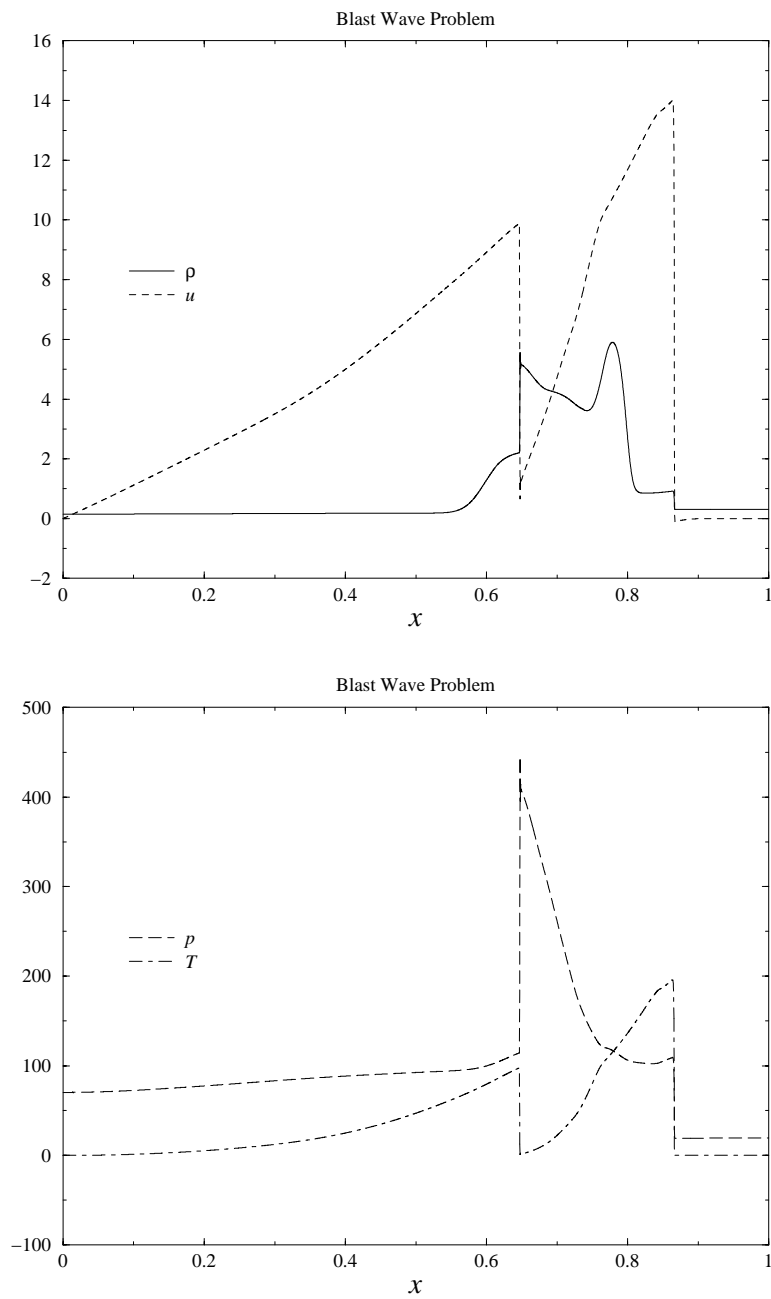


Figure 6. The solution to the blast wave problem at $t = 0.38$ obtained on a uniform grid with $\Delta x = 1/1000$.

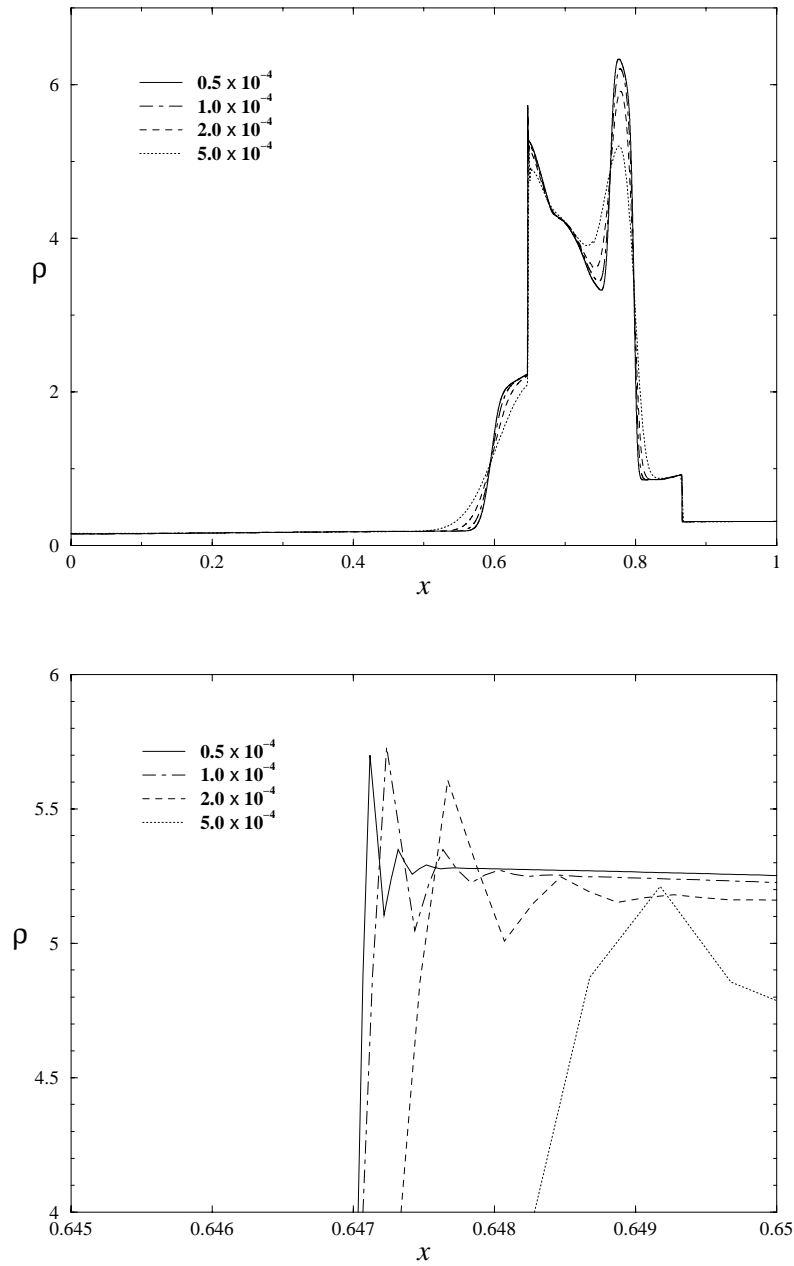


Figure 7. Convergence history of the blast wave problem solution (upper) and detail of this result (lower).

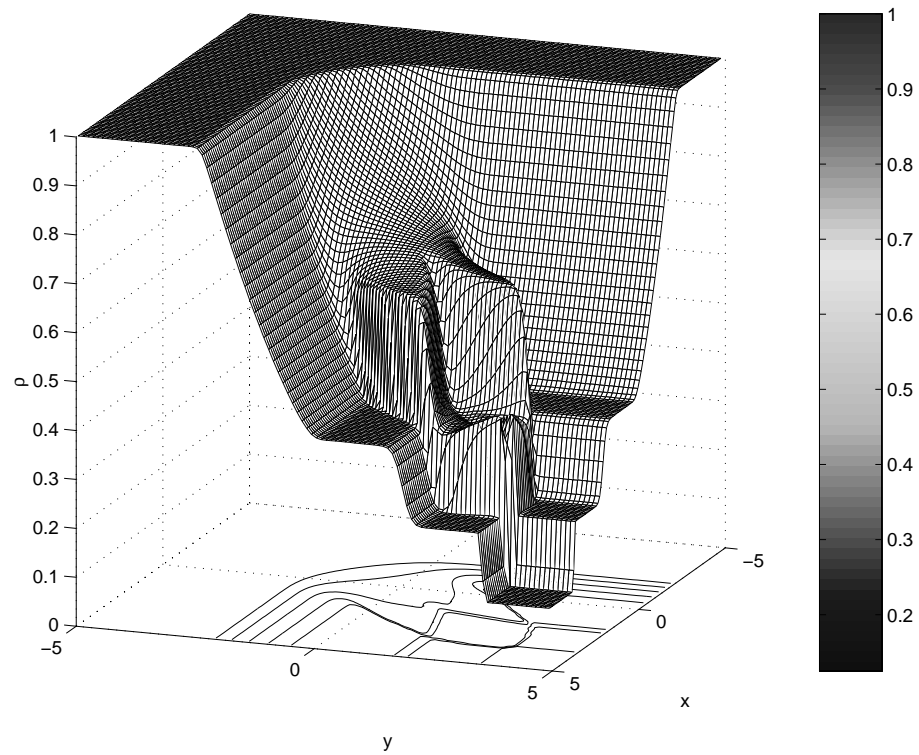


Figure 8. Isosurface of pressure at $t = 2$ in the two-dimensional Sod problem.

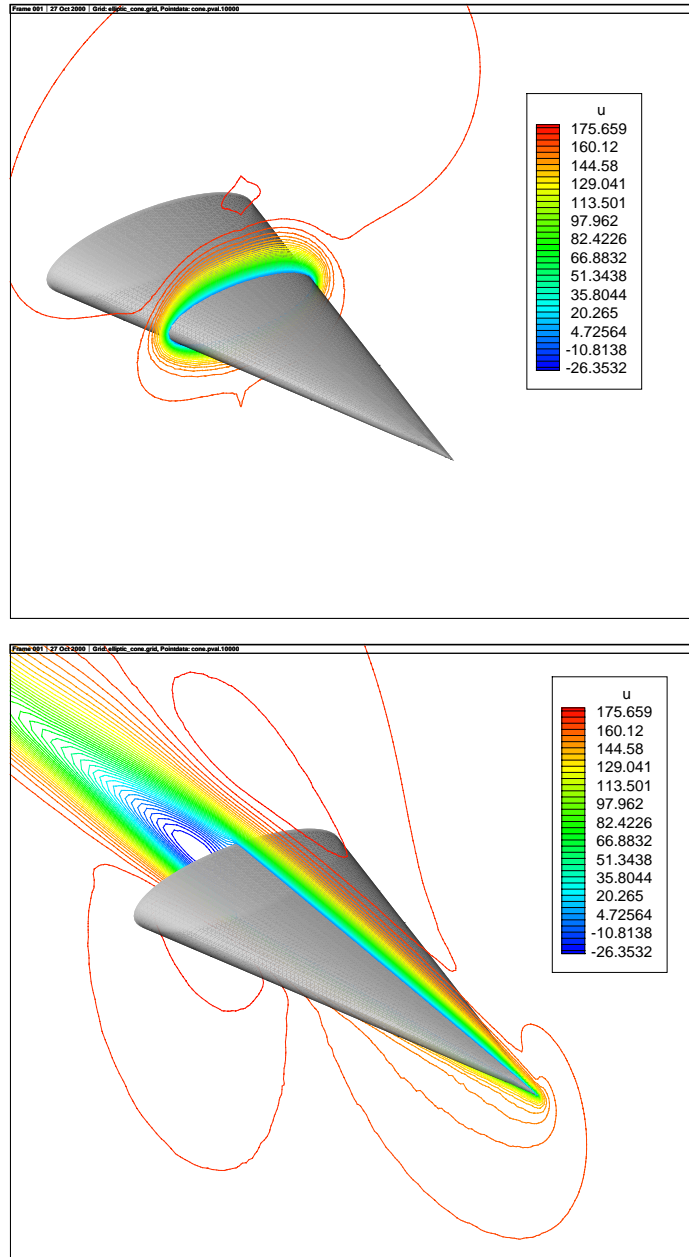


Figure 9. An aspect-ratio $A = 3$ elliptic cone model at $Re = 10^3$, $M = 0.5$, $\alpha = 10^\circ$; shown are contour lines equidistributed between the minimum and maximum values of the x -wise velocity component u on the planes $x = 0.7$ and $y = 0$.

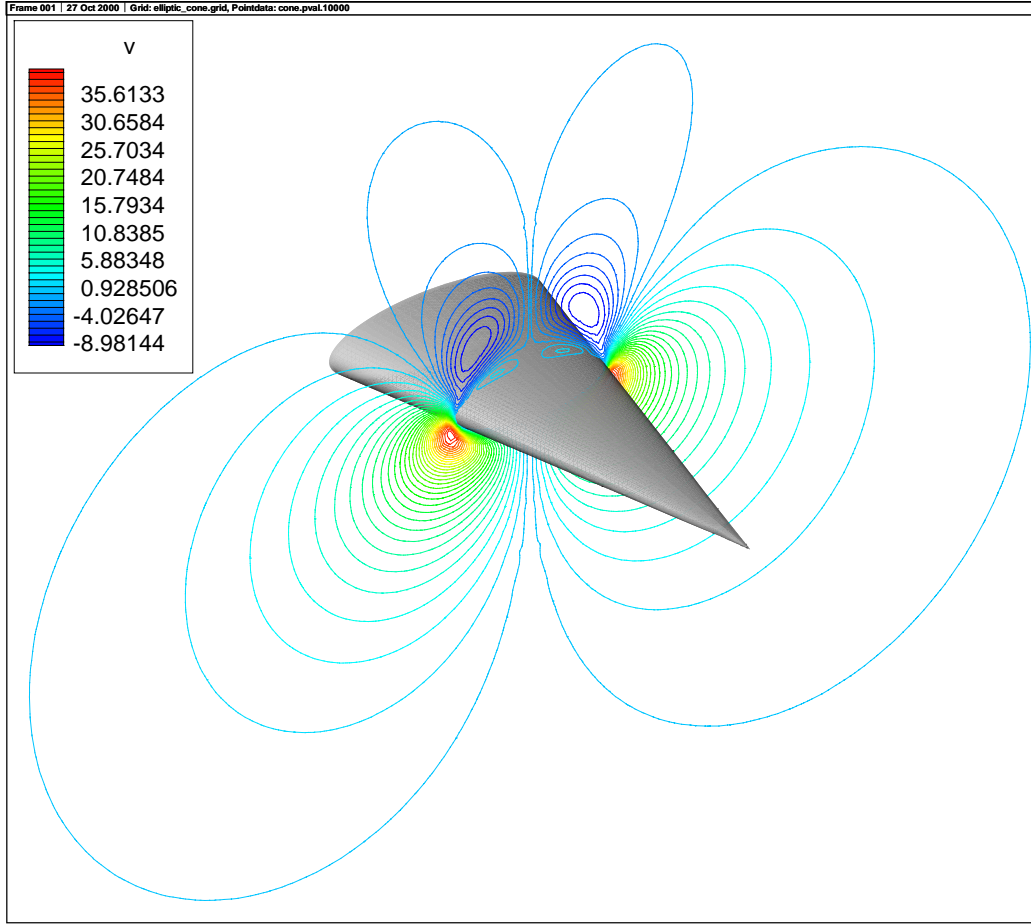


Figure 10. An aspect-ratio $A = 3$ elliptic cone model at $Re = 10^3$, $M = 0.5$, $\alpha = 10^\circ$; shown are contour lines equidistributed between the minimum and maximum values of the y -wise velocity component v on the plane $x = 0.7$. The condition $v \equiv 0$ is satisfied on the symmetry plane on account of the symmetry imposed.

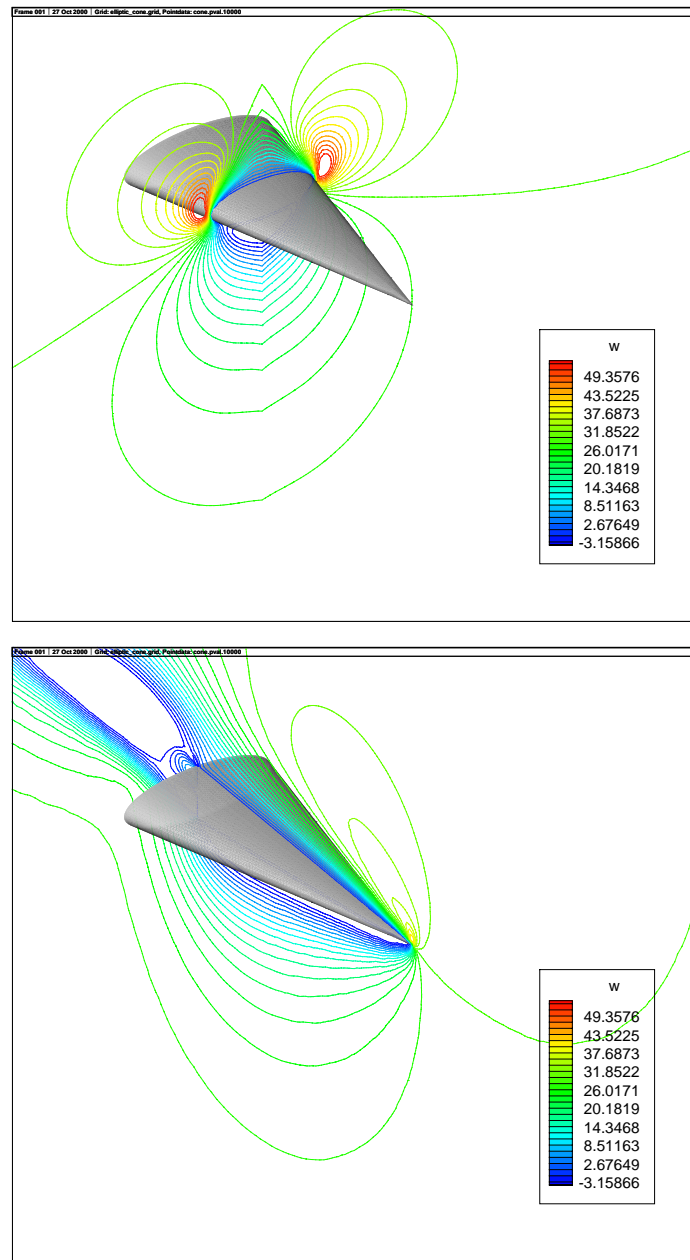


Figure 11. An aspect-ratio $A = 3$ elliptic cone model at $Re = 10^3$, $M = 0.5$, $\alpha = 10^\circ$; shown are contour lines equidistributed between the minimum and maximum values of the z -wise velocity component w on the planes $x = 0.7$ and $y = 0$.

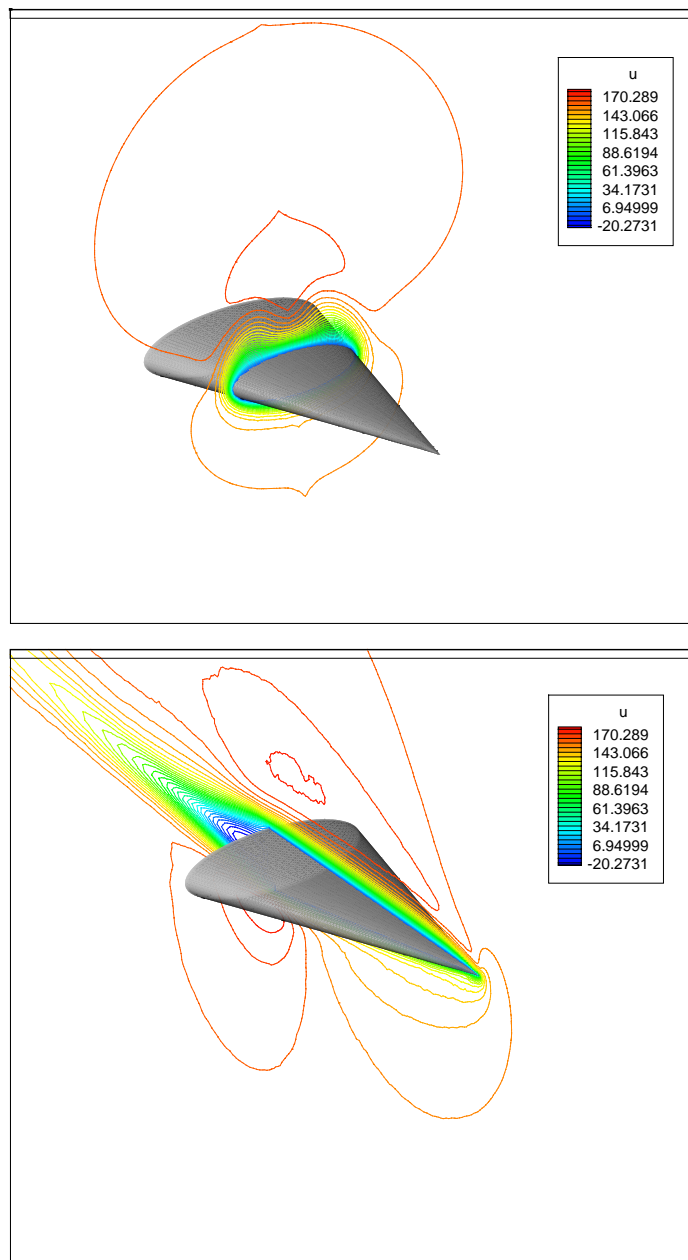


Figure 12. An aspect-ratio $A = 3$ elliptic cone model at $Re = 10^3$, $M = 0.5$, $\alpha = 20^\circ$; shown are contour lines equidistributed between the minimum and maximum values of the x -wise velocity component u on the planes $x = 0.7$ and $y = 0$.

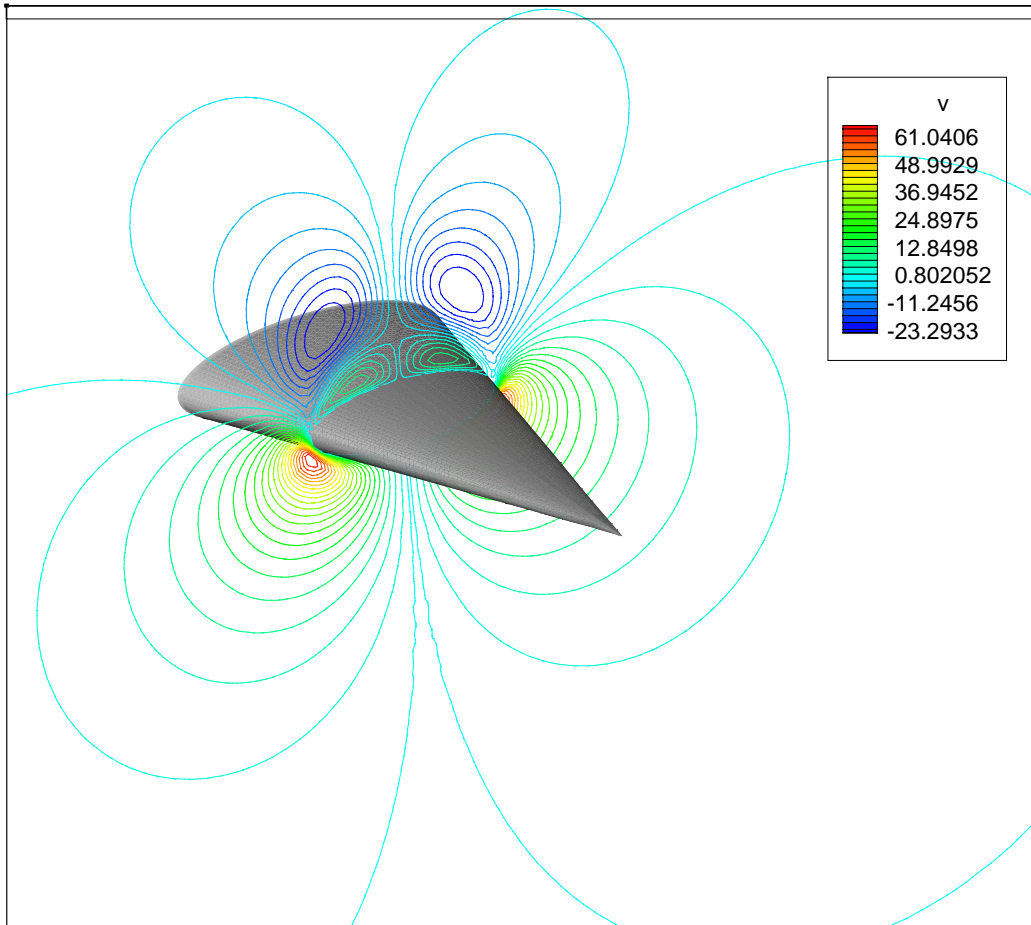


Figure 13. An aspect-ratio $A = 3$ elliptic cone model at $Re = 10^3$, $M = 0.5$, $\alpha = 20^\circ$; shown are contour lines equidistributed between the minimum and maximum values of the y -wise velocity component v on the plane $x = 0.7$. The condition $v \equiv 0$ is satisfied on the symmetry plane on account of the symmetry imposed.

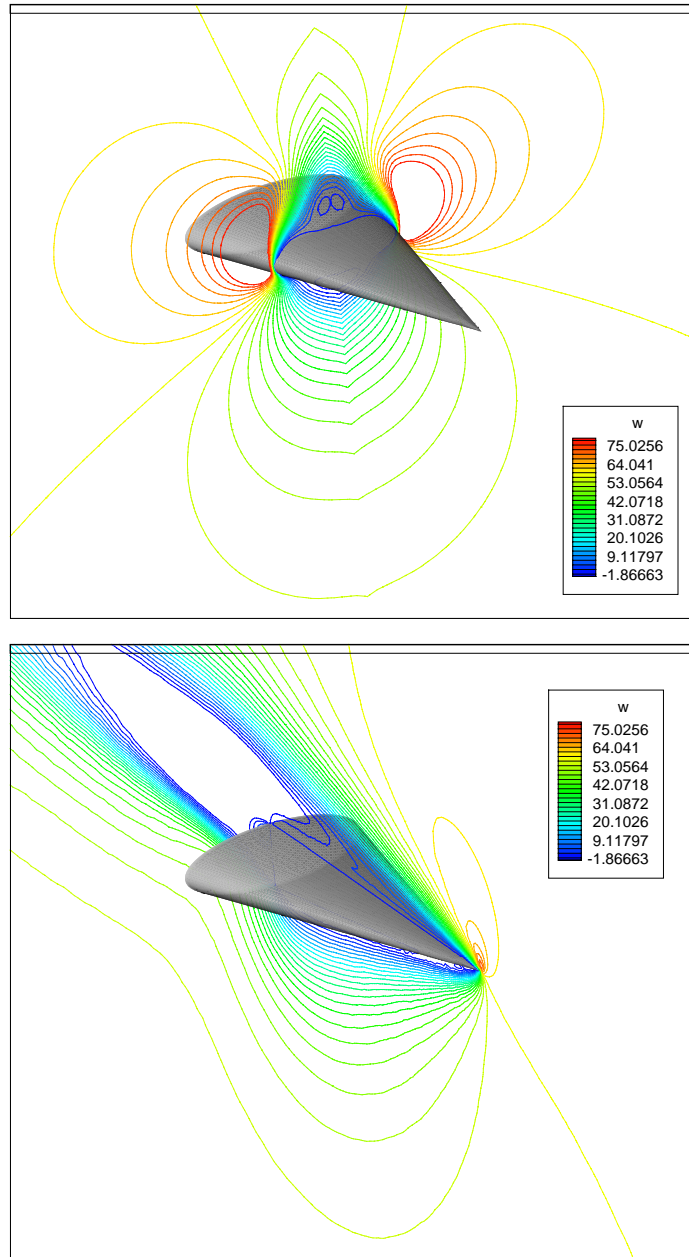


Figure 14. An aspect-ratio $A = 3$ elliptic cone model at $Re = 10^3$, $M = 0.5$, $\alpha = 20^\circ$; shown are contour lines equidistributed between the minimum and maximum values of the z -wise velocity component w on the planes $x = 0.7$ and $y = 0$.

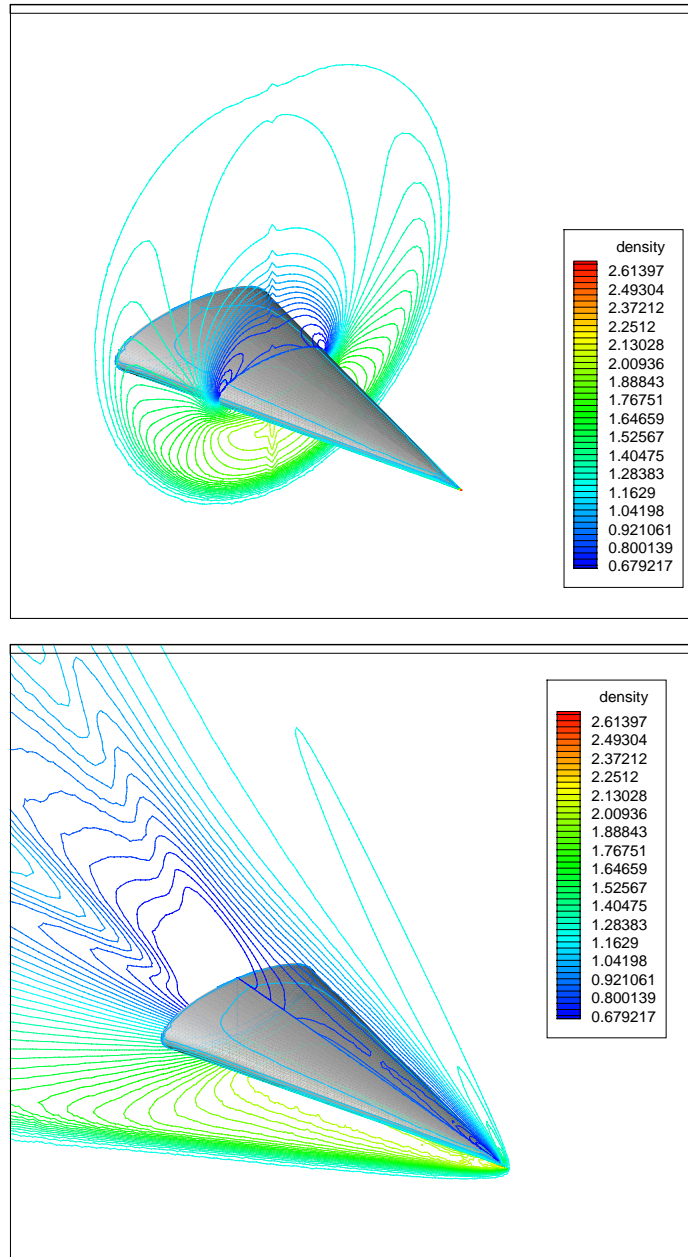


Figure 15. An aspect-ratio $A = 3$ elliptic cone model at $Re = 10^3$, $M = 2$, $\alpha = 20^\circ$; shown are contour lines equidistributed between the minimum and maximum values of ρ on the planes $x = 0.7$ and $y = 0$.

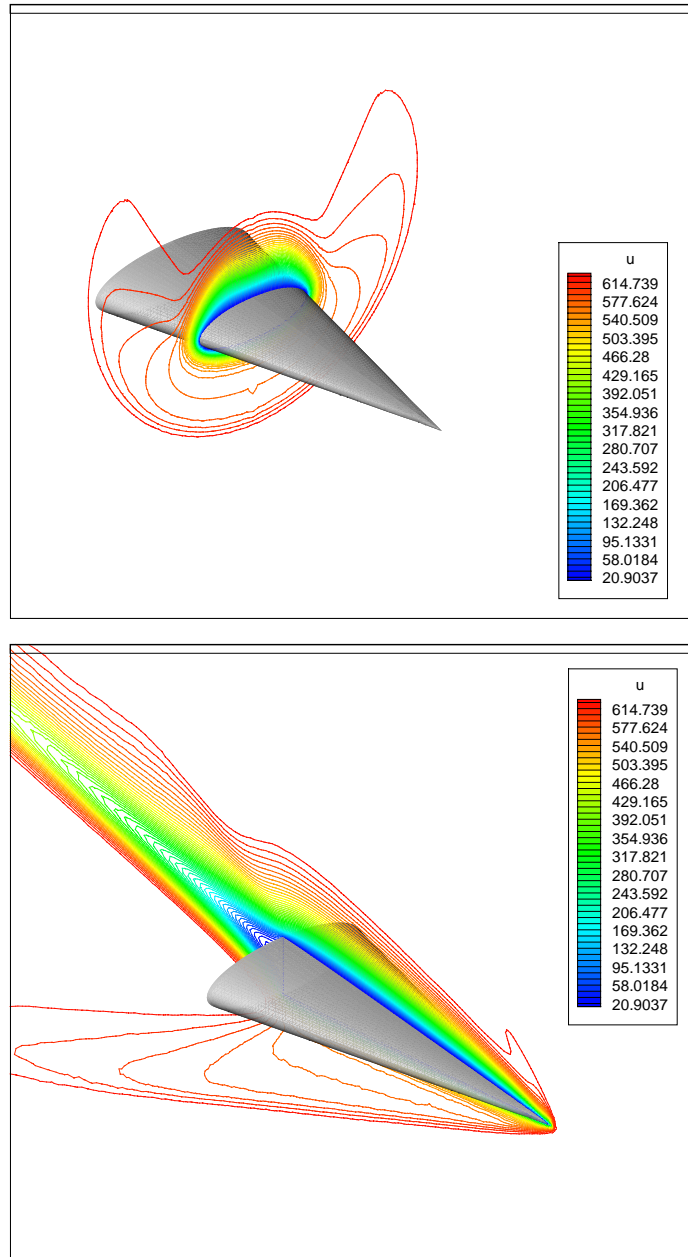


Figure 16. An aspect-ratio $A = 3$ elliptic cone model at $Re = 10^3$, $M = 2$, $\alpha = 20^\circ$; shown are contour lines equidistributed between the minimum and maximum values of the x -wise velocity component u on the planes $x = 0.7$ and $y = 0$.

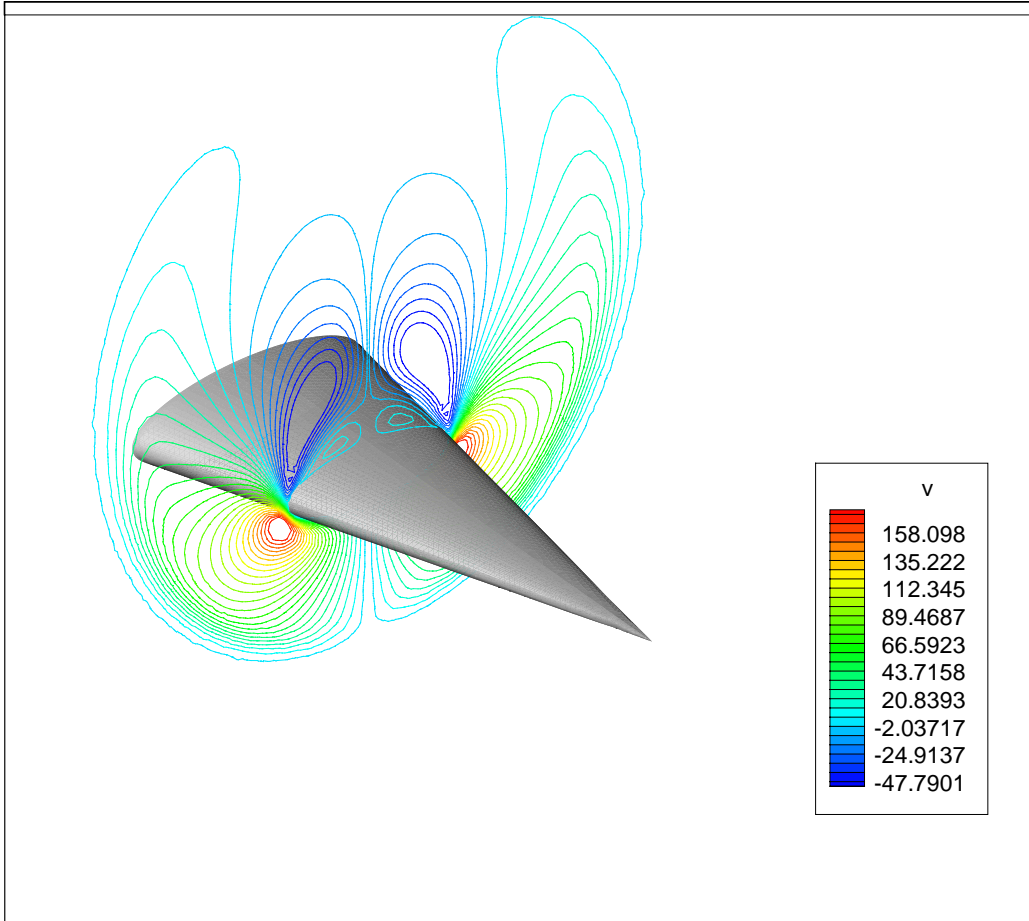


Figure 17. An aspect-ratio $A = 3$ elliptic cone model at $Re = 10^3$, $M = 2$, $\alpha = 20^\circ$; shown are contour lines equidistributed between the minimum and maximum values of the y -wise velocity component v on the plane $x = 0.7$. The condition $v \equiv 0$ is satisfied on the symmetry plane on account of the symmetry imposed.

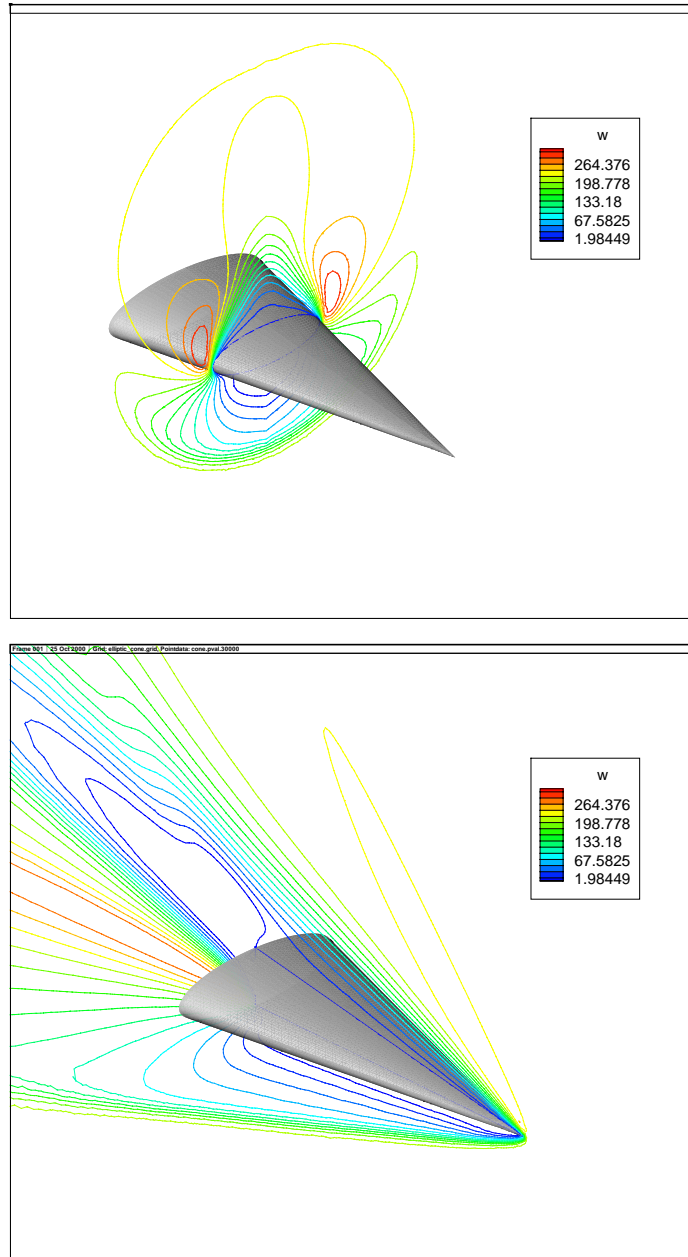


Figure 18. An aspect-ratio $A = 3$ elliptic cone model at $Re = 10^3$, $M = 2$, $\alpha = 20^\circ$; shown are contour lines equidistributed between the minimum and maximum values of the z -wise velocity component w on the planes $x = 0.7$ and $y = 0$.

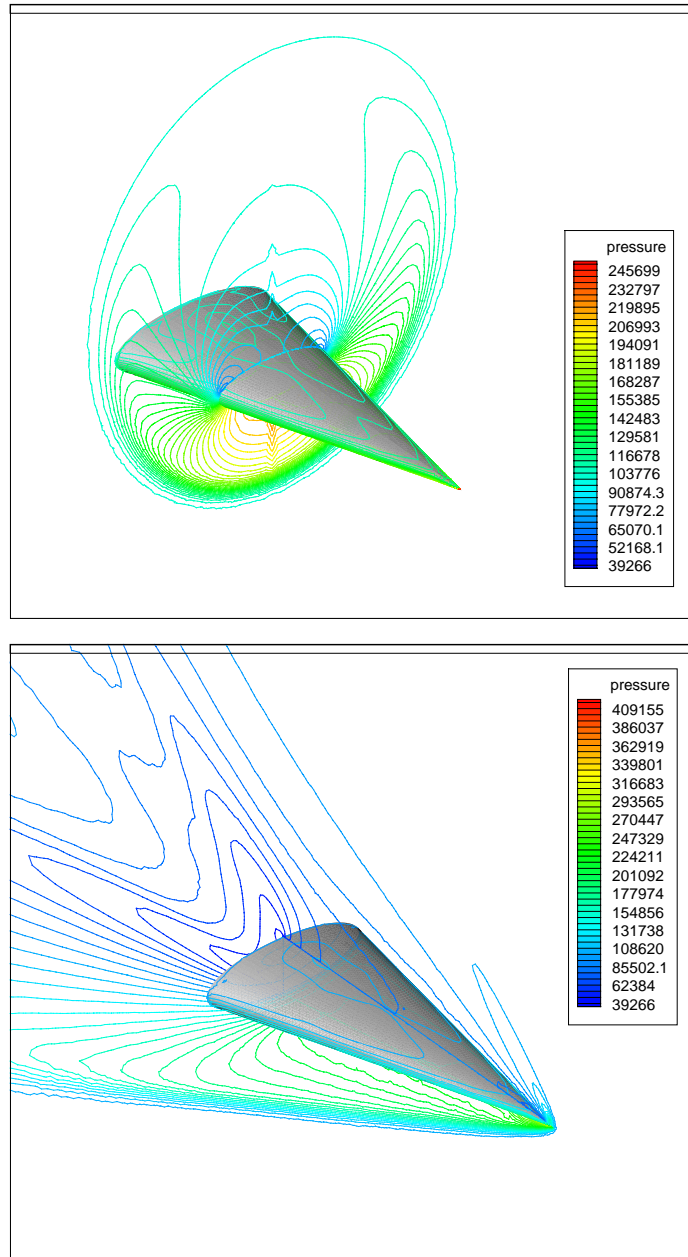


Figure 19. An aspect-ratio $A = 3$ elliptic cone model at $Re = 10^3$, $M = 2$, $\alpha = 20^\circ$; shown are contour lines equidistributed between the minimum and maximum values of p on the planes $x = 0.7$ and $y = 0$.

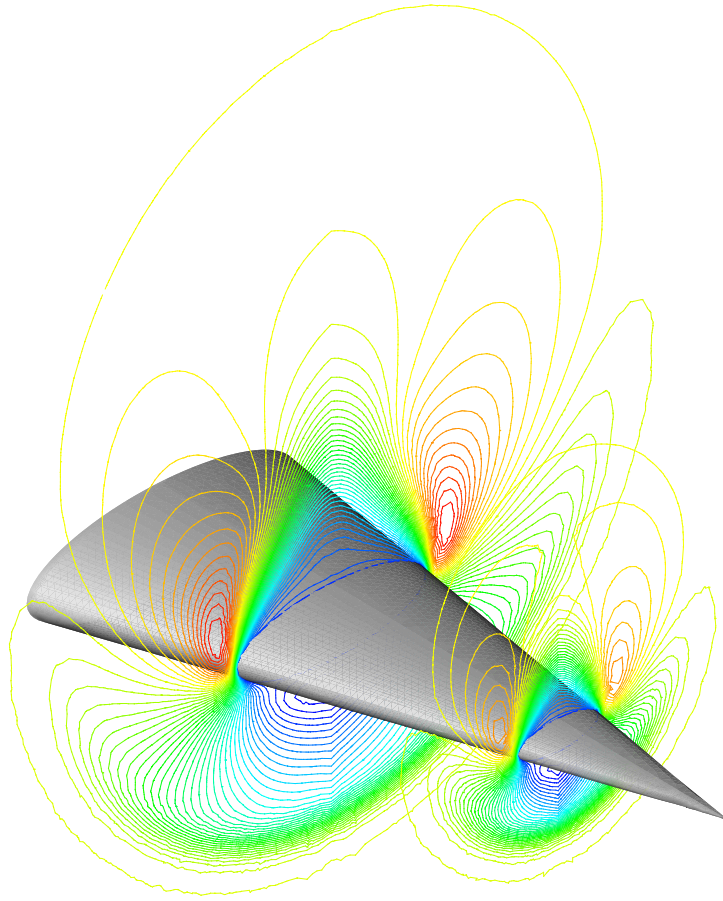


Figure 20. A qualitatively self-similar flowfield pattern of the z -wise velocity component w obtained on the elliptic cone at $M = 2, \alpha = 20^\circ$.

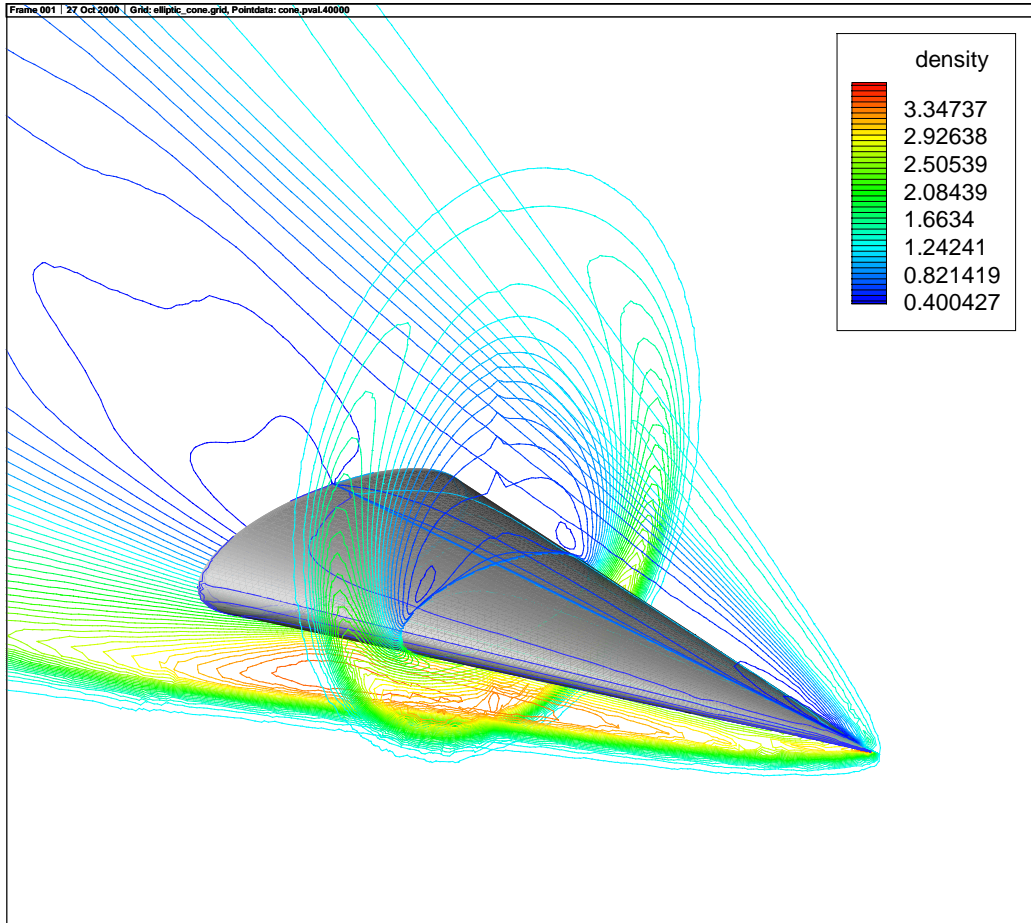


Figure 21. An aspect-ratio $A = 3$ elliptic cone model at $Re = 10^3$, $M = 4$, $\alpha = 20^\circ$; shown are contour lines equidistributed between the minimum and maximum values of ρ on the planes $x = 0.7$ and $y = 0$.

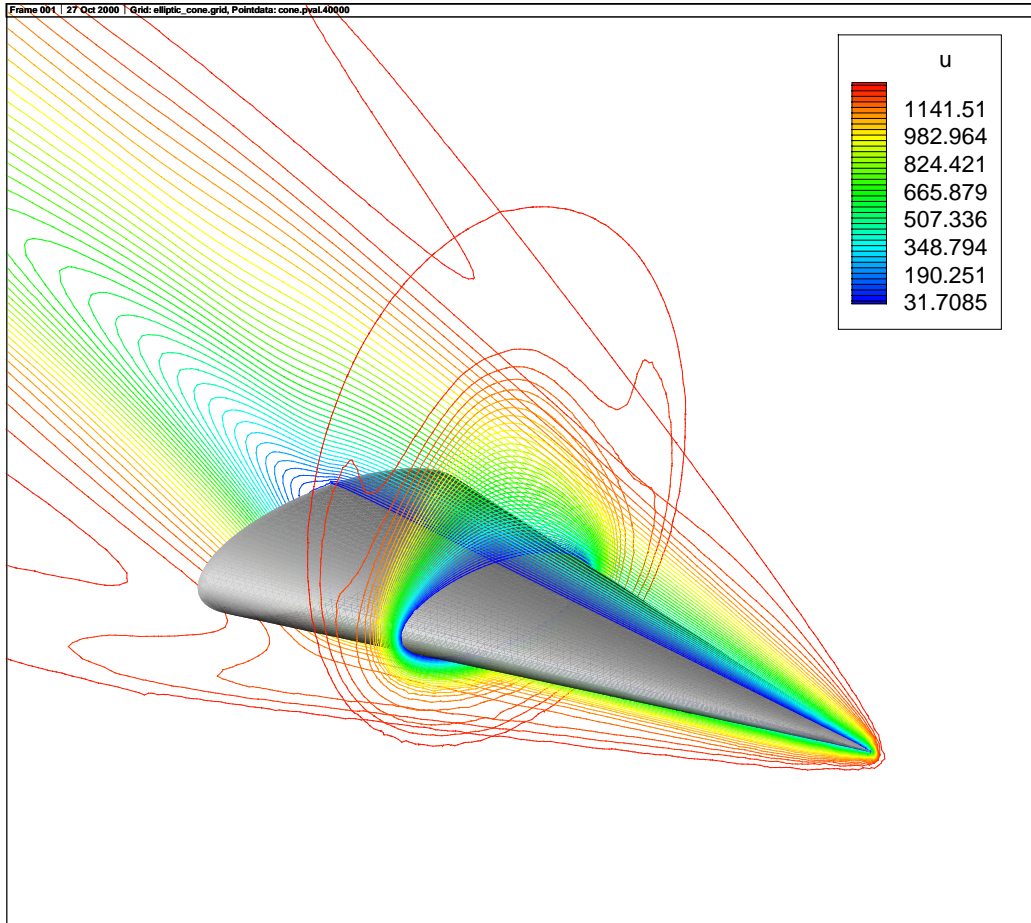


Figure 22. An aspect-ratio $A = 3$ elliptic cone model at $Re = 10^3$, $M = 4$, $\alpha = 20^\circ$; shown are contour lines equidistributed between the minimum and maximum values of the x -wise velocity component u on the planes $x = 0.7$ and $y = 0$.

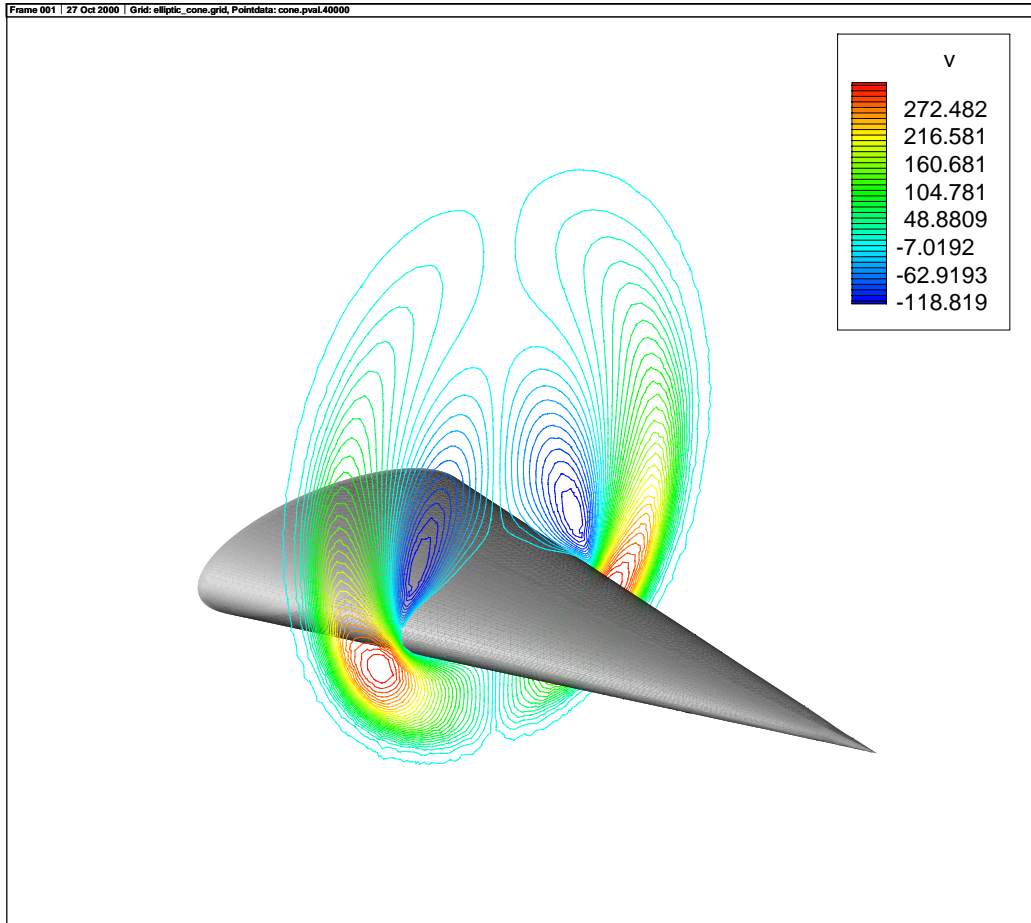


Figure 23. An aspect-ratio $A = 3$ elliptic cone model at $Re = 10^3$, $M = 4$, $\alpha = 20^\circ$; shown are contour lines equidistributed between the minimum and maximum values of the y -wise velocity component v on the plane $x = 0.7$. The condition $v \equiv 0$ is satisfied on the symmetry plane on account of the symmetry imposed.

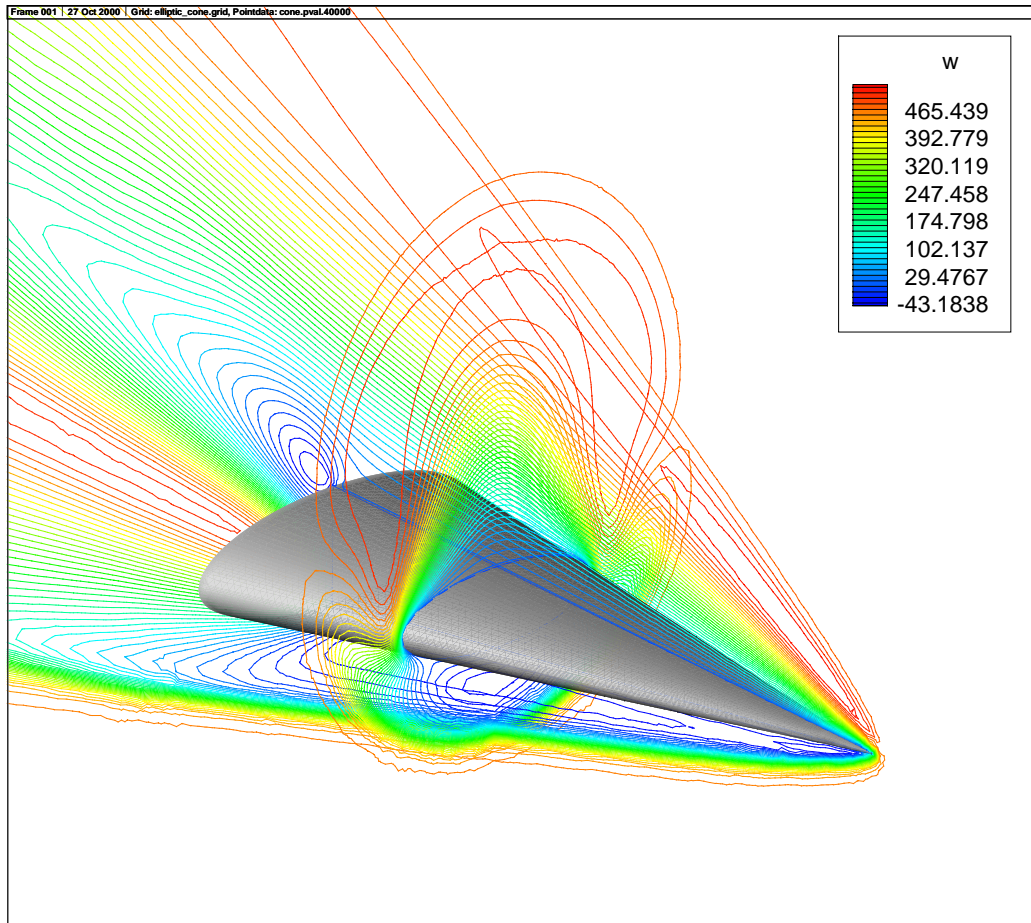


Figure 24. An aspect-ratio $A = 3$ elliptic cone model at $Re = 10^3$, $M = 4$, $\alpha = 20^\circ$; shown are contour lines equidistributed between the minimum and maximum values of the z -wise velocity component w on the planes $x = 0.7$ and $y = 0$.

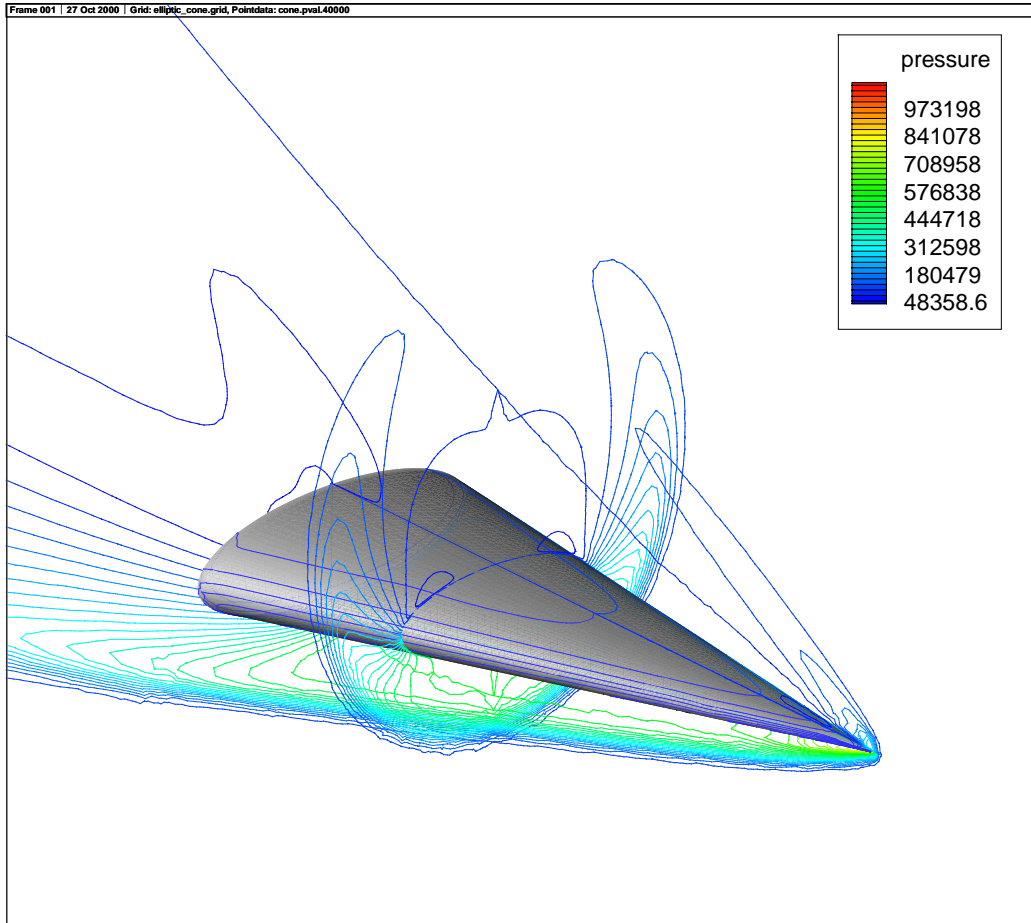


Figure 25. An aspect-ratio $A = 3$ elliptic cone model at $Re = 10^3$, $M = 4$, $\alpha = 20^\circ$; shown are contour lines equidistributed between the minimum and maximum values of p on the planes $x = 0.7$ and $y = 0$.

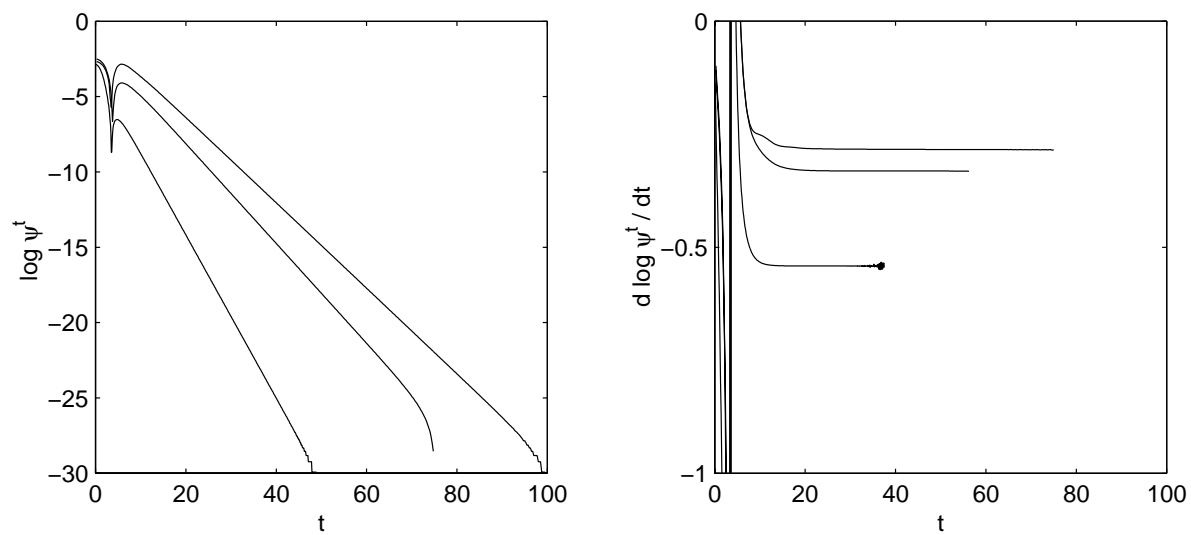


Figure 26. Convergence history of stream function $\psi(0.5, 0.5)$ against time (left) and slope of this curve (right).
Lower to upper curves, $Re = 100, 200$ and 300 , respectively.

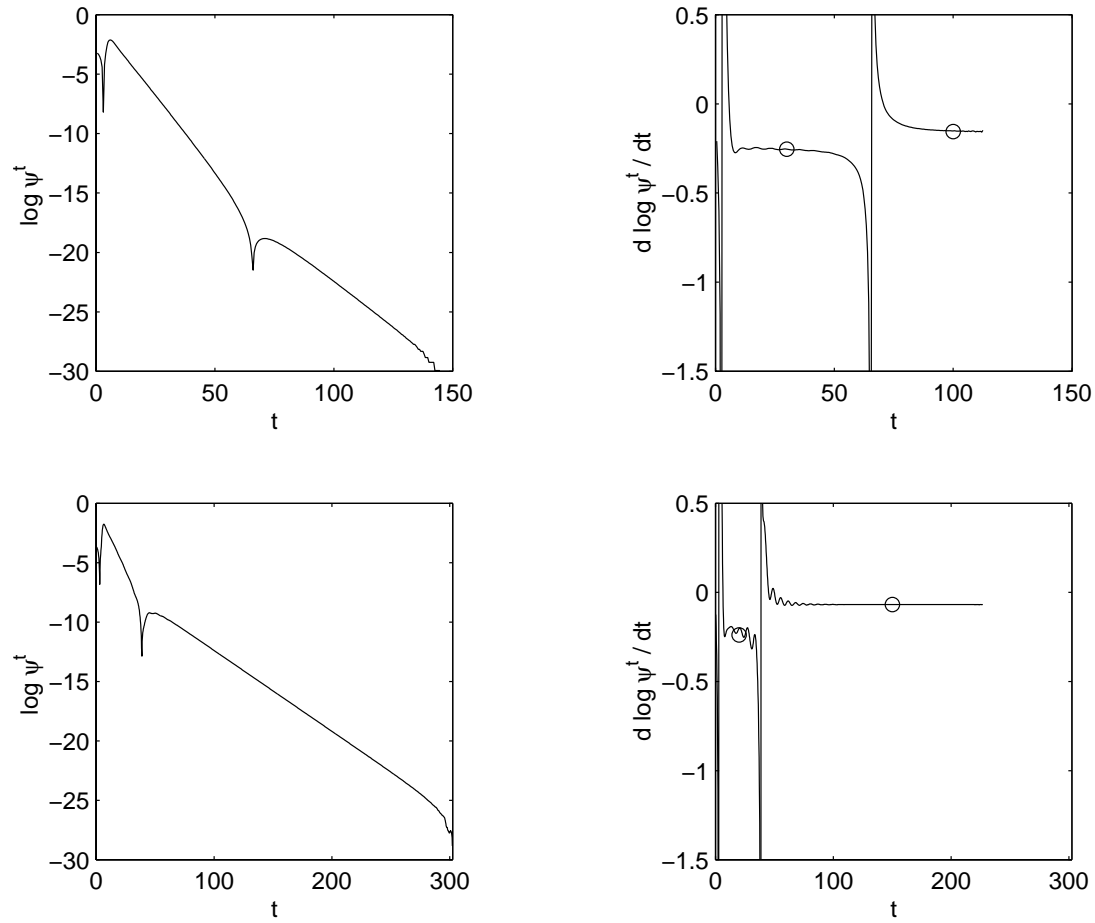


Figure 27. Convergence history of $\psi(0.5, 0.5)$ against time at $Re = 500$ (upper left) and its slope (upper right); lower left and right, respectively, the corresponding results at $Re = 1000$. In both cases superimposed and denoted by symbols are the eigenvalues of the two least stable stationary modes.

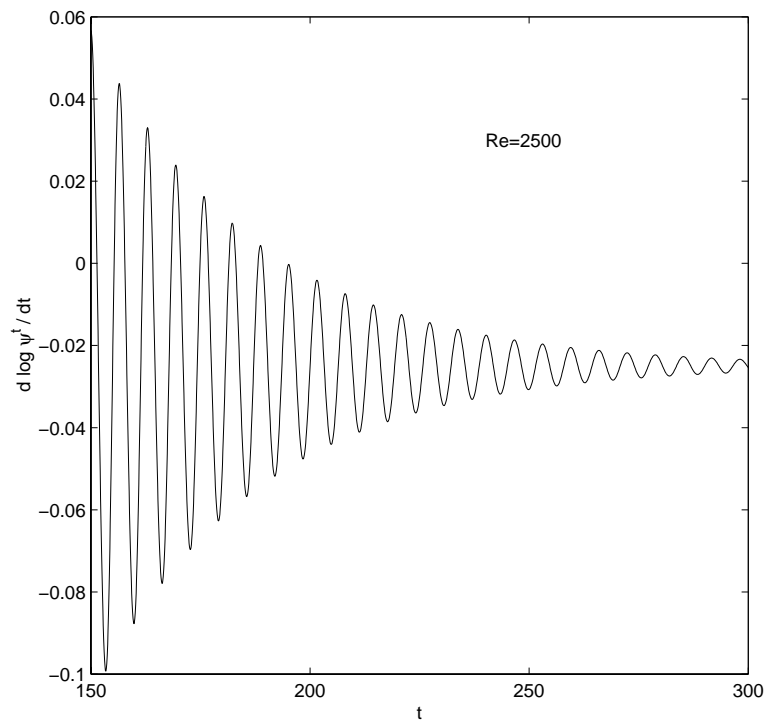
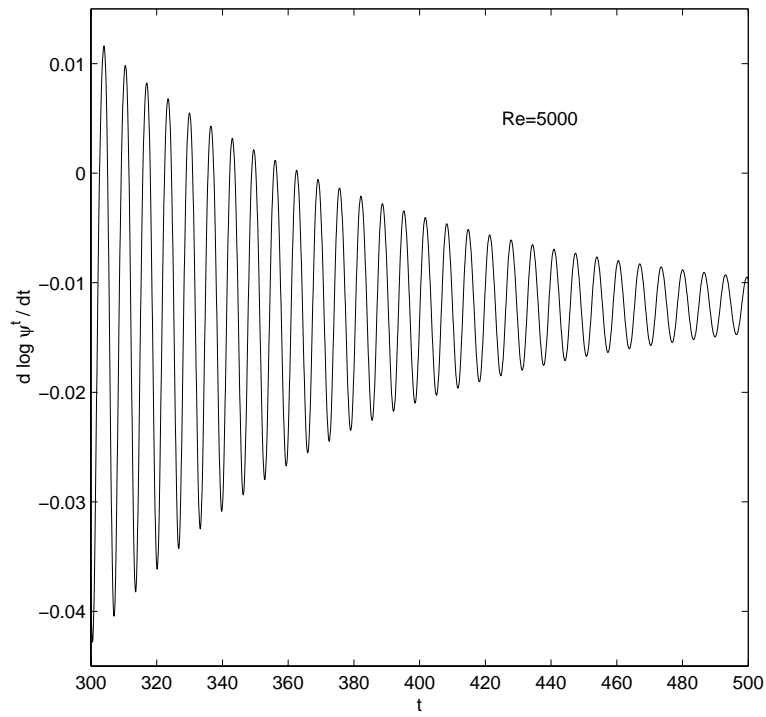
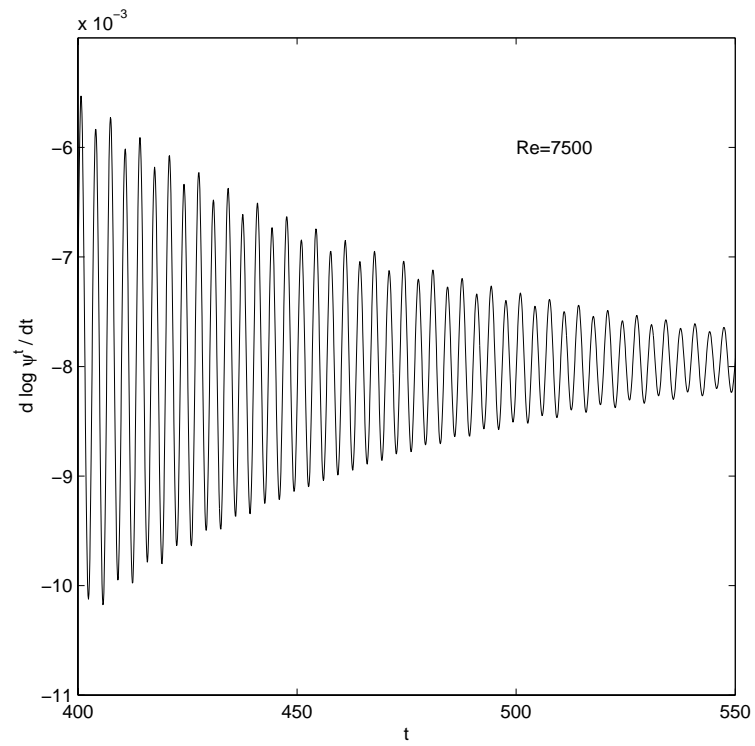


Figure 28. The dependence of the function $d(\ln \psi^t)/dt$ on time t , showing the exponential decay of a single travelling mode ($\Omega_r \approx 0.97 \pm 0.01$) superimposed upon the least damped exponentially decaying stationary disturbance at $Re = 2500$.

Figure 29. $Re = 5000$

Figure 30. $Re = 7500$

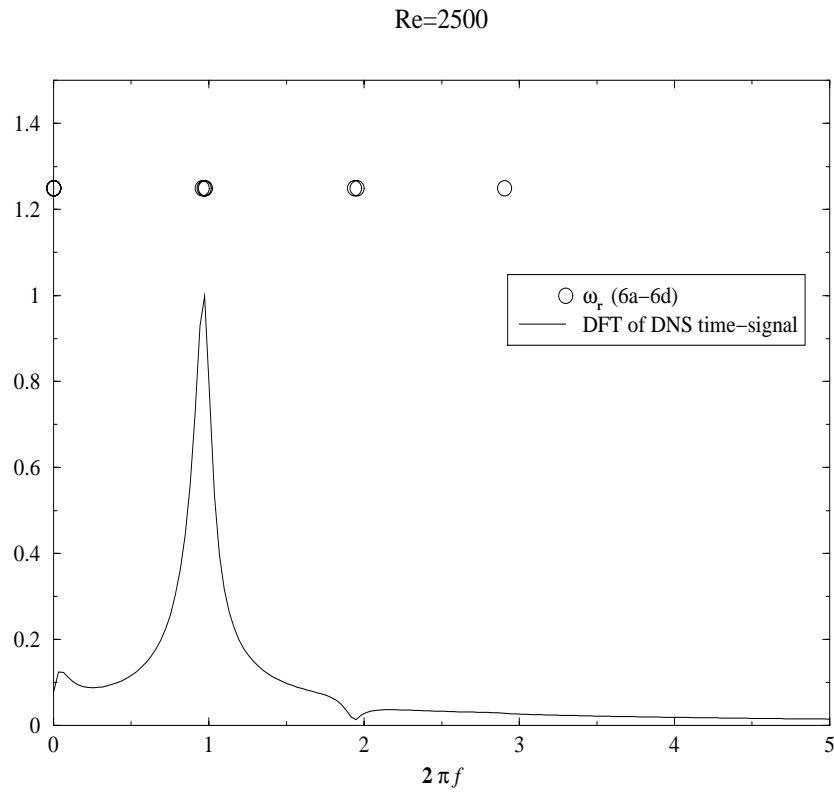


Figure 31. The correspondence of the frequencies of the damped linear ($\lambda = 0$) two-dimensional eigenmodes of the converged steady-states at different Reynolds numbers and those obtained from discrete Fourier transforms of the DNS signals. $Re = 2500$.

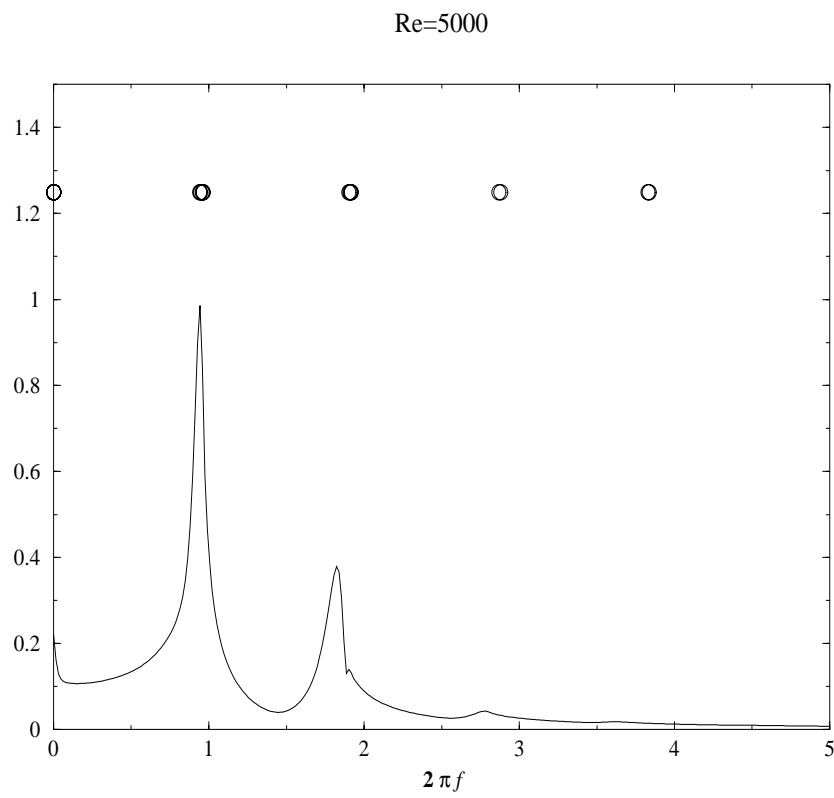
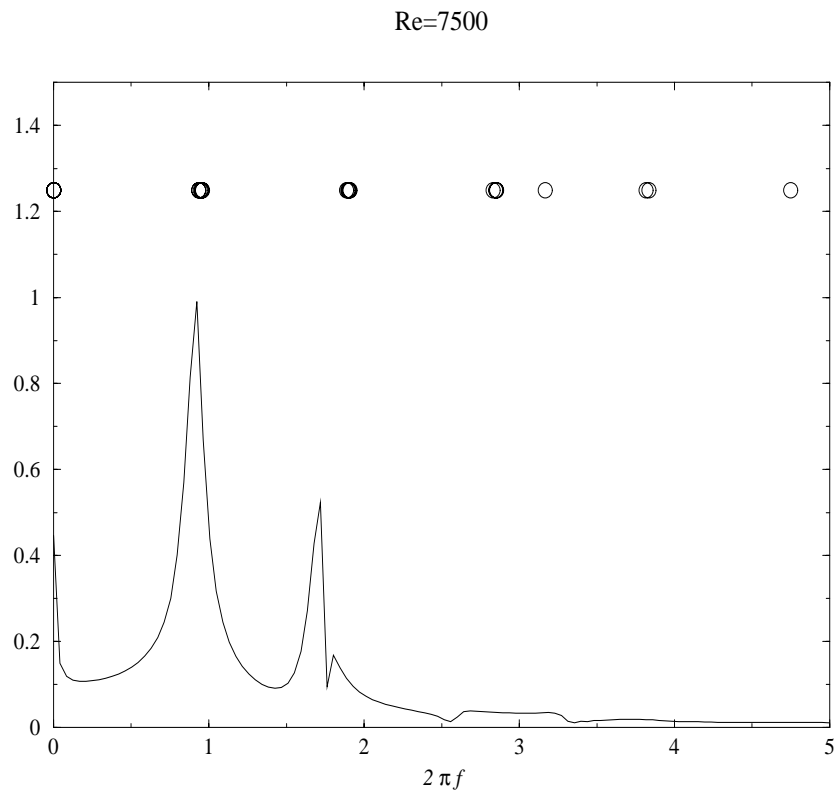


Figure 32. $Re = 5000$

Figure 33. $Re = 7500$

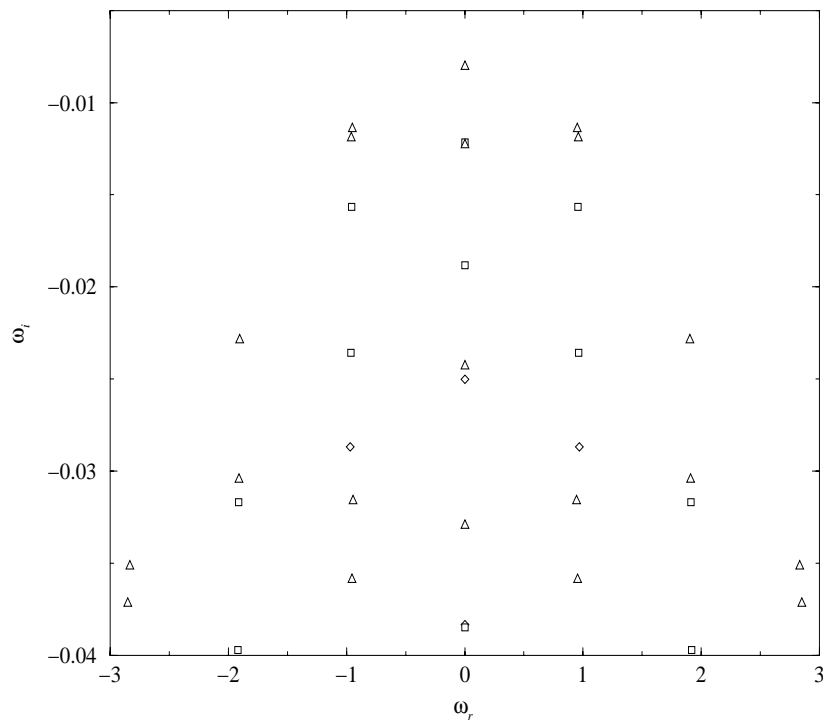


Figure 34. The filling up of the eigenvalue spectrum as Reynolds number increases; $Re = 2500$ (diamond), 5000 (square), and 7500 (triangle).

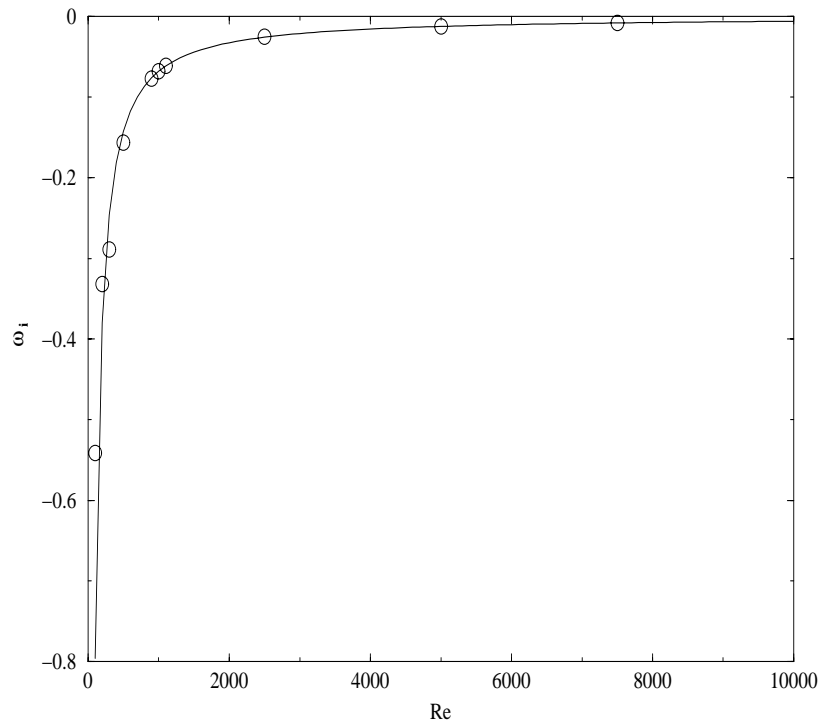


Figure 35. The dependence of the damping rate Ω_i of the least damped two-dimensional eigenmode of the converged steady-state at a Reynolds number on Re as predicted by the model (6.21) denoted by the solid line, and as calculated by numerical solution of the eigenvalue problem (6.6-6.9) denoted by the symbols.

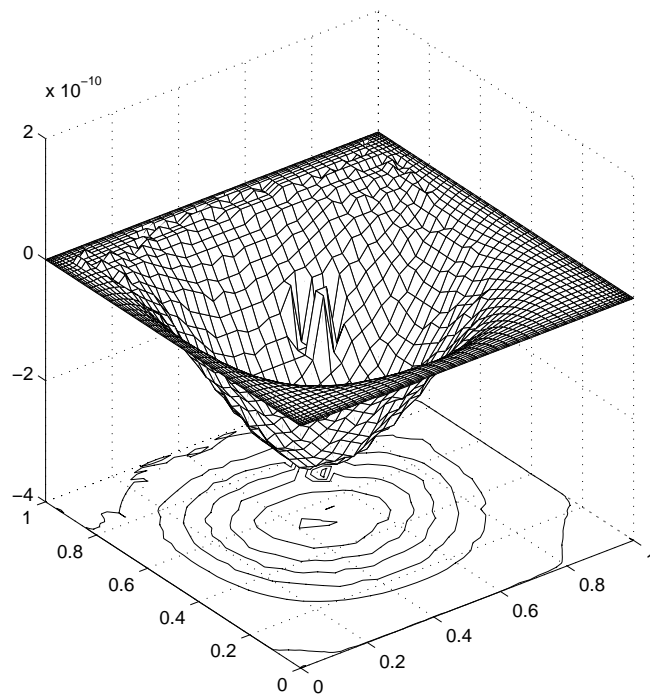


Figure 36. The spatial distribution of the difference $\Delta\tilde{\psi}(x, y) \equiv \tilde{\psi} - \bar{\psi}$ at $Re = 100$ using $Nx = Ny = 48$ Jacobi collocation points.

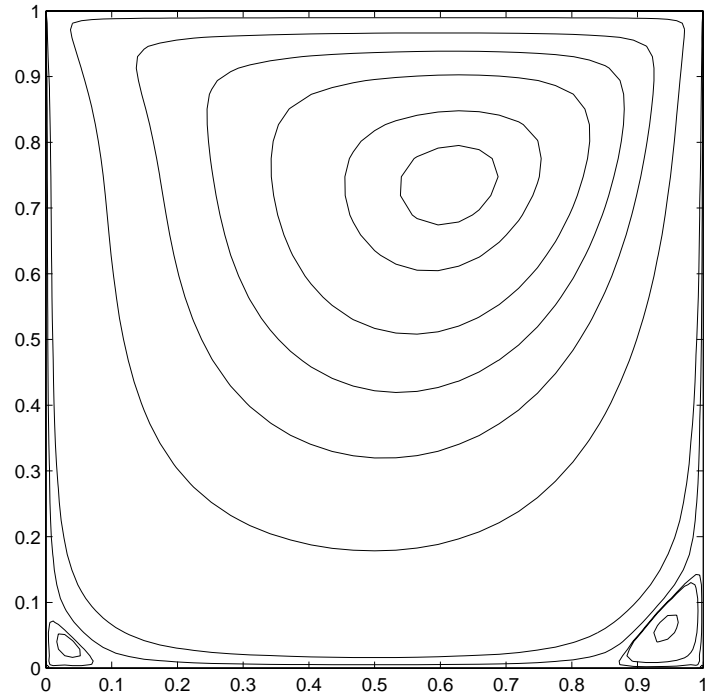


Figure 37. An estimate of the converged solution $\tilde{\psi}$ at $Re = 100$ obtained by evaluating (6.15) at $t = 15$ and using $Nx = Ny = 48$ Jacobi collocation points. Iso-contours are drawn at the levels shown by Ghia *et al.* (1982)